UNIVERSITY OF OKLAHOMA

GRADUATE COLLEGE

PORE CONNECTIVITY AND HYDROCARBON STORAGE IN SHALE RESERVOIRS

A DISSERTATION

SUBMITTED TO THE GRADUATE FACULTY

in partial fulfillment of the requirements for the

Degree of

DOCTOR OF PHILOSOPHY

By

ALI OUSSEINI TINNI
Norman, Oklahoma
2015

PORE CONNECTIVITY AND HYDROCARBON STORAGE IN SHALE RESERVOIRS

A DISSERTATION APPROVED FOR THE
MEWBOURNE SCHOOL OF PETROLEUM AND GEOLOGICAL ENGINEERING

BY

Dr. Carl Sondergeld, Chair

Dr. Chandra Rai

Dr. Deepak Devegowda

Dr. Jeffrey Callard

Dr. Daniel Resasco

© Copyright by ALI OUSSEINI TINNI 2015
All Rights Reserved.

Acknowledgements

I would like to thank my family for supporting me during the pursuit of this Ph.D degree. Thanks to Dr Lele and Rahama Beida.

I would like to express my gratitude to Dr Sondergeld, and Dr Rai. Thank you for teaching the art of scientific research.

I would also like to thank the entire IC^3 family for making the lab an enjoyable workplace.

Thanks to the members of the Unconventional Shale Gas Consortium for the financial support as well as the guidance.

Table of Contents

1 Introduction 1

- 1.1. Advances in shale characterization 1
  - 1.1.1. Definition of shale and shale reservoirs 1
  - 1.1.2. Constituents of shale reservoirs 2
  - 1.1.2.1. Inorganic minerals 2
  - 1.1.2.2. Organic matter 3
  - 1.1.3. Microstructure of shales 7
  - 1.1.4. Hydrocarbon storage mechanism 12
  - 1.1.5. Flow properties in shales 15
  - 1.1.6. Mechanical properties 20
- 1.2. Objectives 22

2 Experimental methods 24

- 2.1 Fourier transform infrared method for quantification of mineralogy 24
- 2.2 Determination of TOC 26
- 2.3 Crushed helium porosity measurement 26
- 2.4 Mercury intrusion capillary pressure measurements 29
- 2.5 Nuclear Magnetic Resonance 31
- 2.6 Subcritical nitrogen adsorption experiments 35
  - 2.6.1 BET theory for surface area calculation 36
  - 2.6.2 Pore size distribution from nitrogen gas adsorption data 38

3 Pore connectivity in shales 40

- 3.1 Concept of pore connectivity 40

3.2 Pore connectivity at atmospheric pressure 43
3.2.1 Experimental procedure and samples description 43
3.2.2 Results 45
3.3 Pore connectivity as a function of pressure 51
4 Hydrocarbon storage in Shale 62
4.1 Special considerations in shales 62
4.2 Contribution of the pores with diameters less than or equal to 15 nm to the total porosity 65
4.3 Hydrocarbon storage measurements 70
4.3.1 Experimental procedure and samples description 70
4.3.2 Methane and ethane storage measurements 73
4.4 Multicomponent desorption experiments 80
4.4.1 Experimental procedure and samples description 80
4.4.2 Results 82
5 Conclusions 89

List of Tables

Table 1.1.1: Grain density of illite and kaolinite as function of the moisture content (adapted from DeWit and Arens 1950). 3

Table 1.1.2: Properties of the different types of kerogen (after Peters and Cassa 1994). 4

Table 1.1.3: Hydrocarbon generated as a function of vitrinite reflectance (Ro (%)) (Harry 2009). 5

Table 4.3.1: Petrophysical properties of the samples used for hydrocarbon storage measurements. The letters in the sample ID refers to the shale formation. B is used for Barnett and EF is used for Eagle Ford. 71

List of Figures

Figure 1.1.1: Average clays, carbonates, quartz and feldspars content in several shale reservoirs (Sondergeld 2011). Not all shale reservoirs are shales. 2

Figure 1.1.2: Evolution of H/C and O/C as a function of maturity. We observe that H/C and O/C decrease as maturity increases (Peters and Cassa 1994). 5

Figure 1.1.3: Tmax as a function of transformation ratio (T_R=S1/(S1+S2)) for the first three types of kerogen (Tissot et al., 1987). It appears that Tmax has the best resolution of transformation ratio for type III kerogen. 7

Figure 1.1.4: Methods used to study the pore structure of shales (Bustin et al., 2008). The classification of microporosity to macroporosity follows the IUPC recommendations. 8

Figure 1.1.5: Thin section images showing the presence of porous fossils which can host pores (Gupta 2012). 9

Figure 1.1.6: Micro-CT images showing the presence of microcracks in a Banett shale sample (Odusina 2011). The observed microcracks are generally 5 to 20 µm wide. 9

Figure 1.1.7: : Different types of pores present in shale reservoirs (Loucks et al., 2011).). Intra P pores, InterP pores and OM pores are respectively the intragranular, intergranular and the pores in the organic matter. 10

Figure 1.1.8: Intrinsic organic porosity as a function of thermal maturity (Curtis et al., 2012a). A weak positive correlation can be observed. This implies that maturity is not the only controlling factor on the generation of organic pores. 11

Figure 1.1.9: Types of organic pores in oil window. (a) shows crack like pores in the organic matter (Curtis et al., 2012) while (b) shows more spherical pores in the organic matter (Laughrey et al., 2013). 12

Figure 1.1.10: Methane solubility in brine increases as the pore size decreases (Campos et al., 2009) modified by Honarpour et al., (2012). 14

Figure 1.1.11: Change in phase behavior as a function of pore size (Ma et al., 2013). It appears that the change in phase behavior becomes non negligible in pores with radii less or equal to 10nm. 14

Figure 1.1.12: Flow regimes as a function of pore size and pore pressure for methane (Sinha et al., 2013). The presence of pores from nanometers to microns has made possible the presence of multiple flow regimes in shales... 16

Figure 1.1.13:Permeability measurements as function of effective stress with different gases for a Haddssen shale sample (Ghanizadeh et al., 2013). The effective stress is considered to be equal to simple difference between the confining and pore pressure. These permeability values (in the micro-Darcy range) are very large for shales (usually in the nano-Darcy range) 18

Figure 1.1.14: Steady state permeability measurements at different pore pressures with nitrogen and a super critical fluid (adapted from Bertoncello and Honarpour 2013). A remarkable agreement can be observed between the nitrogen measurements from two different laboratories and the Klinkenberg corrected permeability with the supercritical fluid permeability. 20

Figure 1.1.15: Plot of γ as a function of ε for shale formations worldwide (Sondergeld and Rai 2011). The weak anisotropy assumption is not valid for most of the shales. ... 21

Figure 2.1.1: FTIR spectrum of several common minerals in sedimentary rocks.......... 25

Figure 2.3.1: Mean particle size frequency in 41 crushed Barnett shale samples (Kale 2009). The variation in mean particle size is mainly controlled by the sample mineralogy. 27

Figure 2.3.2: Photograph of crucible and pestles used to crush the rock samples. The assembly is designed to prevent sample loss during the crushing process..................... 28

Figure 2.4.1: Cross sectional view of a penetrometer loaded with a sample and mercury (www.micrometrics.com). Mercury is injected and pressurized through the stem. 30

Figure 2.5.1: Schematic representation of an inversion recovery pulse sequence (a) and the shape of the raw data obtain after an inversion recovery sequence (b). The measured NMR signal is called echo. 31

Figure 2.5.2: Schematic of a CPMG sequence (a) and the shape of the raw data obtained after a CPMG sequence. τ is equal to TE/2. The lower the TE value, the shorter the relaxation time which can be observed. 32

Figure 2.5.3: Schematic of a T_1-T_2 sequence (a) and the shape of the raw data obtained after a T_1-T_2 sequence (b). The spikes observed are the first echoes acquired at every TI. 34

Figure 2.5.4: Theoretical estimation of the values of T_1 and T_2 based on the BPP theory (Bloembergen et al., 1948). These estimations are conducted by increasing the viscosity of water. 35

Figure 2.6.1: Typical subcritical nitrogen adsorption and desorption isotherms for a shale sample. The shape of the adsorption and desorption isotherm as well as the shape of the hysteresis loop can be used to infer pore sizes and shapes. The sudden pressure drop on the desorption curve at P/Po = 0.4-0.5 is due to a non stable meniscus in micropores (“ Tensile strength effect”) 36

Figure 2.6.2: Example of BET transform plot. The monolayer storage capacity can be calculated from the slope and intercept. 37

Figure 3.1.1: SEM image of a Marcellus shale sample (Courtesy of Curtis). The pores are associated with the organic phase, the inorganic phase and the combination of both phases. The pores formed by the combination of organic matter and inorganic minerals will have a mixed wettability. 42

Figure 3.2.1: NMR T_2 spectra acquired on Barnett shale sample Bxx03 during sequence 1 (a) and brine and dodecane intakes (b). To obtain the brine intake, the echo-train of the “As received” state was subtracted from the echo-train of the brine imbibed state. The dodecane intake was obtained by subtracting the echo-train of the brine imbibed state from the dodecane imbibed state. The echo-train generated after the subtractions is inverted to obtained NMR T_2 distribution in (b). 44

Figure 3.2.2: Comparison between the amounts of brine imbibed during sequence 1 and sequence 2. For most samples, the amount of brine imbibed during sequence 1 is larger than the amount imbibed during sequence 2 in companion samples. 45

Figure 3.2.3: Comparison between the amounts of dodecane imbibed during sequence 1 and sequence 2 in companion samples. In most samples, the amount of dodecane imbibed during sequence 2 is larger than the amount imbibed during sequence 1. 46

Figure 3.2.4: Crushed helium porosity as a function of the total carbonate content. We observe a negative correlation between porosity and carbonate content except for the Eagle Ford samples.. 47

Figure 3.2.5: Amount of brine imbibed during sequence 2 as a function of the total clay content. 20wt% of clays is necessary in order to develop a connected network of water wet pores. 49

Figure 3.2.6: Amount of dodecane imbibed during sequence 1 as a function of TOC. This plot suggests that a minimum of 3 wt% of TOC is necessary in order to develop connectivity throughout the organic pores. 50

Figure 3.3.1: Change in NMR porosity as a function of brine and dodecane saturation pressure. Most samples do not show porosity increase after 4000 psi of saturation pressure for both fluids. 52

Figure 3.3.2: Comparison between dodecane and brine saturated NMR porosity. The brine saturated porosity is generally greater than the dodecane saturated porosity. 52

Figure 3.3.3: NMR T_2 distributions of the “As received” samples and after brine saturation at 7000 psi. There is only one NMR T_2 peak in the “As received” samples, while we generally observed two NMR T_2 peaks for the brine saturated samples. 53

Figure 3.3.4: NMR T_2 distributions of the “As received” samples and after dodecane saturation. While the “As received” samples have mainly one NMR T_2 peak, the dodecane saturated samples have bimodal NMR T_2 distributions. 54

Figure 3.3.5: T1-T2 maps of one “As received” sample from the Haynesville (H-xx689), Woodford (W-xx636), Barnett (B-xx07), Utica-Collingwood (UC-xx39), and Marcellus (M-xx99) shale formation. The maps show NMR signals with T1/T2 ratio between 1 and 1.7, which represent the residual brine (Tinni et al., 2014). 54

Figure 3.3.6: Example of Gaussian fitting applied to NMR T_2 distributions. 55

Figure 3.3.7: Brine intake of peak 1 and peak 2 after saturation at 7000 psi as a function of clay content. Note that the scales on the y axes are different. We observe a positive correlation between the increase of peak 1 and the clay content, but no relationship between the increase of peak 2 and the clay content. 56

Figure 3.3.8: Dodecane intake of peak 1 and peak 2 after saturation at 7000 psi as function TOC. Note that the scales on the y axes are different. In most samples the increase of peak 1 after dodecane saturation is less or equal to 0.5 p.u, and does not exhibit a correlation with TOC. However, the increase of peak 2 after dodecane saturation shows a positive correlation with TOC. 56

Figure 3.3.9: Comparison between the dodecane intake of peak 1 and brine intake of peak 1. The brine intake is generally larger or equal to the dodecane intake. 57

Figure 3.3.10: Comparison between the dodecane intake of peak 2, and the brine intake of peak 2. The dodecane intake of peak 2 is generally less or equal to the brine intake of peak 2. 58

Figure 3.3.11: Representation of the distribution of organic matter and inorganic minerals as a function of clay content and TOC. At clay content above 20 wt%, a continuous water wet flow path is developed. At TOC above 3 wt%, most of the organic bodies are connected; however, there are some organic that are only accessible through the water wet pores. 58

Figure 3.3.12: Comparison between the porosity of a subset of samples saturated at 7000 psi with brine and dodecane (a) and at 20,000 psi with dodecane (b). The difference between the brine and dodecane porosity reduces after dodecane saturation at 20,000 psi. 59

Figure 3.3.13: Magnitude of peak 2 after dodecane saturation at 7000 psi as a function of TOC. We observe two trends (C and D). The samples in trend C have a higher proportion of water wet pores with diameters larger than 4 nm and or mixed wettability pores. 61

Figure 4.1.1: Schematic representation of a Langmuir isotherm. 64

Figure 4.1.2: Excess methane adsorption measurements on a Sleen shale sample by Gasparik et al., (2012) (a). (b) illustrates the absolute adsorption isotherms established from (a) using 0.42 g/cc, 0.33 g/cc, and 0.27 g/cc for the adsorbed phase density. 65

Figure 4.2.1: Comparison between the porosity calculated with the DFT carbon slit method and the measured crushed rock helium porosity. The crushed rock helium porosity is generally larger than the DFT porosity because the DFT method can only resolve pore with diameters less than or equal 300 nm. 66

Figure 4.2.2: Pore size distribution obtained after subcritical nitrogen gas adsorption using the DFT carbon slit model for samples from Haynesville, Barnett, Wolfcamp and Avalon shale. The pores are assumed to have a slit shape, thus the pore size reported is the width of the slit. We consider this pore width to be representative of a pore diameter. n represent the number of samples studied for each formation. 67

Figure 4.2.3: Pore size distribution in an Eagle Ford sample (Curtis et al., 2013). The pores with radii larger than 4 nm were quantified from the SEM images while the pores with radii less than 4 nm are estimated assuming a fractal pore size distribution. 68

Figure 4.2.4: Histograms of the contribution of Φ_{15} to the total pore volume. The Haynesville samples have lowest contribution of Φ_{15} with an average of 10% while the Wolfcamp samples have the largest contribution with an average 25%. 69

Figure 4.2.5: Contribution of Φ_{15} as a function of clay content and TOC. We do not observe a relationship between the contribution of Φ_{15} with either clay content or TOC. 70

Figure 4.3.1: Pore size distributions of the samples used for storage measurements..... 71

Figure 4.3.2: Schematic of the experimental setup used for hydrocarbon storage measurements. Fluorinert FC 770 was used as confining pressure fluid. 72

Figure 4.3.3: NMR T_2 distribution of the Tennessee sandstone, Barnett, and Eagle Ford samples saturated with methane and ethane. The T_2 data was normalized to the maximum amplitude observed in each sample. The NMR signal at T_2 times larger than 200 ms represents methane or ethane in the tubings above and below the sample........ 74

Figure 4.3.4: Ethane and methane porosity as a function of pressure (a) and ψ as a function of pressure (b) for Tennessee sandstone. At high pressures, ethane, methane and crushed helium porosity have similar values, but at low pressures we observe a porosity increase. ψ is always lower than 1 for methane, but for ethane it takes on values larger than 1 at pressures below the vapor pressure.. 76

Figure 4.3.5: Ethane and methane porosity as a function of pressure (a) and ψ as a function of pressure (b) for Barnett sample B-xx97. Methane storage capacity increases as the pressure decreases because of the presence of the adsorbed phase which has a larger contrast with the bulk phase density at low pressures. No hysteresis is observed in the methane data. The ethane measurements show hysteresis below the vapor pressure because of capillary condensation. Capillary condensation also induces an increase in the storage capacity of ethane at pressures below the vapor pressure........................... 78

Figure 4.3.6: Ethane and methane porosity as a function of pressure (a) and ψ as a function of pressure (b) for Eagle Ford sample EF-xx72. At 4000 psi, the porosity measured with ethane, methane and the crushed helium porosity have similar values. Methane storage capacity increases at lower pressure because of adsorption, and ethane storage capacity increases below the vapor pressure because of capillary condensation which also induces hysteresis in the ethane measurements. 79

Figure 4.3.7: Ethane and methane porosity as a function of pressure (a) and ψ as a function of pressure (b) for Eagle Ford sample EF-xx18. This sample shows a reduction in ethane porosity due to pore compressibility at pressures between 2000 psi and 750 psi. This reduction in porosity balances the increase in ethane and methane storage capacity at low pressures. 80

Figure 4.4.1: Phase diagram of 85% CH_4 and 15% C_4H_{10}. At 30 ^oC, the mixture is in gaseous phase above 1850 psi, two phases (gas-liquid) between 1850 psi and 375 psi, and single phase gas below 375 psi. 81

Figure 4.4.2: Experimental setup used for multicomponent desorption experiments. GC/MS is the abbreviation of gas chromatograph/mass spectrometer (Agilent 7890B). 81

Figure 4.4.3: FID signal recorded during the analysis of the mixture collected at 3400 psi from an empty pressure vessel. The FID signal is proportional to the mass of hydrocarbon. 83

Figure 4.4.4: $R_{CH4/C4H10}$ as a function of pressure for the empty pressure vessel. The horizontal dashed line indicates the theoretical value of $R_{CH4/C4H10}$ (1.56) for a mixture of 85% CH_4 - 15% C_4H_{10}. The increase of $R_{CH4/C4H10}$ below the dew point is due to the settling of butane enriched liquid at the bottom of the pressure vessel. 84

Figure 4.4.5: $R_{CH4/C4H10}$ as a function of pressure for Berea sandstone. The mixture composition is constant during the production from 3300 psi to 1900 psi. 85

Figure 4.4.6: $R_{CH4/C4H10}$ as a function of pressure for Eagle Ford sample EF-xx72. The mixture composition is constant during the production from 3200 psi to 1900 psi. 85

Figure 4.4.7: $R_{CH4/C4H10}$ as a function of pressure for B-xx97. We observe an increase of $R_{CH4/C4H10}$ at pressures greater than the dew point of the original mixture, because of the preferential adsorption of butane by the sample. 86

Figure 4.4.8: $R_{CH4/C4H10}$ as a function of pressure for Eagle Ford sample EF-xxx82. $R_{CH4/C4H10}$ starts at a value greater than the normal value for the original mixture, implying a preferential adsorption of butane at pressures greater than 3000 psi. This preferential adsorption induces liquid dropout at pressures greater than the dew point of the original mixture. 87

Figure 4.4.9: Sample EF-xxx82 after the injection of 85% CH_4 -15%C_4H_{10}. We observe that the sample was fractured during the experiments, and the presence of oil bubbles on the surface of the sample. 88

Abstract

Considerable advances have been made in the science of shale characterization during the past two decades. However, the evaluation of the production potential of shale reservoirs is still hindered by the lack of understanding of fluid flow and storage. The present dissertation summarized several laboratory experiments designed to evaluate pore connectivity as well as storage and production mechanisms in shale reservoirs.

SEM studies on ion milled surfaces of shales revealed that the pores in shales have sub micrometer diameters and are associated with the organic matter, the inorganic minerals and the interfaces between organic matter and inorganic minerals. The organic pores are hydrocarbon wet, while the inorganic pores are generally water wet and the pores at the interfaces between organic matter and inorganic minerals are considered mix wet. The Current methods used to study pore connectivity fail to acknowledge the presence of pores with different wettability. The storage and flow of fluids as a function of pore wettability invalidates the concept of oil-water relative permeability in shales.

The combination of spontaneous imbibition and pressure saturation of shale samples with brine and dodecane was used to study the connectivity of the water wet and hydrocarbon wet pore network. 20 wt% of clay and 3-4 wt% of TOC are required to develop a connected water wet and hydrocarbon wet pore network respectively. The connectivity of the water wet and hydrocarbon wet pore networks are enhanced by the presence of mix wettability pores. These mixed wettability pores provide the best flow path for hydrocarbon delivery.

The study of the hydrocarbon storage mechanisms in shales was conducted by measuring the NMR T_2 spectra of shale samples saturated with methane and ethane at different pore pressures. Storage measurements show that the main mechanism of fluid storage at high pressures is fluid compressibility while adsorption and capillary condensation are the main storage mechanisms at low pressures. In contrast with numerous model predictions, no change in fluid critical properties was observed.

The multicomponent desorption experiments show that heavier hydrocarbons can be preferentially adsorbed during the production of hydrocarbon. This preferential adsorption will induce a dynamic change in the in-situ fluid composition during pressure depletion.

1 Introduction

1.1. Advances in shale characterization

1.1.1. Definition of shale and shale reservoirs

Shales are sedimentary rocks composed of more than 67% clay size particles (less than 4 µm). However, this general definition might lead to confusion in some instances. A literature review on the definition of shale provides various definitions.

Shale is defined by the USGS (2002) as fine grained sedimentary rock, formed by the consolidation of clay, silt or mud. For the British Geological Survey (2003), shale and mudstone are hard mudrocks with variable proportions of quartz silts with grain size less than 32 µm. The Online AGI glossary attempted to differentiate between shale and mudstone by defining shales as fissile while mudrocks do not exhibit fissility. However, as pointed out by Bohacs et al., (2013) fissility can be weathering dependent, and a rock considered mudstone can become a shale (with fissility) over time.

From every definition above, it appears that shales will include a wide variety of rocks with a predominance of clay sized particles. However, **Figure 1.1.1** shows that shale reservoirs are not necessarily dominated by clay in terms of mineralogy.

Shale reservoirs are organic rich porous fine-grained rocks which fall under the category of unconventional reservoirs. Cander (2012) defined unconventional reservoirs as hydrocarbon reservoirs where permeability or viscosity needs to be altered in order to produce the hydrocarbons at economic rates. The commonality of most shale reservoirs is that the hydrocarbons have been generated in-situ through the maturation of organic matter. However, there is evidence of migration in some shale reservoirs (Bohacs et al., 2013).

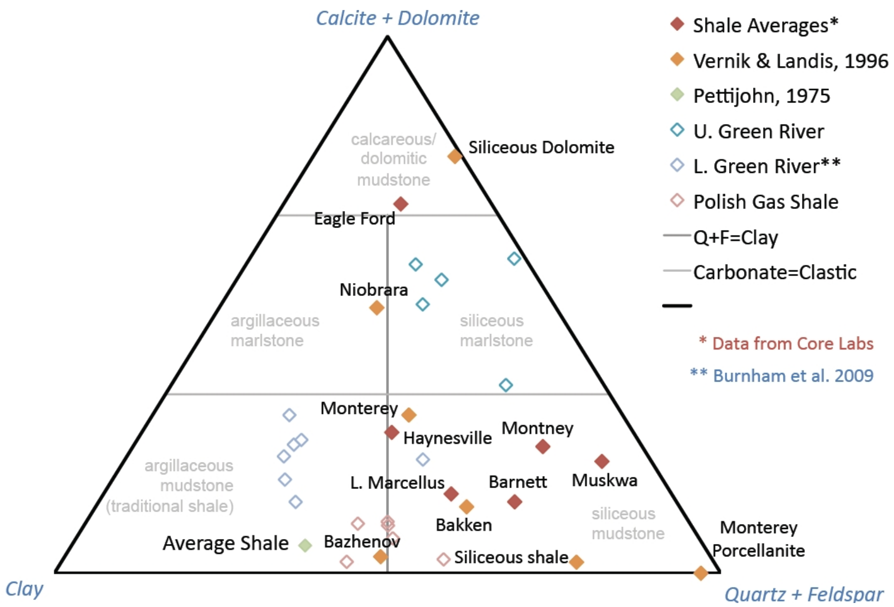

Figure 1.1.1: Average clays, carbonates, quartz and feldspars content in several shale reservoirs (Sondergeld 2011). Not all shale reservoirs are shales.

1.1.2. Constituents of shale reservoirs

By definition, shale reservoir rocks are comprised of two main components which are the inorganic minerals and the organic matter. These two components, by their nature, will have different properties which will directly affect the intrinsic quality of the reservoirs.

1.1.2.1. Inorganic minerals

The inorganic minerals are often the most abundant constituents of shale reservoirs. They generally account for 85-98% of the rock composition by weight and 70-94% by volume. The main inorganic minerals found in shales are clays minerals, carbonate minerals and quartz.

Among the minerals present in shales, clays are the least understood because of their complex structures and chemical reactivity. It is very challenging to obtain an accurate value of the density of clay minerals, due to their chemical reactivity and their tendency to adsorb water. The uncertainty in density affects the calculation of grain density based on mineralogy. Based on its crystallographic arrangement, the grain density of illite should be between 2.76 and 3 g/cc (Dana 1921). A value of 2.609 g/cc is reported by Gruner (1937) for kaolinite and 2.6-2.96 g/cc for chlorite. DeWit and Arens (1950) measured the grain density of illite and kaolinite as a function of moisture content. Their results are summarized in **Table 1.1.1**.

Table 1.1.1: Grain density of illite and kaolinite as function of the moisture content (adapted from DeWit and Arens 1950).

Clay mineral	Moisture content (wt%)	Grain density (g/cc)
Illite	0.0	2.642
	8.3	2.409
	12.0	2.310
	24.8	2.020
	76.0	1.480
Kaolinite	0.4	2.663
	0.8	2.651
	0.9	2.642
	6.5	2.427

1.1.2.2. Organic matter

Organic matter as both solid and liquid is present in shales and is quantified by TOC (total organic carbon), usually expressed in weight percentage. TOC includes kerogen, bitumen, pyrobitumen, dead carbon and liquid hydrocarbons.

Kerogen is defined as the fossilized form of phytoclasts which are organic particles of algae, bacteria, land plants and/or fungi. Their decomposition during thermal maturation yields various petroleum products. Four types of kerogen can be distinguished based on the origin of the phytoclasts, hydrogen to carbon ratio (H/C) and oxygen to carbon ratio (O/C) of the immature kerogen (**Table 1.1.2**). Bitumen represents the solid fraction of the organic matter, which is soluble in organic solvents (Bohacs et al., 2013). Pyrobitumen is the thermally altered solidified bitumen not soluble in organic solvents.

Thermal maturation is defined by the chemical reactions taking place at temperature above 60°C, leading to the decomposition of kerogen. The extent of these chemical reactions is often denoted as maturity.

Table 1.1.2: Properties of the different types of kerogen (after Peters and Cassa 1994).

Kerogen Type	Main Origin	H/C	O/C	Main petroleum product
I	Algal organic matter	≥1.5	≤0.1	Oil
II	Algal organic matter	1-1.5	≤0.1	Oil with small proportion of gas
III	Wood material	<1	≤0.3	Gas
IV	Wood material	0.5-0.6	≤0.4	NA

The most common maturity index is vitrinite reflectance (Ro (%)). Ro (%) measures the reflectance of vitrinite (particular type of organic maceral derived from land plants) immersed in oil. The reflectance of vitrinite increases with thermal maturation. **Table 1.1.3** provides a range of values of Ro (%) as a function of the petroleum products generated. Thermal maturation affects the H/C ratio and O/C ratio of the various kerogens in different ways (**Figure 1.1.2**). Thermal maturity maps have become one of the main exploration tools in shale reservoirs.

Table 1.1.3: Hydrocarbon generated as a function of vitrinite reflectance (Ro (%)) (Harry 2009).

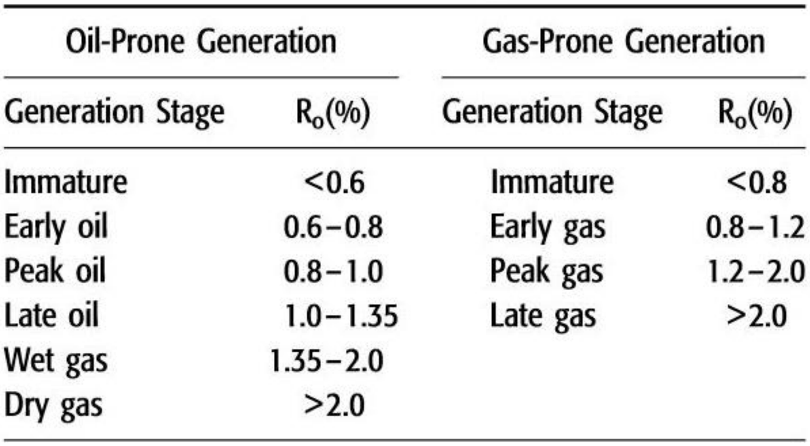

Oil-Prone Generation		Gas-Prone Generation	
Generation Stage	R_o(%)	Generation Stage	R_o(%)
Immature	<0.6	Immature	<0.8
Early oil	0.6−0.8	Early gas	0.8−1.2
Peak oil	0.8−1.0	Peak gas	1.2−2.0
Late oil	1.0−1.35	Late gas	>2.0
Wet gas	1.35−2.0		
Dry gas	>2.0		

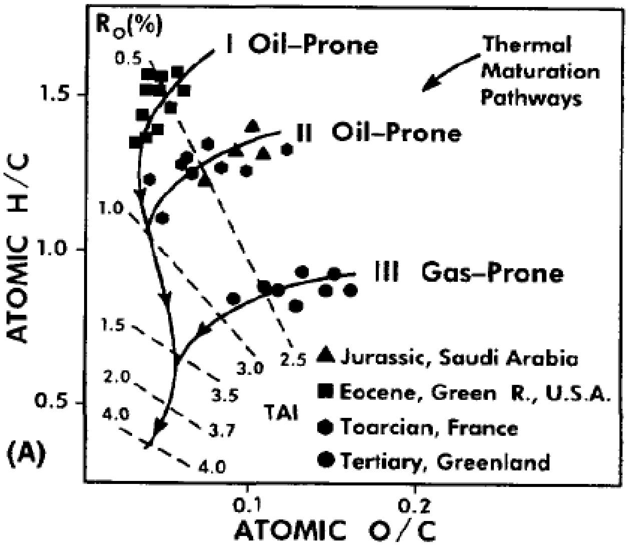

Figure 1.1.2: Evolution of H/C and O/C as a function of maturity. We observe that H/C and O/C decrease as maturity increases (Peters and Cassa 1994).

The determination of Ro (%) requires the expertise of an experienced organic petrologist for the identification of the vitrinite macerals and the estimation of the reflection index. This practice is subjective. Vitrinite is derive from land plant tissues, thus it will not be possible to measure Ro (%) on shales that do not have kerogen which originated from land plants such as pre-Silurian shales.

To overcome the shortcomings of the Ro (%) method the industry has been extensively using the source rock analysis method (SRA) (Espitalie et al., 1977). This method consists of maintaining a crushed sample at 300° C for 3 minutes before increasing the temperature up to 600° C at a rate of 25° C/minute. During the heating process the intensity of the product expelled is captured with a flame ionization detector (FID). Three quantities are of main interest in an SRA measurement: S1, which is the peak measured at 300 ^{o}C, is interpreted as the amount of converted hydrocarbon present in the rock sample; S2 measures the amount of hydrocarbon generated after thermal cracking of the kerogen. It is interpreted as the potential for hydrocarbon generation, and the temperature at which the S2 peak occurs, Tmax, is an indication of the thermal maturity. Tmax can be related to Ro (%) by **equation 1.1.1** (Jarvie et al., 2001). S3 measures the amount of CO_2 produced during the heating process.

$$R_o(\%) = 0.018 * \text{Tmax} - 7.16 \qquad 1.1.1$$

Tissot et al., (1987) have shown that Tmax might not be a good indicator of maturity because it depends on the type of kerogen (**Figure 1.1.3**). Tissot et al., (1987) also found that SRA data are sensitive to the drilling fluid used. Therefore the SRA data must be interpreted with caution.

Dang (2013) developed a method to measure the maturity of organic matter by analyzing the FTIR spectrum of the organic matter. This method named R_{CH} quantifies

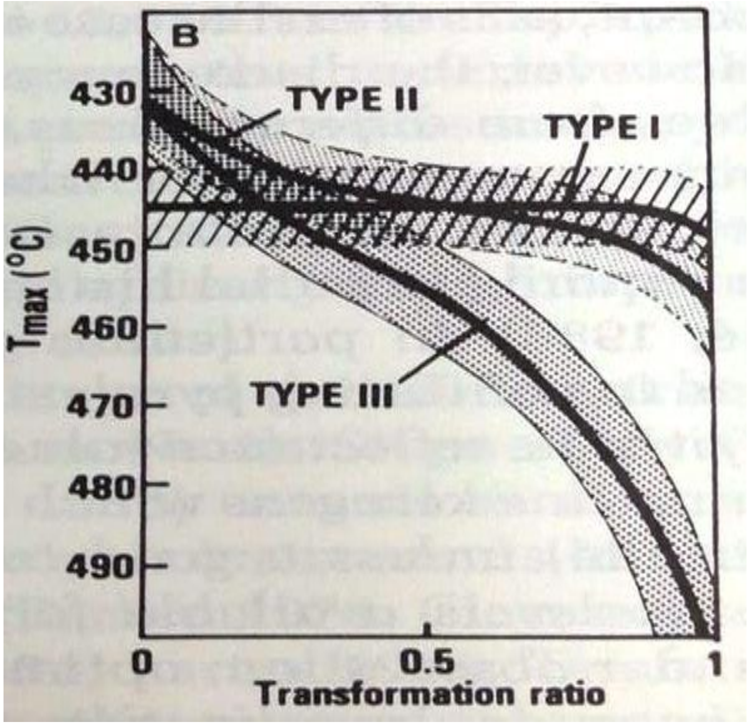

Figure 1.1.3: Tmax as a function of transformation ratio (T_R=S1/(S1+S2)) for the first three types of kerogen (Tissot et al., 1987). It appears that Tmax has the best resolution of transformation ratio for type III kerogen.

the ratio of the aromatic compounds to the aliphatic compounds remaining in the present day organic matter. As organic matter mature the amounts of aromatic compounds decrease while the amount of aliphatic compounds increases. Therefore, the R_{CH} method appears to be an objective method to determine the maturity of shales.

1.1.3. Microstructure of shales

Reservoir properties such as porosity and permeability are largely controlled by the microstructure. Several researchers (Bustin et al., 2008; Curtis et al., 2010; Handwerger et al., 2011; Suarez et al., 2012; and Chalmers et al., 2012) have studied the microstructure of shales and found microstructural features from micrometer to nanometer scales. To study shale microstructure at different scales a combination of imaging and/ or intrusion techniques have to be used (**Figure 1.1.4)**.

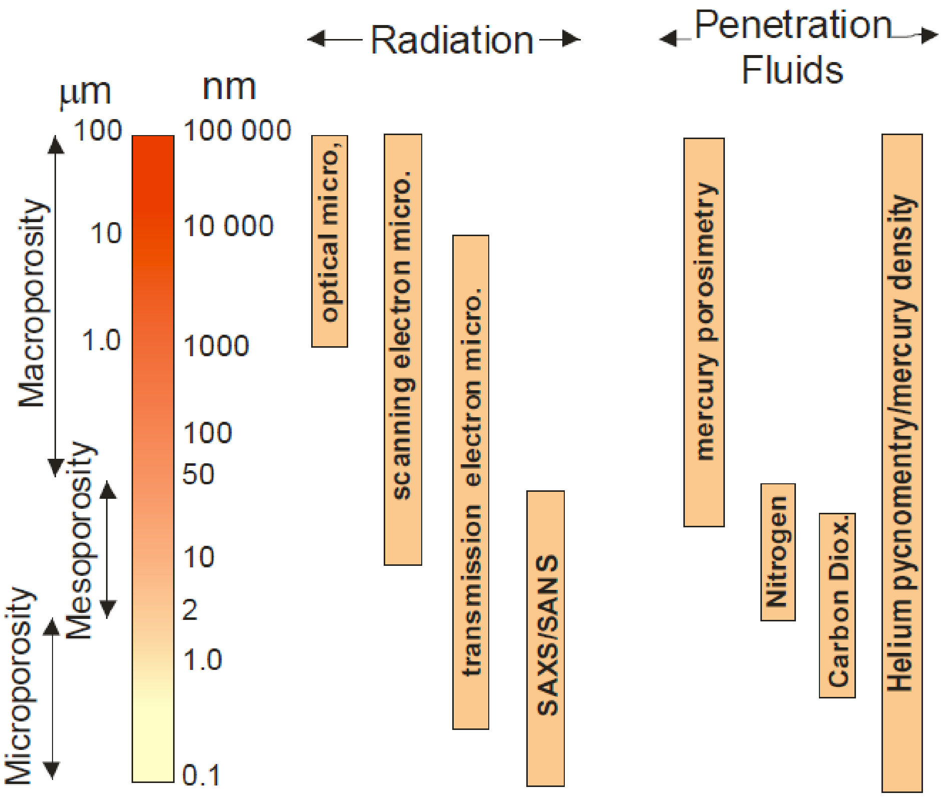
Radiation
Penetration Fluids
µm
nm
100
10
1.0
100 000
10 000
1000
100
50
10
2
1.0
0.1
Macroporosity
Mesoporosity
Microporosity
optical micro,
scanning electron micro.
transmission electron micro.
SAXS/SANS
mercury porosimetry
Nitrogen
Carbon Diox.
Helium pycnomentry/mercury density

Figure 1.1.4: Methods used to study the pore structure of shales (Bustin et al., 2008). The classification of microporosity to macroporosity follows the IUPC recommendations.

Thin section images (optical microscopy) on some shale samples have shown the presence of fossil skeletons which contain substantial porosity (**Figure 1.1.5**). Micro-CT X-ray images **(Figure 1.1.6**) show the presence of a considerable number of micrometer size cracks in shales even in fine crushed samples. However, it is not known to date if the microcracks in shales are open in subsurface conditions or if they are the result of clay desiccation or expansion of the core due to stress relief after coring.

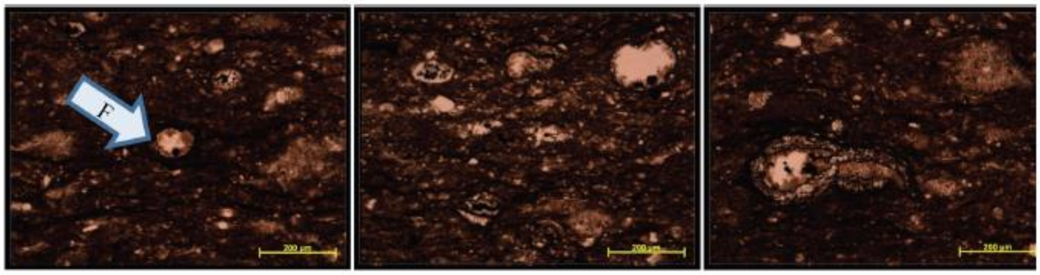

Figure 1.1.5: Thin section images showing the presence of porous fossils which can host pores (Gupta 2012).

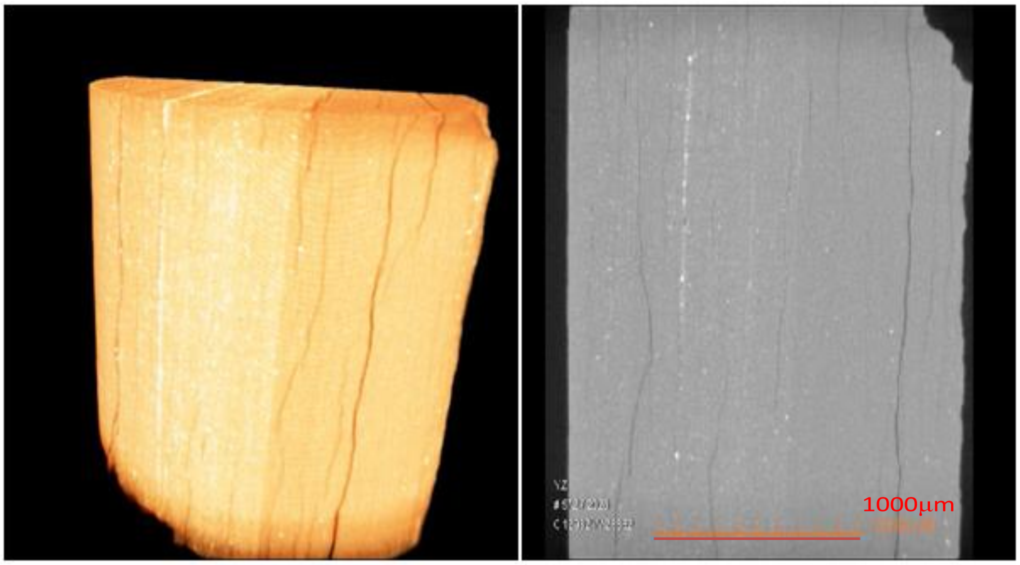

Figure 1.1.6: Micro-CT images showing the presence of microcracks in a Banett shale sample (Odusina 2011). The observed microcracks are generally 5 to 20 µm wide.

Numerous SEM studies on ion milled shale samples show a distribution of nanometer size pores (Curtis et al., 2010; Sondergeld et al., 2010; and Loucks et al., 2011) as intergranular pores, intraganular pores and pores within the organic matter. Ion milling is a technique which uses high energy ions (often gallium or argon) to sputter away materials from the sample surface (Curtis et al., 2010). This will produce a highly polished sample surface with virtually no topography.

Figure 1.1.7 shows the different types of pores generally observed in shales. The organic porosity appears to be the general type of porosity observed in shales. However the lack of positive trend between porosity and TOC in Barnett (Sondergeld et al., 2010) suggests that there is a large portion of the pore space in the inorganic fraction. The intrinsic organic porosity can reach 35% in certain cases, Curtis et al., (2012a). However, in some cases no porosity is observed within the organic matter. At this point, it is necessary to distinguish the organic matter observed in the oil window from that observed in the gas window.

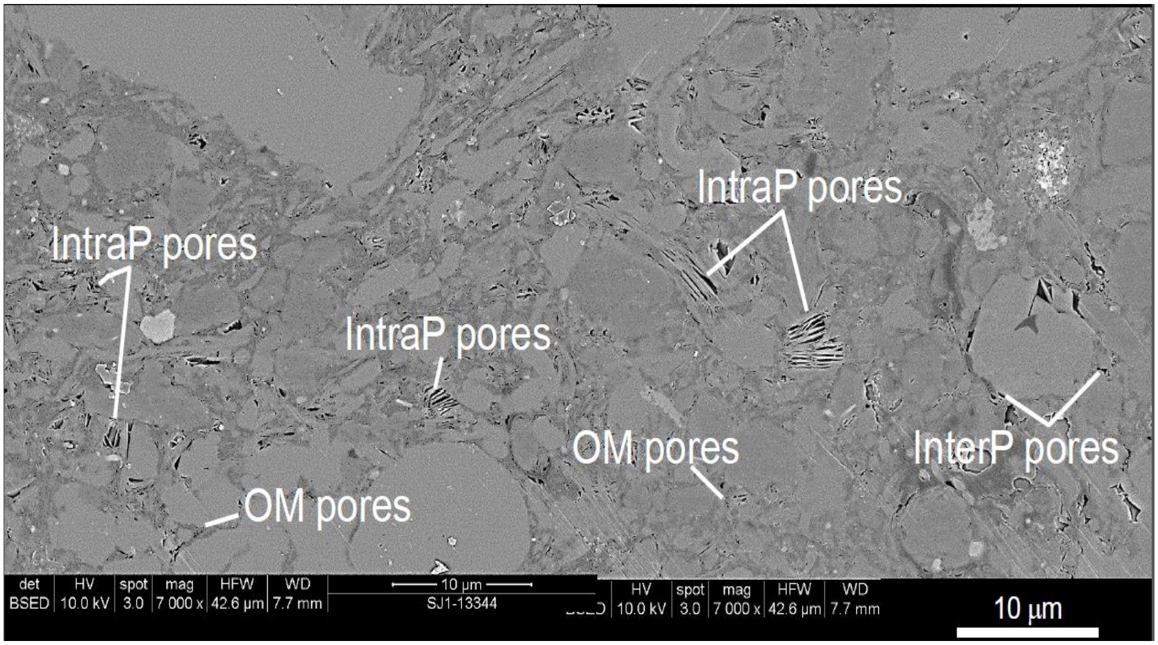
IntraP pores
IntraP pores
IntraP pores
OM pores
OM pores
InterP pores
det HV spot mag HFW WD
BSED 10.0 kV 3.0 7 000 x 42.6 µm 7.7 mm
10 µm
SJ1-13344
HV spot mag HFW WD
10.0 kV 3.0 7 000 x 42.6 µm 7.7 mm
10 µm

Figure 1.1.7: : Different types of pores present in shale reservoirs (Loucks et al., 2011).). Intra P pores, InterP pores and OM pores are respectively the intragranular, intergranular and the pores in the organic matter.

In the gas window, Curtis et al., (2012a) observed more porosity in the organic matter as the maturity increases (**Figure 1.1.8**).The general explanation given by Curtis et al, (2012a) is that the generation of hydrocarbons by cracking of the kerogen will produce porosity in the organic matter. Valenza et al., (2013) observed an increase of the specific surface of the organic matter from 50 m^2/g on immature samples to 400-600 m^2/g on post mature samples. This is consistent with the development of porosity as a function of maturity. However the weakness of the trend observed by Curtis et al., (2012a) suggests that the origin of the organic matter could play an important role on the generation of organic porosity or possibly the inadequacy of the Ro (%) measurements.

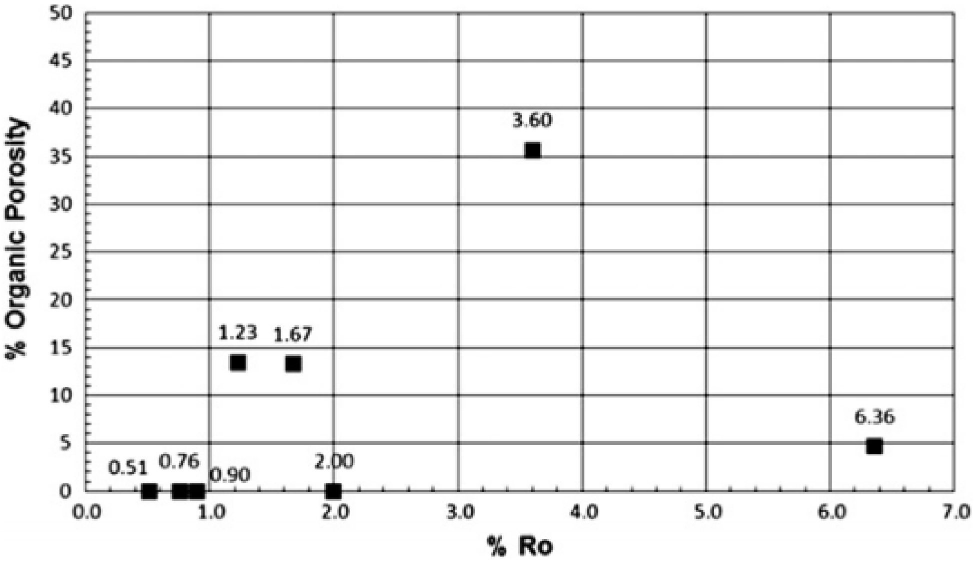

Figure 1.1.8: Intrinsic organic porosity as a function of thermal maturity (Curtis et al., 2012a). A weak positive correlation can be observed. This implies that maturity is not the only controlling factor on the generation of organic pores.

In the oil window the development of porosity is less understood. Curtis et al., (2012b) have reported the presence slit shape pores within the organic matter of the oil window of Woodford while Laughrey et al., (2013) observed some spherical pores in the oil producing part of the Niobrara (**Figure 1.1.9**). This put more emphasis on the need to investigate the type of organic matter contained in these shales and a call for more accurate maturity index.

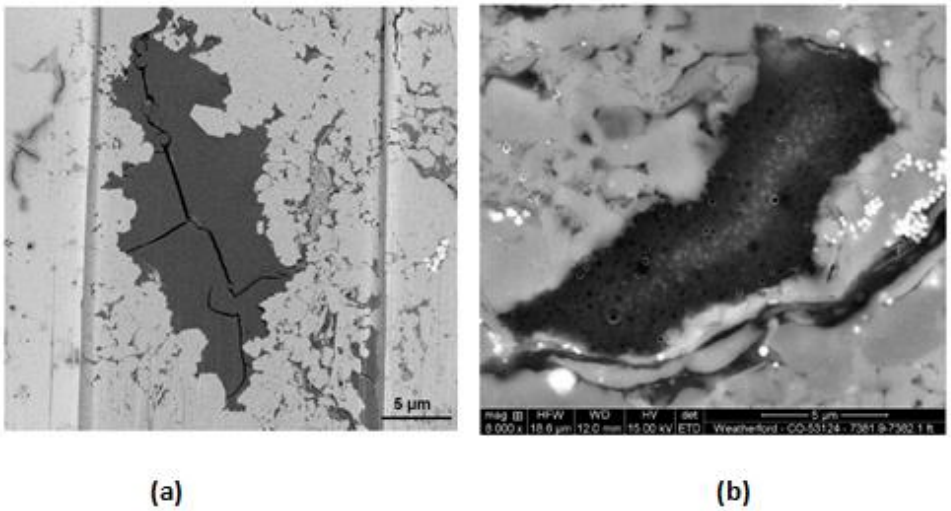

Figure 1.1.9: Types of organic pores in oil window. (a) shows crack like pores in the organic matter (Curtis et al., 2012) while (b) shows more spherical pores in the organic matter (Laughrey et al., 2013).

1.1.4. Hydrocarbon storage mechanism

Several storage mechanisms have been investigated in shales. These mechanisms depend on the fluid type and the pore size.

In the dry gas window, natural gas in shales can be stored as compressed gas in the organic and inorganic pores (free gas), adsorbed on the surface of organic matter, and as dissolved in the formation brine (Cluff et al., 2007; Ambrose et al., 2010; and Campos et al., 2009). At low moisture content natural gas can also be adsorbed on some clays (Chalmers and Bustin 2010). The presence of adsorbed gas and nanometer size pores can have a significant impact on the calculation of the amount of gas in place.

In conventional reservoirs the amount of free gas G_f (scf/ton) can be quantified with **equation 1.1.2** (Ambrose et al., 2010), where S_w is the water saturation, ρ_b is the sample bulk density in g/cc, B_g is gas formation volume factor and ø is the porosity.

$$G_f = 32.0368\,\frac{\emptyset(1-S_w)}{\rho_b B_g} \qquad 1.1.2$$

Due to the fact that the adsorbed gas will occupy some volume of the free space, Ambrose et al., (2010) proposed a modified form of **equation 1.1.2** to calculate the amount of free gas in shales (**equation 1.1.3).** In equation **1.13**, $\widehat{M}$ is the apparent gas molecular weight (lbm/lbmole), P is the reservoir pressure (psia), P_L is the Langmuir pressure (psia), G_{sL} is the Langmuir storage capacity (scf/ton), and ρ_s is the adsorbed phase density.

$$G_f = \frac{32.0368}{B_g}\left[\frac{\emptyset(1-S_w)}{\rho_b} - \frac{1.318*10^{-6}\widehat{M}}{\rho_s}\left(G_{sL}\,\frac{P}{P+P_L}\right)\right] \qquad 1.1.3$$

The use of **equation 1.1.3** as well as any storage model based on the Langmuir theory requires the knowledge of the adsorbed phase density. The molecular simulation study conducted by Campos (2010) concluded that the adsorbed phase density depends on the pore size and pore pressure. However, there is no method capable of measuring the adsorbed phase density.

Generally not considered in the calculation of the amount of gas in place, the dissolved gas in brine can be important in shale reservoirs. The simulations of Campos et al., (2009) showed that the solubility of methane in brine increases as the pore size decreases (**Figure 1.1.10**).

The storage mechanisms in the condensate window are believed to be similar to the mechanism of dry gas storage. However, in the case of condensate, the thermodynamic behavior of the fluid in the reservoir is of critical importance. The PVT diagrams are believed to be affected by pore confinement (**Figure 1.1.11),** and several authors have predicted shifts in the critical properties of the fluids (Devegowda et al., 2012; Ma et al., 2013; Didar and Akkutlu 2013; Pitakbunkate et al., 2014; and Khoshghadam et al., 2015).

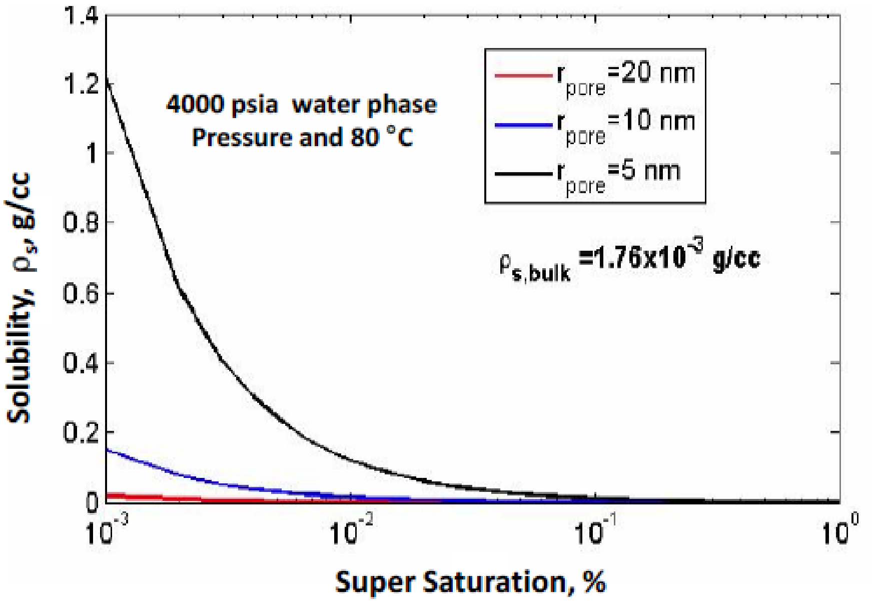

Figure 1.1.10: Methane solubility in brine increases as the pore size decreases (Campos et al., 2009) modified by Honarpour et al., (2012).

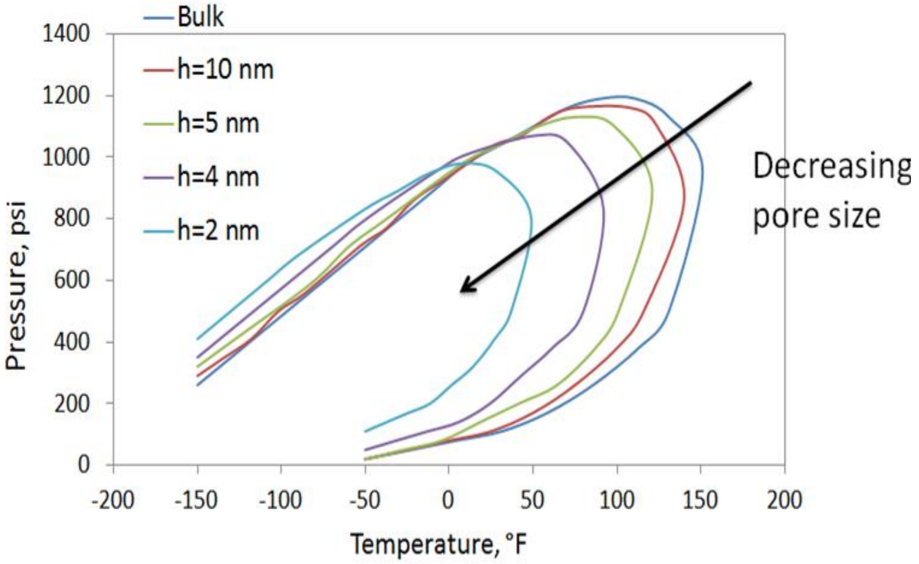

Figure 1.1.11: Change in phase behavior as a function of pore size (Ma et al., 2013). It appears that the change in phase behavior becomes non negligible in pores with radii less or equal to 10nm.

In the oil window, the PVT diagram of the fluid can change as well due to the effect of nanopores. Honarpour et al., (2012) studied the process of gas liberation from oil at the bubble point in nanocapillaries. They postulated that to sustain a bubble in these nanocapillaries, additional pressure differential is needed. This need for additional differential pressure will imply a decrease of the bubble point pressure.

1.1.5. Flow properties in shales

The presence of flow paths at different scales will impact the flow regime in shales. Several flow regimes can be distinguished based on Knudsen number (Kn), which is the ratio of the mean free path of the gas (λ) to the pore radius (r).

$$Kn = \frac{\lambda}{r} \tag{1.1.4}$$

The mean free path is the average distance a gas molecule can move before colliding with another gas molecule. **Figure 1.1.12** shows a plot of the different flow regimes as a function pore size, and pore pressure.

The continuum regime is valid when Kn ≤ 0.001. In this regime the flow is governed by viscous forces and can be modeled with Darcy’s Law. The slip flow regime (0.001 ≤ Kn ≤ 0.1) has received considerable attention in the literature e.g. Klinkenberg (1941), Jones and Owens (1980), Michel et al., (2011), and Fathi et al., (2012). In this regime the no slip boundary condition (continuum regime) is violated by the gas molecules which slip at the pore wall. However, if Darcy’s Law is corrected for the additional flow provided by the slipping molecules, it can be used in this regime.

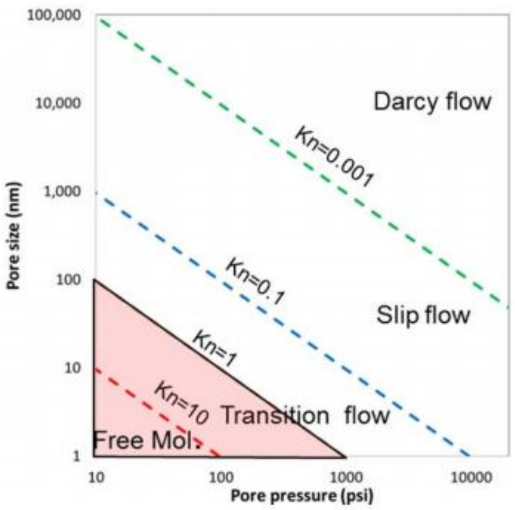

Figure 1.1.12: Flow regimes as a function of pore size and pore pressure for methane (Sinha et al., 2013). The presence of pores from nanometers to microns has made possible the presence of multiple flow regimes in shales.

The most popular correction for gas slippage is the Klinkenberg correction (**equation 1.1.5)** (Klinkenberg, (1941)).

$$k_a = k_\infty \left[1 + \frac{b_K}{\bar{p}}\right] \tag{1.1.5}$$

k_a is the measured gas permeability, $\bar{p}$ is the mean pressure (atm), b_K is the gas slippage factor, and k_∞ is the equivalent liquid permeability. The gas slippage factor is defined by the following equation:

$$\frac{b_k}{\bar{p}} = \frac{4c\bar{\lambda}}{r} \tag{1.1.6}$$

Where r is the effective pore radius, c is a constant close to one, and λ is the mean free path of the gas.

Before the production of hydrocarbon from shale formations, the only flow regimes studied by reservoir engineers were, the continuum and slip flow regimes. However, in shales there has been evidence of additional slippage which could not be explained by a simple Klinkenberg correction (Civan et al., 2011; and Fathi et al., 2012). Fathi et al., (2012) concluded after their lattice Boltzmann simulations of flow in nanocapillaries that Klinkenberg (1941) did not account for the additional momentum brought by the gas molecules that slip at the pores walls. They proposed **equation 1.1.7** to correct for the additional gas slippage. In **equation 1.1.7**, L_{KE} is the length scale associated with the kinetics of the molecules bouncing at the nanopores walls.

$$k_a = k_\infty \left[1 + \left(\frac{b}{\bar{p}}\right)^2 \left(\frac{L_{KE}}{\lambda}\right)\right] \qquad 1.1.7$$

The correction of Fathi et al., (2012) is valid at the limit between the slip flow regime and the transition flow regime. Flow modeling in the transition and molecular flow regime is quite complex; however, several studies have addressed it (Sakhaee-Pour and Bryan 2011; Civan 2010; and Florence et al., 2007) through apparent gas permeability corrections. Civan (2010), based on the original work of Beskok and Karniadakis (1999) published an equation (**equation 1.1.8**) valid for all flow regimes.

$$k_a = k_\infty (1 + \alpha_2 K_n)\left(1 + \frac{4K_n}{1 - bK_n}\right) \qquad 1.1.8$$

The experimental studies by Tinni (2012), Sinha (2013), Pathi (2008) and Ghanizadeh et al., (2013) showed that permeability measurements are extremely stress sensitive and dependent on the flow direction (anisotropy). Permeability could decrease by two or three orders of magnitude over a confining pressure range from to 1000 to 5000 psi. This was attributed to the influence of cracks on permeability measurements. However, the interpretation that permeability is controlled by cracks, needs to be taken with caution because slit shape pores behave like cracks, and the presence of slit shape pores has been reported in shales such as the Haynesville and the Avalon (Curtis et al., 2010). Cui et al., (2009), pointed out the need to measure permeability with reservoir fluids instead of gases such as nitrogen and helium, because of adsorption effects and possibility of molecular sieving. Sinha et al., (2013) and Ghanizadeh et al., (2013) addressed this issue by measuring permeability with reservoir fluids such as methane in steady state conditions and compared them with the measurements with helium and argon. The measurements with methane are always lower than the measurements with helium, but very close to the measurements with argon (**Figure 1.1.13**).

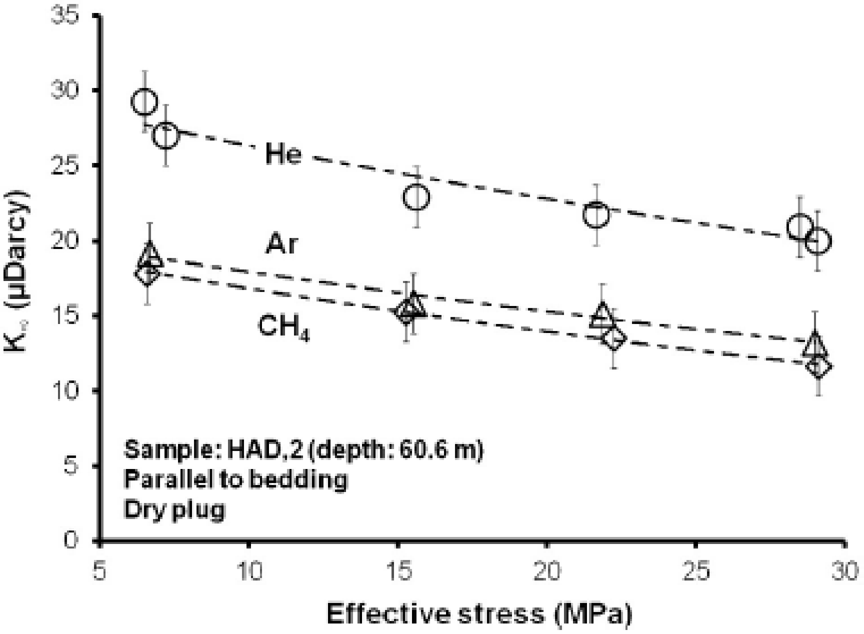

Figure 1.1.13:Permeability measurements as function of effective stress with different gases for a Haddssen shale sample (Ghanizadeh et al., 2013). The effective stress is considered to be equal to simple difference between the confining and pore pressure. These permeability values (in the micro-Darcy range) are very large for shales (usually in the nano-Darcy range)

Argon and methane have a similar molecular diameter (0.34 nm for argon and 0.38 nm for methane), so their mean free paths will be similar in comparison to the mean free path of helium, which has significantly different molecular diameter (0.25 nm).

Steady state permeability measurements with gas at multiple pore pressures can be used to test the validity of Klinkenberg's theory. The Klinkenberg correction only accounts for gas slippage. Therefore, a deviation from Klinkenberg's correction should indicate a change of flow regime.

However, all published steady state permeability measurements show a straight line dependency of permeability as a function of 1/p in a pore pressure range from 20 to 1000 psi (Bertoncello and Honarpour 2013; Sinha et al., 2013; Ghanizadeh et al., 2013; and Soeder 1988). An example of this straight line dependency is illustrated on **Figure 1.1.14**. This observation is counter intuitive (especially in the low pressure range), because the presence of nanometer size pores should have induced a change in flow regime.

Cui et al., (2013) measured the permeability of several Montney shale sample with liquid (decane) and gases (helium and argon). The equivalent liquid permeabilities obtained after Klinkenberg's correction for helium were slightly larger (50 nano-Darcy more) than those for argon. Both equivalent liquid permeabilities were larger than the permeability measured with decane by approximately one order of magnitude. This observation suggests that permeability in shales depends on the measurements fluid.

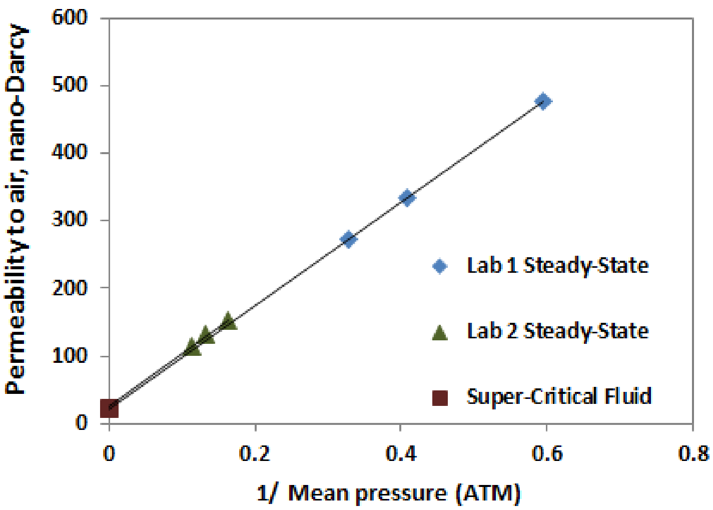

Figure 1.1.14: Steady state permeability measurements at different pore pressures with nitrogen and a super critical fluid (adapted from Bertoncello and Honarpour 2013). A remarkable agreement can be observed between the nitrogen measurements from two different laboratories and the Klinkenberg corrected permeability with the supercritical fluid permeability.

1.1.6. Mechanical properties

To produce at economic rates shale reservoirs have to be stimulated by hydraulic fracturing. This fracturing process is in large governed by the mechanical properties of the rock. The mechanical properties of interest in shales are generally Young's modulus and Poisson's ratio. However, in shales these two properties are dependent on the measurement direction (Sondergeld and Rai 2011; and Sarkar 2008). Shale anisotropy is generally considered to be transverse anisotropy which can be quantified with following anisotropic parameters (Thomsen 1986):

$$\varepsilon = \frac{C_{11}-C_{33}}{2C_{33}} \qquad 1.1.9$$

$$\gamma = \frac{C_{66}-C_{44}}{2C_{44}} \qquad 1.1.10$$

$$\delta = \frac{(C_{13}+C_{44})^2-(C_{33}-C_{44})^2}{2C_{33}(C_{33}-C_{44})} \qquad 1.1.11$$

ε and γ are respectively the compressional and shear wave anisotropy. δ is related to the velocity at polar angles to the principal directions (Sondergeld and Rai 2011). When ε and γ are less than 10% the medium is considered to have a weak anisotropy. However, most of the shales show a strong anisotropy (**Figure 1.1.15**).

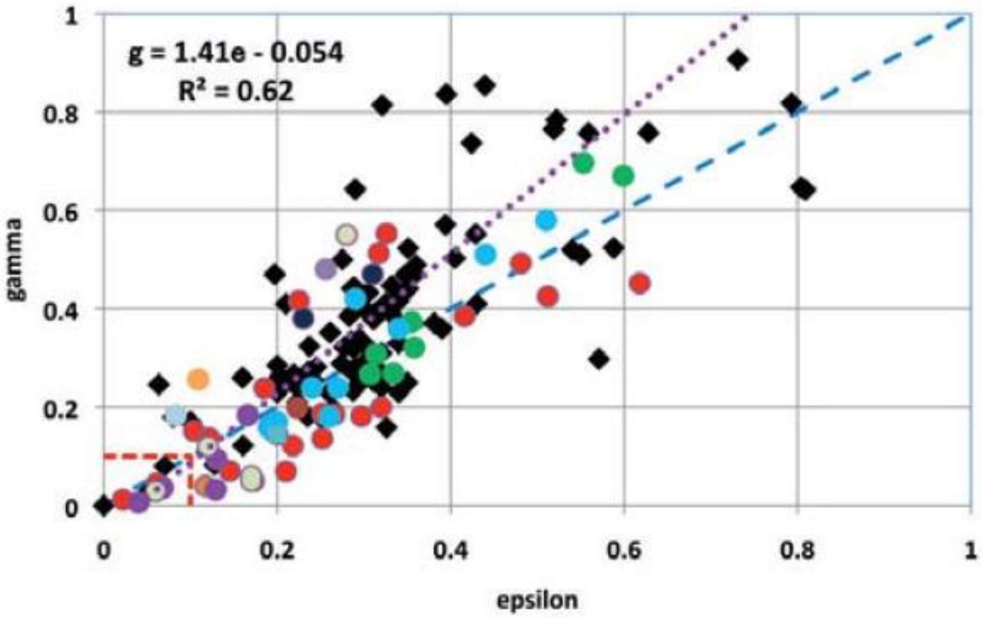

Figure 1.1.15: Plot of γ as a function of ε for shale formations worldwide (Sondergeld and Rai 2011). The weak anisotropy assumption is not valid for most of the shales.

This strong anisotropy will impact the estimation of the fracture closure stress, which is also the minimum horizontal stress:

$$\sigma_h = \frac{E_h}{E_v} * \frac{\nu_V}{(1-\nu_H)}(\sigma_V - \alpha P) + \alpha P \qquad 1.1.12$$

In **equation 1.1.12**, E_h and E_v represent the horizontal and vertical Young's moduli respectively. ν_V and ν_H are the vertical and horizontal Poisson's ratio. α is the Biot coefficient which is also anisotropic (Al-Tahini and Abousleiman 2008) and P is the pore pressure.

In anisotropic rocks such as shales the hydraulic fracture propagation will be governed by the rock fabric at low stress levels and by the applied stress at high stress levels (Sharma and Damani 2013). Young's modulus and Poisson's ratio are used as surrogate for the brittleness of the rock (Rickman et al., 2008). High Young's modulus and low Poisson's ratio rocks are believed to be more brittle (Rickman et al., 2008), hence more "fracable". Clays are considered soft materials, so they tend to have lower Young's modulus and high Poisson's ratio, the inverse of quartz and calcite. Calcite is generally present as filling material between paleo-fracture faces. The weak bonds between the calcite filling material and the shale matrix will facilitate the reopening of these fracture plans during hydraulic fracturing (Gale et al., 2006; and Mighani 2014).

1.2. Objectives

The previous section discussed the state-of-the-art in shale characterization. It can be seen that considerable amount of research has been conducted since the early exploitation of organic rich shales as hydrocarbon reservoirs. Shales are considered to be highly heterogeneous, anisotropic, with low porosity, permeability (which can be enhanced with hydraulic fracturing) and deposited in various environments. Despite the considerable amount of research already published, the complete characterization of shales remains a goal for the scientific community. Measurements such as water saturation which were considered to be routine measurements in conventional reservoirs are extremely difficult to carry out in shales. Relative permeability measurements have not even been attempted.

Hydrocarbon flow properties and storage are among the least understood properties of shales. The flow properties are still elusive because of the lack of understanding of pore connectivity in shales. Several mechanisms have been proposed for hydrocarbon storage, but no experimental work which systematically investigated these mechanisms has been published to date.

In this dissertation, we have developed several experimental programs which investigated pore connectivity in shales based on intrusion of fluids with different polarities. We have studied the pore structure of shales using the combination of different porosity measurements methods, and investigated the relevant mechanisms for hydrocarbon storage and flow.

2 Experimental methods

2.1 Fourier transform infrared method for quantification of mineralogy

Fourier transform infrared (FTIR) is based on the principle of infrared (IR) spectroscopy, i.e., a molecular bond exposed to a light source with a frequency equal its resonant frequency, vibrates due to an energy transfer from the light source. During an FTIR measurement, a polychromatic light source is radiated through the sample. The amount of energy lost at different frequencies due to the vibration of the molecular bonds present in the sample, is measured with a detector. This detector can be mounted before or after the sample, with respect to the optical path of the light source. If the detector is mounted before the sample, the measurement is a reflection FTIR, and when the detector is after the sample, the measurement is called transmission FTIR. Our FTIR spectrometers work on the transmission principle in the mid-infrared range (4000-400 cm^{-1}).

The amount of energy loss is generally quantified as total absorbance. In transmission FTIR, the total absorbance of a rock sample depends on the type of minerals present, their amount and the thickness of the sample. The total absorbance is related to the minerals present and their amount by Beer's Law:

$$A = \sum_{i=1}^{n} \varepsilon_i l c_i \qquad 2.1.1$$

Where A represents the total absorbance, ε_i is the absorptivity of the ith mineral, l is the optical path length and c_i is the concentration of the ith mineral. Beer's Law allows the quantification of the minerals present in a true quantitative manner as opposed to X-ray diffraction which is a semi-quantitative. The application of Beer's Law requires the establishment of a library which will contain the spectra of minerals of interest at different concentration (Sondergeld and Rai 1993; and Ballard 2007). **Figure 2.1.1** shows examples of the FTIR spectrum of 6 common minerals in sedimentary rocks.

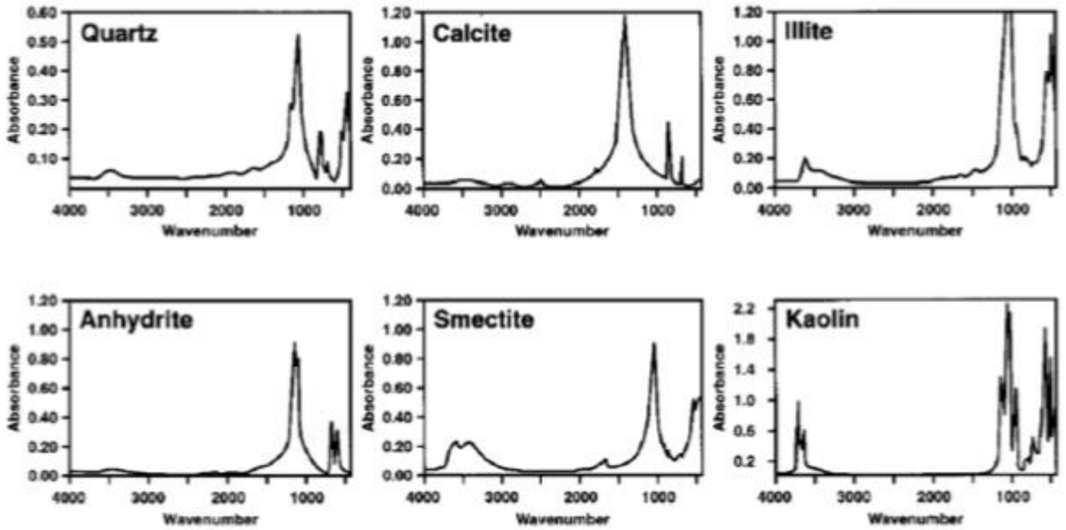

Figure 2.1.1: FTIR spectrum of several common minerals in sedimentary rocks.

Our inversion library contains 16 minerals, which are quartz, calcite, dolomite, siderite chlorite, illite, kaolinite, smectite, mixed layer clay, albite, oligoclase, orthoclase, anhydride, apatite, pyrite, and aragonite.

Prior to FTIR measurements on the samples, 0.3 g of potassium bromide (KBr) is pressed in 1 mm thick pellet by compression at 10 tons under vacuum. The KBr pellet is used to measure the background signal of the FTIR spectrometer. KBr is good for background measurements because it has no vibration frequencies in the mid-infrared range.

The shale samples selected for FTIR measurements are crushed into fine particles (<2 5 μm). The crushed samples are dried at 100 °C for 12 hours and oxidized in a low temperature (< 90 ^{o}C) plasma asher until all organic matter is removed. It is important to remove the organic matter, because organic matter has FTIR peaks that overlap with several clay FTIR peaks (Dang 2013). The ashed samples are dried at 100 ^{o}C for at least 12 hours.

0.0005 g of the prepared sample is mixed with 0.2995 g of KBr and pressed into a 1 mm thick pellet for FTIR measurement.

2.2 Determination of TOC

The amount of organic matter contained in shales is quantified as total organic carbon (TOC). We have measured TOC on all the shale samples used in our studies with a LECO C844™ instrument. In practice, this instrument measures the total carbon contained in the sample by combusting the sample at 1200 ^{0}C in a high frequency induction furnace, and quantifying the total carbon content by measuring the IR signal of combustion products.

In order to measure only organic carbon we treated our samples (0.1 ± 0.01g) with 10-15% hydrochloric acid. The acidized sample is washed with deionized water in order to remove acid and residues from the acidizing process. Prior to the introduction in the LECO C844 furnace, the sample is dried at 100 ^{0}C for 15 minutes. TOC is reported as weight percentage.

2.3 Crushed helium porosity measurement

In conventional reservoir rocks, porosity is generally measured on core plugs by helium pycnometry (API 1998). In unconventional rocks such as shales, the low permeability (sub microdarcy) precludes accurate porosity measurements on core plugs because of the time it takes for helium to diffuse through the sample. The crushed rock helium porosity method is the standard method for porosity measurements in shales.

During our measurements, we followed the recommendation of Karastathis (2007). The bulk volume of 6 to 11 g of a solid rock sample is measured by mercury immersion. The selected rock sample is crushed to submillimeter particle size **(Figure 2.3.1**) in a special crucible (**Figure 2.3.2**).

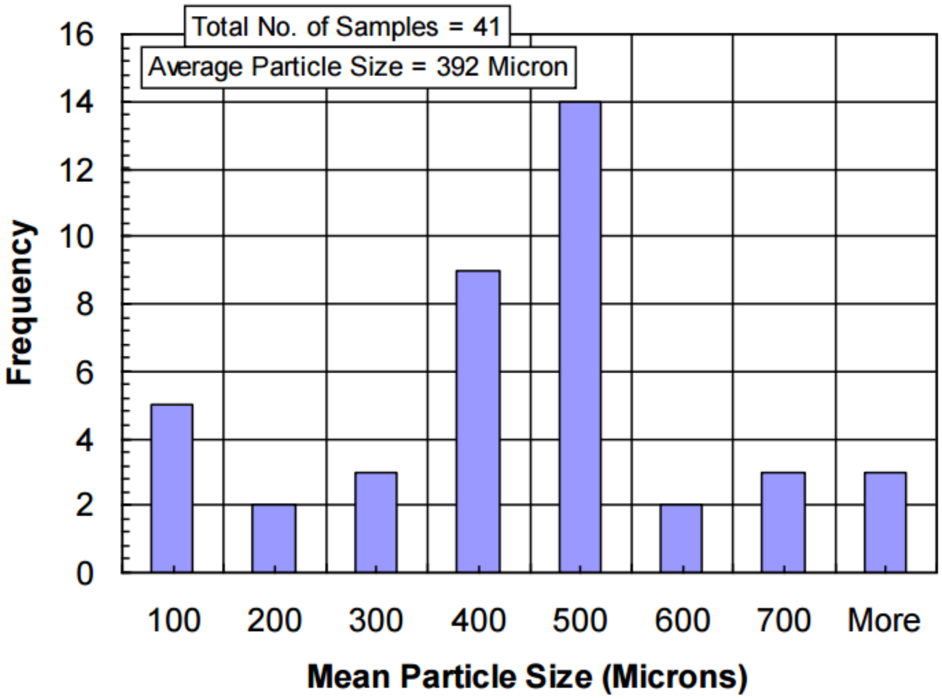

Figure 2.3.1: Mean particle size frequency in 41 crushed Barnett shale samples (Kale 2009). The variation in mean particle size is mainly controlled by the sample mineralogy.

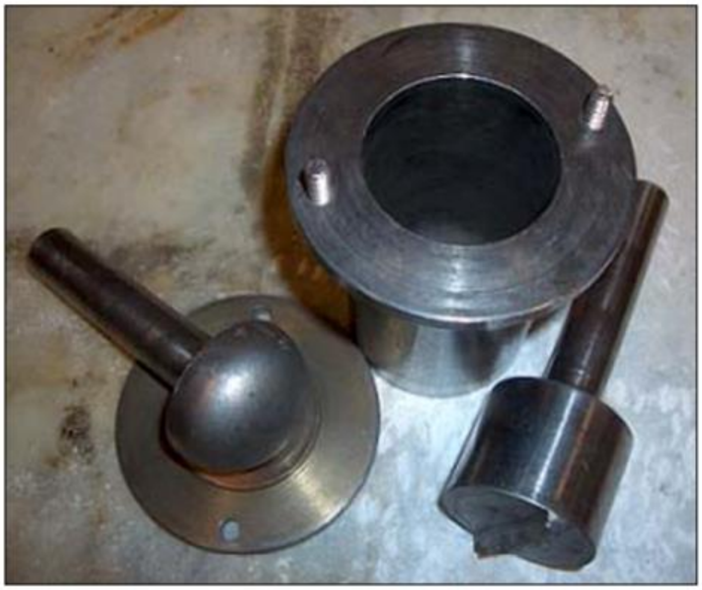

Figure 2.3.2: Photograph of crucible and pestles used to crush the rock samples. The assembly is designed to prevent sample loss during the crushing process.

The crushed sample is removed from the crucible and weighted. The weight difference tolerated between the solid and crushed sample is less or equal to 0.1% of the solid weight. The crushed sample is heated at 100 ^{0}C for a minimum of 12 hours in a convection oven. After heating, the crushed sample is cooled to room temperature in a desiccator for 30 minutes before being reweighted. Helium grain volume is measured on the crushed sample by helium pycnometry at a pressure of 15 psi. This grain volume is adjusted for weight loss with the following formula:

$$V_{\tilde{G}} = V_G + \frac{\Delta m}{\rho_G} \qquad 2.3.1$$

Where $V_{\tilde{G}}$ is the adjusted grain volume, V_G is the measured grain volume, Δm is the weight loss, and ρ_G is the grain density based on the measured grain volume. Porosity is calculated with **equation 2.3.2**.

$$\emptyset = \frac{V_B - V_{\tilde{G}}}{V_B} \qquad 2.3.2$$

In **equation 2.3.2** V_B represents the sample bulk volume.

This porosity value will be a measure of effective porosity because the 100 °C heating process does not remove the bound water (Karastathis 2007, Sondhi 2010).

2.4 Mercury intrusion capillary pressure measurements

Mercury intrusion capillary pressure (MICP) is the quantification of the amount of mercury intruded in a sample at different pressure steps. Our MICP measurements are conducted on 8 to12 g of solid rock samples that were dried at 100 °C for at least 12 hours. After drying, the samples are cooled to room temperature in a desiccator for 30 minutes.

A sample prepared for MICP measurement is placed in a penetrometer which is glass sample holder with a hollow stem (**Figure 2.4.1**).

The assembly is introduced in the low pressure system of a Micrometrics Autopore IV™, where it is subjected to a vacuum of less than 100 mmHg for an hour. The vacuum step is followed by the injection of mercury through the stem of the penetrometer. The injected mercury is pressurized in logarithmic pressure steps (31 steps) up to a pressure of 27 psi. Mercury completely surrounds the sample before entering the pore space. At 27 psi, the penetrometer filled with mercury is placed in the high pressure system of the Autopore IV instrument, where the mercury is compressed with mineral oil in logarithmic pressure steps (132 steps) up to a pressure of 60,000 psi.

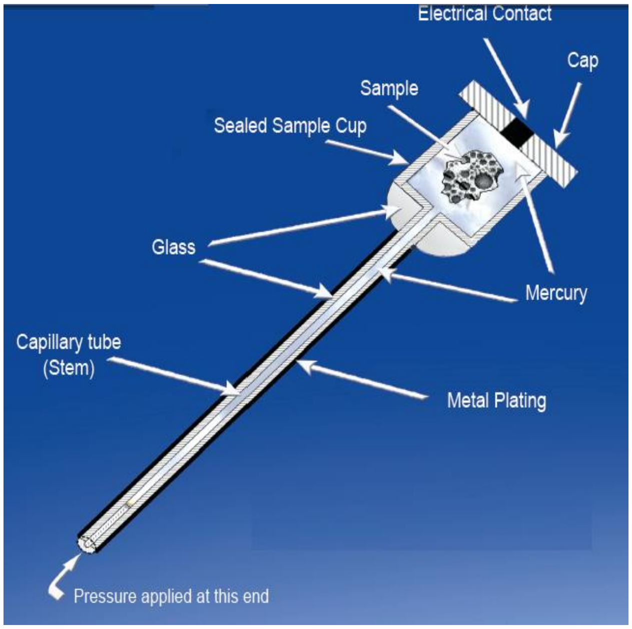
Electrical Contact
Cap
Sample
Sealed Sample Cup
Glass
Mercury
Capillary tube
(Stem)
Metal Plating
Pressure applied at this end

Figure 2.4.1: Cross sectional view of a penetrometer loaded with a sample and mercury (www.micrometrics.com). Mercury is injected and pressurized through the stem.

Mercury is non wetting to most materials. Therefore, its penetration through the pore space is controlled by the Washburn equation:

$$r = \frac{2\gamma \cos(\theta)}{P_{cap}} \qquad 2.4.1$$

Where the radius r is in cm, P_{cap} is the corresponding capillary pressure in dyne/cm^2, γ is the interfacial tension (dyne/cm) for the system air-Hg (480 dyne/cm), and ϴ is the contact angle (140°).

Generally, 5000 psi is the minimum pressure required to start the intrusion of mercury in the pore space of shales (Kale 2009, Sondhi 2011). This high pressure required for intrusion can compress the rock and reduce the size of compliant pores. MICP does not detect microcracks because of their low compliance. Therefore the pore throat size obtained after an MICP experiment could be an underestimation of the pore throat dimension in reservoir conditions.

2.5 Nuclear Magnetic Resonance

Nuclear Magnetic Resonance (NMR) measurements characterize the magnetic properties of nuclei exposed to external magnetic fields at their resonant frequencies. Nuclei have magnetic properties because of the electrical charge of their protons and their spins. For oil field application, we focus on the properties of the hydrogen atom at a frequency of 2MHz. How the magnetic field is applied determines the type of NMR measurement. In the present dissertation we have conducted NMR T_1, T_2, and simultaneous T_1-T_2 measurements.

Our T_1 measurements were conducted with an inversion recovery pulse sequence (Green Imaging Technology 2009). The inversion recovery pulse sequence starts with a 180° radio frequency (RF) magnetic pulse followed by a 90° RF magnetic pulse and the measurements of the induced magnetization (**Figure 2.5.1**).

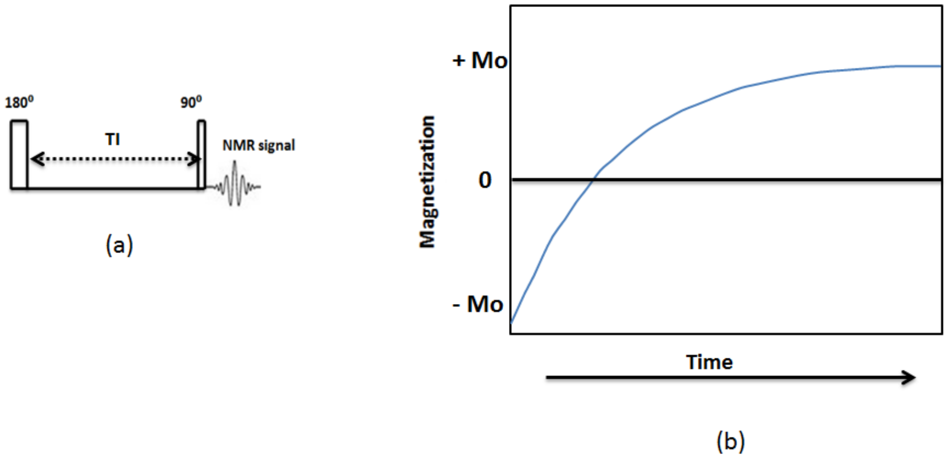

Figure 2.5.1: Schematic representation of an inversion recovery pulse sequence (a) and the shape of the raw data obtain after an inversion recovery sequence (b). The measured NMR signal is called echo.

The time between the 180° and the 90° RF magnetic pulses is called TI. This sequence of magnetic pulses is repeated with increasing TI values until the measure magnetization does not change.

T_2 is measured with a Carr Purcell Meiboom Gill (CPMG) pulse sequence. A CPMG pulse sequence is the application of a 90^0 magnetic pulse followed by a series of 180° magnetic pulses spaced at a characteristic time named inter-echo spacing (TE) (**Figure 2.5.2**).

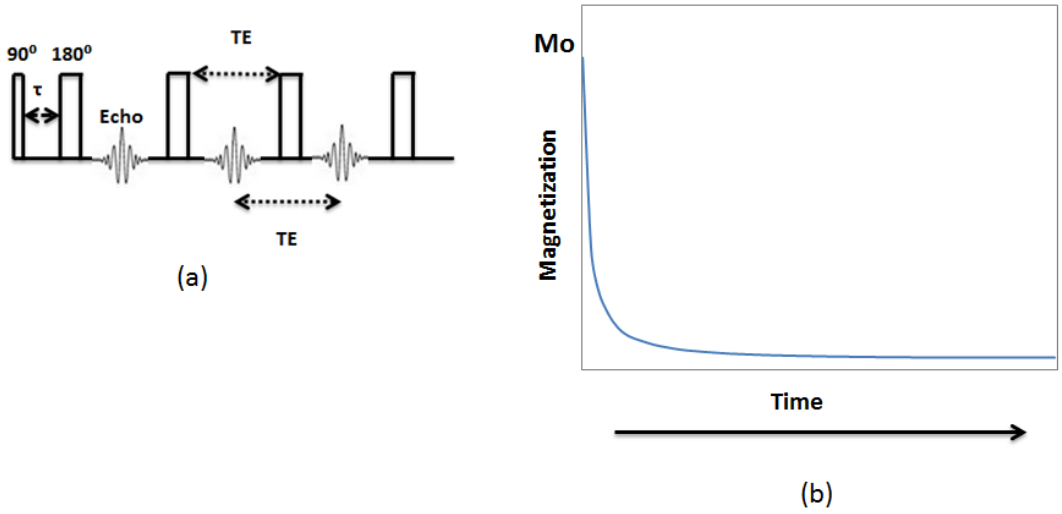

Figure 2.5.2: Schematic of a CPMG sequence (a) and the shape of the raw data obtained after a CPMG sequence. τ is equal to TE/2. The lower the TE value, the shorter the relaxation time which can be observed.

During a CPMG experiment, enough echoes should be acquired to ensure the relaxation of all the protons. The total number of echoes captured after a CPMG experiment represent an echo-train. To quantify the change of fluid content in a sample before and after a treatment, the echo-train acquired before the treatment is subtracted from the echo-train acquired after the treatment. The resultant echo-train is then inverted in a new spectrum representing the changes due to the treatment.

The CPMG and inversion recovery sequences are repeated continuously and their data are stacked in order to provide a good signal to noise ratio (SNR). In the present studies, the minimum SNR was 50. The raw data obtained from CPMG and inversion recovery experiments are inverted with multi-exponentials fitting algorithms to obtain the NMR T_2 and T_1 spectra. These spectra represent the distribution of fluids in the samples. The shapes of the spectra are controlled by the fluid types, pore sizes, and pore walls chemistry.

The areas under the T_1 and T_2 distributions are directly proportional to the amount of hydrogen based fluids present in the sample. Therefore, fluids with different hydrogen concentration i.e. hydrogen index (HI) will have different proportionality constants (calibration factor). All of our initial NMR porosities are based on a calibration factor determined for deionized water with **equation 2.5.1**.

$$porosity\ (\emptyset) = \frac{Area\ \ under\ NMR\ spectrum}{Number\ of\ scans * calibration\ factor * bulk\ volume} \qquad 2.5.1$$

To convert the water based NMR porosities to the specific fluids present in the rocks we used **equation 2.5.2**.

$$\emptyset_f = \frac{\emptyset_w}{HI} \qquad 2.5.2$$

Where $\emptyset_f$ is the specific fluid porosity, $\emptyset_w$ is the water based porosity, and HI is the hydrogen index of the fluid considered. Water and light oil have a hydrogen index essentially equal to 1(Dunn et al., 2002). However, gases have hydrogen indices significantly different than 1. The hydrogen index of a pure gas can be computed with the following equation (Hirasaki et al., 2002):

$$HI = \frac{\rho N_H/M}{0.111} \qquad 2.5.3$$

Where ρ is the gas density (g/cc), N_H is the number of hydrogens atoms contain in the gas molecule, and M is the molecular weight (g/mol).

In addition to the T_1 and T_2 data, we have acquired NMR T_1-T_2 data. While T_1 and T_2 are used to quantify porosity and understand the pore structure we used NMR T_1-T_2 to identify the type of fluids present in the samples based on viscosity contrasts. NMR T_1-T_2 data are acquired with a T_1-T_2 pulse sequence which is the insertion of a CPMG sequence, within an inversion recovery sequence (**Figure 2.5.3**).

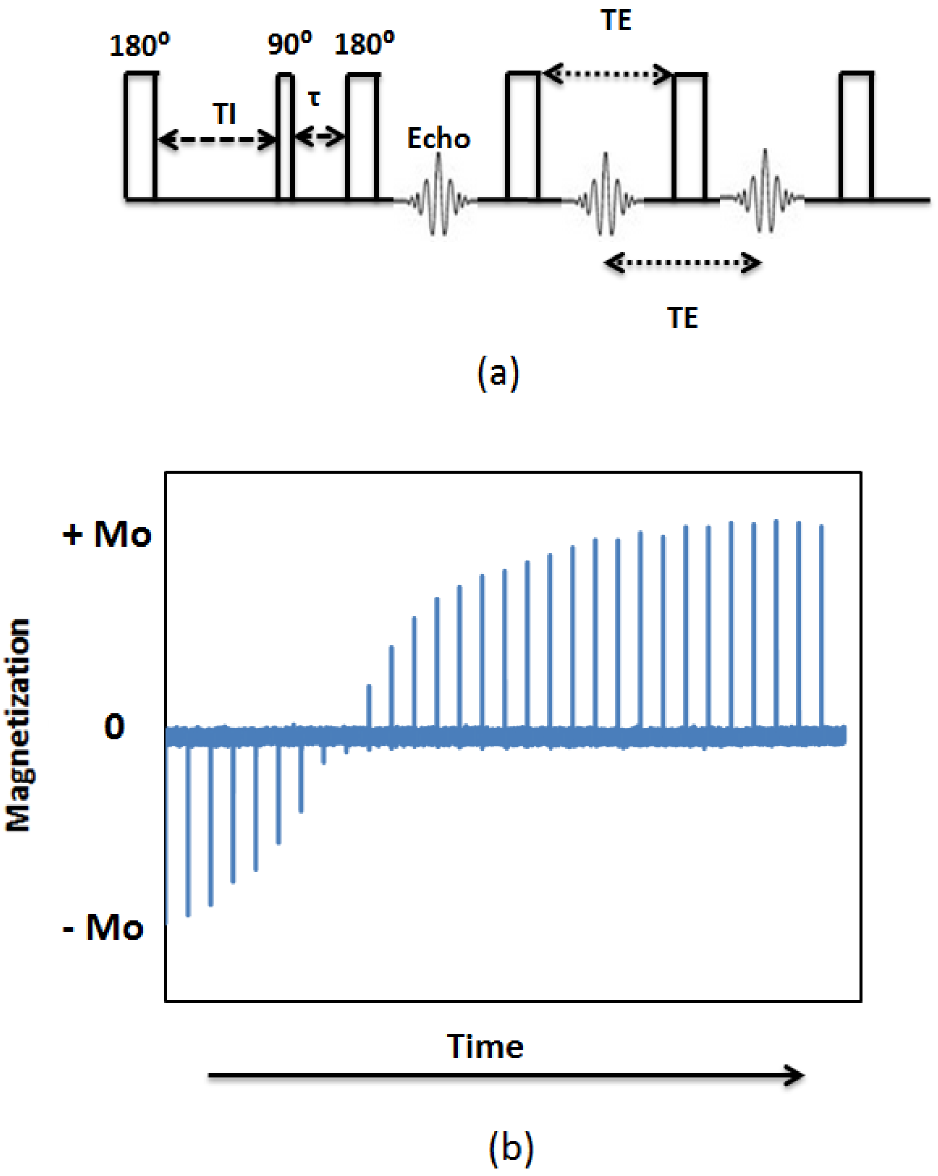
180°
90°
180°
TE
TI
τ
Echo
TE
(a)
+ Mo
Magnetization
0
- Mo
Time
(b)

Figure 2.5.3: Schematic of a T_1-T_2 sequence (a) and the shape of the raw data obtained after a T_1-T_2 sequence (b). The spikes observed are the first echoes acquired at every TI.

The raw T_1-T_2 data are inverted in the Laplace domain to obtain T_1-T_2 correlation maps where every T_1 signal is associated a T_2 signal.

Using the BPP theory (Bloembergen et al., 1948) it is possible to compute the values of T_1 and T_2 as a function of viscosity for simple fluids in their bulk states (**Figure 2.5.4**). It appears that highly viscous fluids will have short T_2 and longer T_1 while the bulk relaxation of a moveable fluid is characterize by T_1=T_2. Therefore the T_1/T_2 ratio can be used differentiate the type of fluids if the viscosity contrast is large enough (Hirasaki and Mohanty 2008; and Tinni et al., 2014).

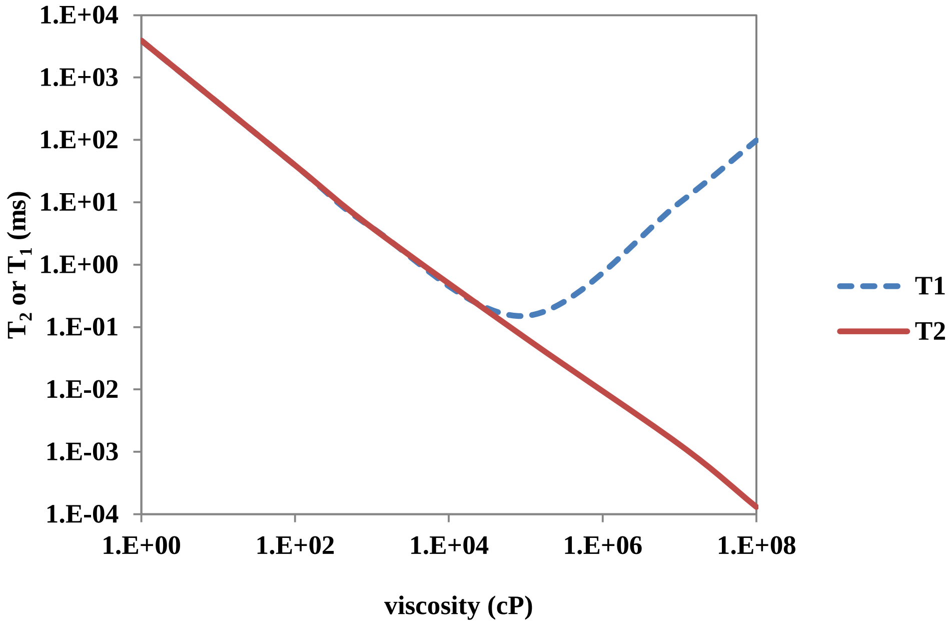

Figure 2.5.4: Theoretical estimation of the values of T_1 and T_2 based on the BPP theory (Bloembergen et al., 1948). These estimations are conducted by increasing the viscosity of water.

2.6 Subcritical nitrogen adsorption experiments

During the subcritical nitrogen adsorption experiments the samples are placed in liquid nitrogen bath (77° K), and nitrogen gas is injected in the samples at small pressure increments (48 steps) up to a relative pressure (ratio of measured pressure P over the saturation pressure P_o) of 1. After the relative pressure reaches 1, the pressure is decreased in small steps (38 steps). This process results in isotherms of nitrogen adsorption and desorption (**Figure 2.6.1**). Prior to the subcritical nitrogen adsorption experiments the samples were heated at 100 ^{0}C under vacuum for 12 hours.

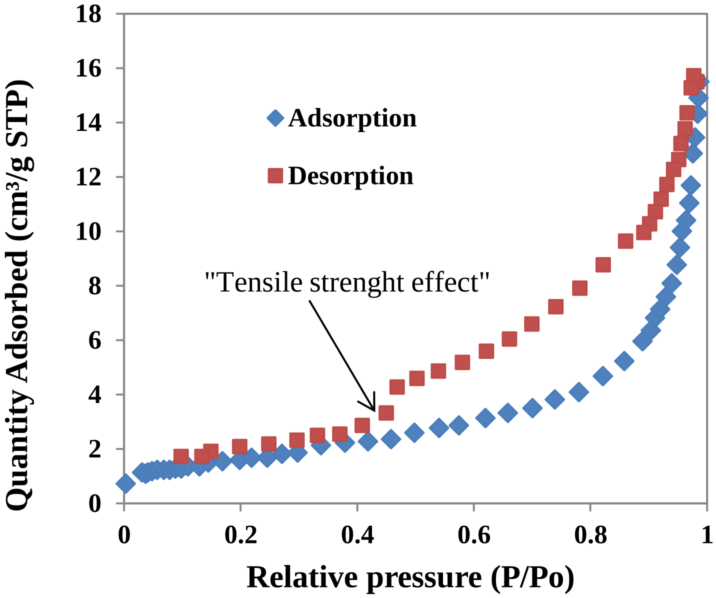

Figure 2.6.1: Typical subcritical nitrogen adsorption and desorption isotherms for a shale sample. The shape of the adsorption and desorption isotherm as well as the shape of the hysteresis loop can be used to infer pore sizes and shapes. The sudden pressure drop on the desorption curve at P/Po = 0.4-0.5 is due to a non stable meniscus in micropores (“ Tensile strength effect”)

2.6.1 BET theory for surface area calculation

The BET theory (1938) is an extension of the Langmuir theory for multilayer adsorption. Brunauer et al., (1938) derived **equation 2.6.1.1** to model multilayer adsorption processes.

$$\frac{1}{Q[\left(\frac{P_o}{P}\right)-1]} = \frac{1}{Q_m C} + \frac{C-1}{Q_m C}\frac{P}{P_o} \qquad 2.6.1.1$$

In **equation 2.6.1.1**, Q is the intake of gas (standard cubic centimeter per grams), P_o/P is the ratio of the actual pressure (P) to the saturation pressure of the measurement gas (Po), Qm is the amount of adsorbed gas forming a monolayer and C is constant representing the heat of enthalpy.

After a nitrogen gas adsorption experiment, $\frac{1}{Q[\left(\frac{P_o}{P}\right)-1]}$ is plotted as function P_o/P; such plot is known as a BET transform plot is (**Figure 2.6.2**). The BET transform plot generally established for $0.05 \leq P/P_o \leq 0.35$, because it yields a straight line within that pressure interval.

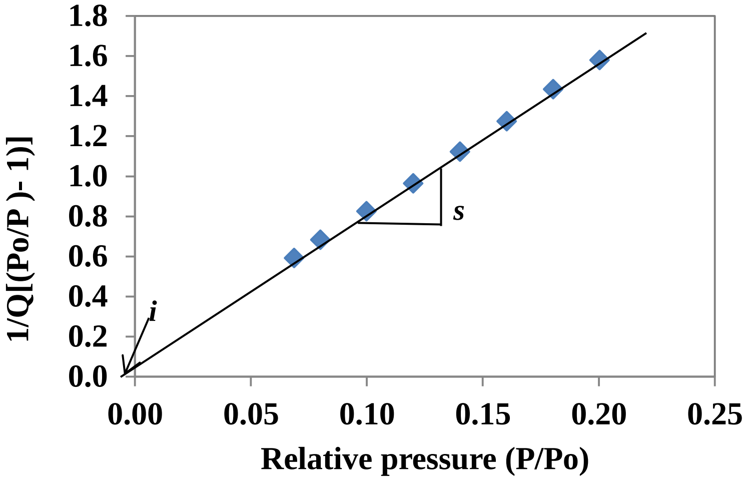

Figure 2.6.2: Example of BET transform plot. The monolayer storage capacity can be calculated from the slope and intercept.

From the BET theory, the intercept of the straight line on **Figure 2.6.2** is defined by **equation 2.6.1.2**.

$$i = \frac{1}{Q_m C} \qquad 2.6.1.2$$

The slope s is defined by **equation 2.6.1.3**.

$$s = \frac{C-1}{Q_m C} \qquad 2.6.1.3$$

From **equation 2.6.1.2** and **equation 2.6.1.3**, the monolayer capacity can be computed and the total surface area (S_t) is calculated with **equation 2.6.1.4.**

$$S_t = \frac{Q_m A N_a}{M} \qquad 2.6.1.4$$

A represents the cross sectional area of the N_2 molecule (16.2 nm^2). N_a is Avogadro's number and M is the molecular weight of N_2. The specific surface area is obtained by dividing the total surface area by the weight of the sample.

2.6.2 Pore size distribution from nitrogen gas adsorption data

During the adsorption process, physio-sorption and capillary condensation occur one after the other in every pore (Gregg and Sing 1982). Capillary condensation occurs in small pores at low pressures and in large pores at higher pressures. During the desorption process, evaporation should occur first in the large pores. However, in the presence of interconnected pores with small pore throats, large pore bodies will not be emptied unless the pore throat with smaller diameter is emptied. Therefore the desorption curves contain information about pore throat sizes while adsorption curves contain information about the pore bodies and pore throats. However, the desorption isotherm is generally characterized by a sudden drop in pressure around P/P_o = 0.4-0.5. This sudden drop is known as the "Tensile strength effect" and is due to a non stable meniscus at relative pressures of 0.4-0.5. The "Tensile strength effect" generally occurs in samples with pores around 4 nm (Groen et al., 2003). Therefore, the desorption curve is not usable for pore size inversion in most shales.

The adsorption data is inverted for pore size distribution using a Density Functional Theory (DFT) algorithm for *carbon slit* pores. Knowing the intermolecular, intramolecular and solid-fluid potential energies, the DFT algorithm is used to build a library of adsorption capacity as a function of pore size. This library is used to match the experimental data and provide a pore size distribution (Do and Do 2003).

3 Pore connectivity in shales

3.1 Concept of pore connectivity

Pore connectivity measures how the pore system is connected throughout a volume of rock. It is a physical concept which is often thought to be measured by permeability or effective porosity in conventional reservoirs rocks.

Shale permeability measurements are often affected by the presence of fractures which act as bypass conduits (Luffel et al., 1993; Handwerger et al., 2011; and Tinni et al., 2012, Mathur 2015), and effective porosity is still an elusive concept in shales. The standard methods used to evaluate pore connectivity in conventional rocks are not applicable in shales.

Several authors (Sisk et al., 2010; Curtis et al., 2011; and Peng et al., 2014) have used the combination of focused ion beam (FIB) and scanning electron microscopy (SEM) to build 3D volumes of several shale samples. From the 3D shale volumes, they extracted the connected and non connected pore systems and studied the connectivity levels in the samples. However, as mentioned by Curtis et al., (2011) the extraction of the pore spaces from 3D volumes relies on the establishment of subjective gray scales thresholds for the pore systems; hence the resultant pore spaces will be strongly dependent on the researcher.

Kale (2009), Hu et al., (2014), Klaver et al., (2015) and King et al., (2015) used mercury injection capillary pressure (MICP) to study pore connectivity in shales. They reported that mercury starts to intrude the shale samples at pressures greater than 5,000 psi. This translates into pore throat diameters smaller than 36 nm. The MICP experiment provides a pore throat size distribution, but does not allow the investigation of how the pores are connected. Curtis et al., (2012c) have shown the presence of mercury within organic pores by taking SEM pictures of a shale sample after it underwent an MICP experiment. In order to study which pores are connected and how they are connected Hu et al., (2014) and Klaver et al., (2015) injected Wood's metal in shale samples. Wood's metal is an alloy that melts at 70 °C. During the experiments of Hu et al., (2014) and Klaver et al., (2015), molten Wood's metal was injected in the shale samples at a maximum pressure of 87,000 psi for Hu et al., (2014) and 46,000 psi for Klaver et al., (2015). The smallest pore throats accessible at 87,000 psi and 46,000 psi are, respectively, equal to 2.3 nm and 4 nm. After the injection of Wood's metal, they allow the samples to cool to room temperature while maintaining the maximum pressures. This process solidifies Wood's metal, and the distribution of Wood's metal throughout the samples is studied with the SEM. Both authors observed that Wood's metal penetrated essentially the pores at the edge of the samples, microfractures, and the vicinity of the microfractures. Hu et al., (2014) quantified the concentration of Wood's metal in the middle of the samples as equal to approximately 1/1000th of the concentration at the edges. Wood's metal and mercury are both non-wetting; hence a significant part of the mercury intrusion volumes recorded during MICP on shales did not enter the samples. The false intrusion reflects the compressibility of the shale sample (Bailey 2009; and Mahomad 2014).

The SEM image (**Figure 3.1.1)** shows that shales have pores associated with the inorganic minerals, the organic matter and the combination of organic and inorganic interfaces. This observation implies the existence of 3 different wettability systems; a water wet system associated with the water wet inorganic minerals (clays, quartz and feldspars), a hydrocarbon wet system associated with the organic matter as well as the hydrocarbon wet minerals (carbonates), and the mixed wet system controlled by pores formed by the water wet and hydrocarbon wet components.

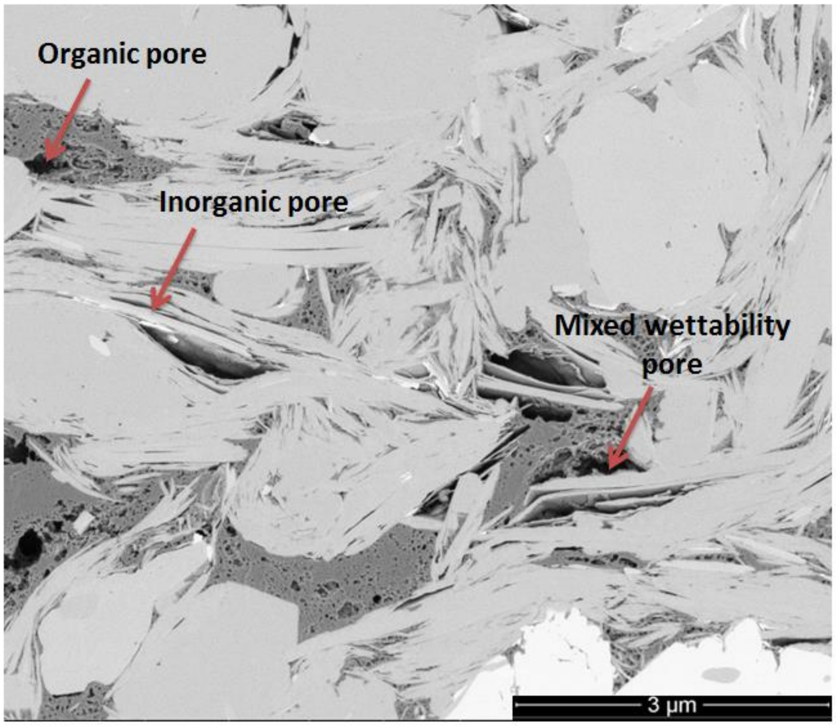

Figure 3.1.1: SEM image of a Marcellus shale sample (Courtesy of Curtis). The pores are associated with the organic phase, the inorganic phase and the combination of both phases. The pores formed by the combination of organic matter and inorganic minerals will have a mixed wettability.

The presence of different wettability systems will affect significantly fluid distribution and its flow. For example, water can enter a clay pore at atmospheric pressure by simple capillary suction while oil can only enter a clay pore after the application of a pressure inversely proportional to the pore size (capillary pressure). However, both fluids can enter the mixed wettability pores at atmospheric pressure. Therefore, every study of pore connectivity needs to take into account the existence of different wettability systems. Studies conducted with non-wetting fluids such as mercury and Wood's metal cannot provide a good understanding of how pores are connected in shales.

Odusina (2011), Sulucarnain (2013), Xu and Dehghanpour (2014) and Hu et al., (2014) recognized the presence of water wet and hydrocarbon wet systems during their imbibition studies, but they were not able to characterize the connectivity levels in each system and how the different wettability systems interact.

In the present study, we have investigated the connectivity of all wettability systems at atmospheric pressure and how it evolves as a function of fluid pressure.

3.2 Pore connectivity at atmospheric pressure

3.2.1 Experimental procedure and samples description

Pore connectivity at atmospheric pressure was investigated with brine (25,000 ppm KCl) and dodecane sequential imbibition data acquired by Odusina (2011) and Sulucarnain (2013) at the Integrated Core Characterization Center of the University of Oklahoma. It is necessary to conduct such studies with the spontaneous imbibition of brine and dodecane because of their respective affinity for water wet and hydrocarbon wet pores.

The imbibition experiments were conducted on 45 shale samples obtained from Haynesville, Woodford, Barnett, Eagle Ford, Floyd, Utica-Collingwood and Wolfcamp formations. The samples from Haynesville, Barnett and Floyd were from the gas window. The samples from Utica-Collingwood were from the condensate window. The Eagle Ford samples were from the gas and condensate windows. The Wolfcamp samples were from the oil window. **Table A-I** in the appendix summarizes the petrophysical properties of the measured samples. Two imbibition sequences were performed on the “As received” sample:

Sequence 1: The samples were immersed in brine for 48 hours, followed by an immersion in dodecane for 48 hours.

Sequence 2: Companion samples from the same depths as the samples used in sequence 1 were used in sequence 2. The samples were first immersed in dodecane for 48 hours, followed by an immersion in brine for 48 hours.

After every immersion step, the amount of brine and dodecane imbibed was quantified by the acquisition of the NMR T_2 spectra of the samples. The NMR measurements were conducted at a TE of 300 μsec on Oxford Maran Ultra™ 2 MHz instruments.

Figure 3.2.1 shows the NMR T_2 spectra acquired for a Barnett sample during sequence 1 as well as the brine and dodecane intakes quantified by NMR.

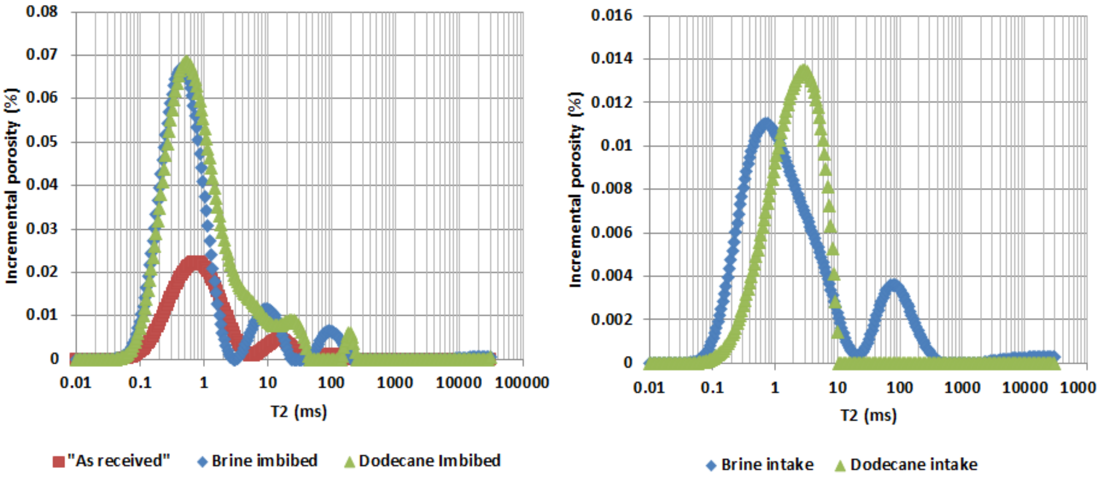

(a) (b)

Figure 3.2.1: NMR T_2 spectra acquired on Barnett shale sample Bxx03 during sequence 1 (a) and brine and dodecane intakes (b). To obtain the brine intake, the echo-train of the “As received” state was subtracted from the echo-train of the brine imbibed state. The dodecane intake was obtained by subtracting the echo-train of the brine imbibed state from the dodecane imbibed state. The echo-train generated after the subtractions is inverted to obtained NMR T_2 distribution in (b).

3.2.2 Results

Figure 3.2.2 and **Figure 3.2.3** show the comparison between the amounts of brine imbibed during sequence 1 and sequence 2, and the amounts of dodecane imbibed during sequence 1 and sequence 2, respectively. The letters in parenthesis within the figure legends are used to indicate that the shale samples are from the gas window (G), the condensate window (C) and the oil window (O).

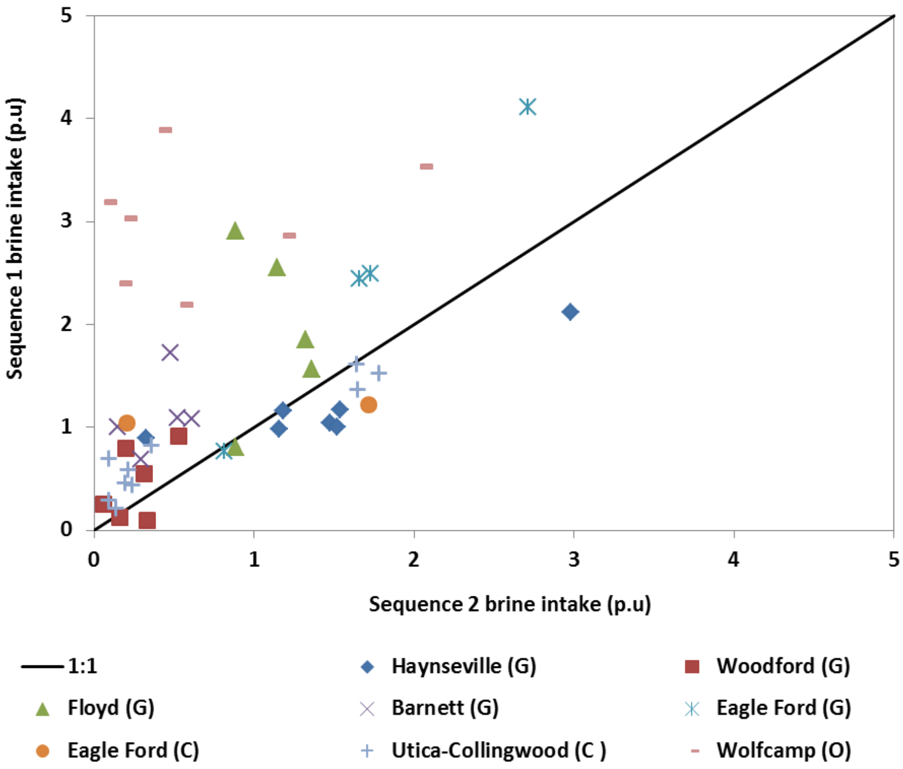

Figure 3.2.2: Comparison between the amounts of brine imbibed during sequence 1 and sequence 2. For most samples, the amount of brine imbibed during sequence 1 is larger than the amount imbibed during sequence 2 in companion samples.

If the water wet flow path is independent from the hydrocarbon wet flow path and vice versa, the amounts of brine imbibed during both sequences will be similar and the amount dodecane imbibed during both sequences will be the same. However, we observe that the amount of brine imbibed during sequence 1 is generally larger than the amount of brine imbibed during sequence 2 (**Figure 3.2.2**). The amount of dodecane imbibed during sequence 2 is generally larger than the amount imbibed during sequence 1 (**Figure 3.2.3**).

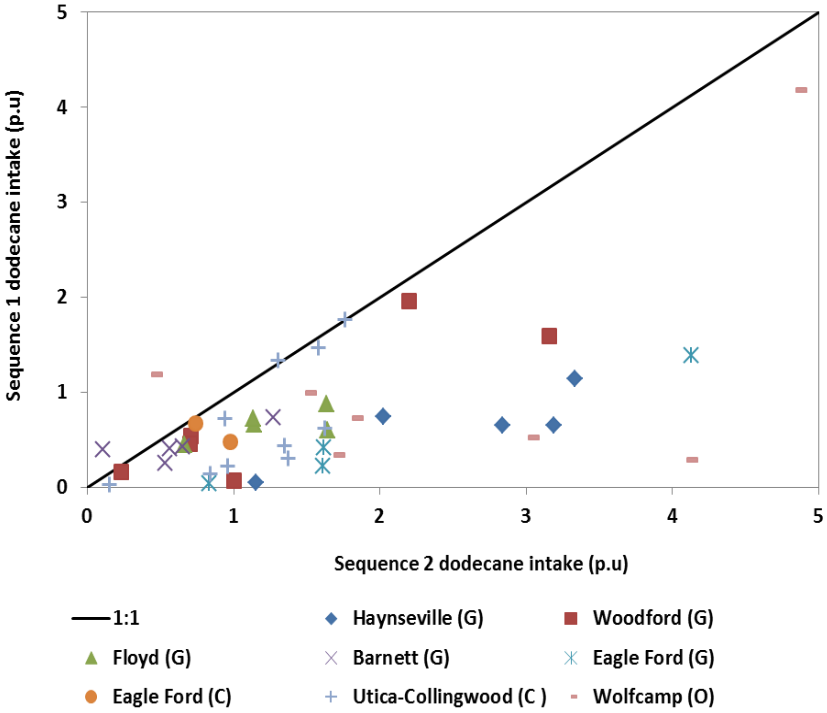

Figure 3.2.3: Comparison between the amounts of dodecane imbibed during sequence 1 and sequence 2 in companion samples. In most samples, the amount of dodecane imbibed during sequence 2 is larger than the amount imbibed during sequence 1.

These observations imply that the presence of brine reduces the accessibility of dodecane to some of the pores it could have accessed if brine was not present. The presence of dodecane prevents brine from accessing some of the pores it can enter in the absence of dodecane. This phenomenon can only be observed if there are pores that are accessible by spontaneous imbibition to brine and dodecane. These pores are the mixed wettability pores.

The fact that the imbibition of brine will affect the subsequent imbibition of dodecane, and vice versa also implies that most of our shale samples do not have a continuous connectivity of the water wet and hydrocarbon wet pores. The connectivity of either flow paths is enhanced by the presence of mixed wettability pores.

Figure 3.2.4 shows a slight negative correlation between the crushed helium porosity and the carbonate content in all shale sample studied except the Eagle Ford samples. Therefore, the porosity associated with the carbonate minerals is generally negligible. This implies that the hydrocarbon wet porosity is essentially contained within the organic matter.

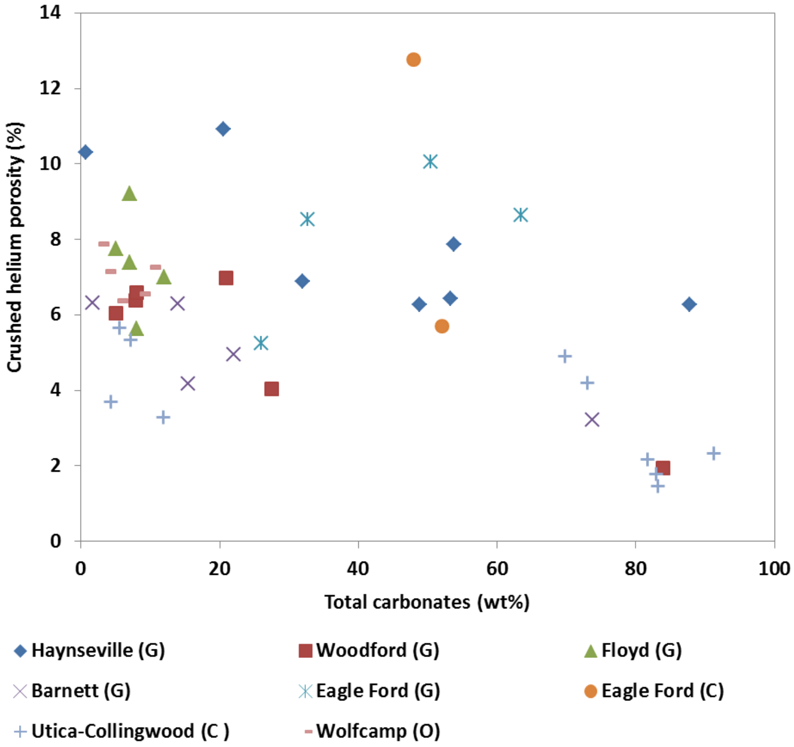

Figure 3.2.4: Crushed helium porosity as a function of the total carbonate content. We observe a negative correlation between porosity and carbonate content except for the Eagle Ford samples.

In **Table A-I** (cf. appendix), it can be seen that the organic content is lower than 10 wt% in all the samples studied. Considering an organic matter density of 1.4 g/cc (Dang et al., 2014) and a shale bulk density of 2.4 g/cc, organic matter will represent a maximum of 18% of the sample volume; thus the organic matter will always be disseminated in connected or non-connected bodies throughout the shale samples. Therefore, during sequence 1, brine will enter all the water wet pores, benefiting from the enhanced connectivity provided by the mixed wet pores; however, during sequence 2, dodecane can only enter the connected hydrocarbon wet pores and the hydrocarbon wet pore accessible via the mixed wet pores. The hydrocarbon wet and mixed wettability pores accessible via water wet pores will not be accessible to dodecane by spontaneous imbibition.

To study the connectivity of the water wet pores it is necessary to block the mixed wet pores with dodecane. During sequence 2, part of the mixed wet pores will be occupied by dodecane. This will give the opportunity to study the connectivity of the water wet pores. However, this connectivity will be affected by the amount of mixed wet pores accessible only through the water wet pores.

Figure 3.2.5 shows the amount of brine imbibed during sequence 2 as a function of the clay content. Below 20 wt% clays, the amount of brine imbibed is less than 0.5 p.u and does not show any correlation with the clay content, implying that the water wet pores are not connected beyond the edges of the samples. Above 20 wt% clay, the amount of brine imbibed exhibits a positive correlation with clay content. Therefore 20 wt% is the minimum amount of clay necessary in order to start the development of a connected water wet pore network. However, when the clay content is greater than 20 wt% we observe two trends for the relationship between the amount of brine imbibed and the clay content.

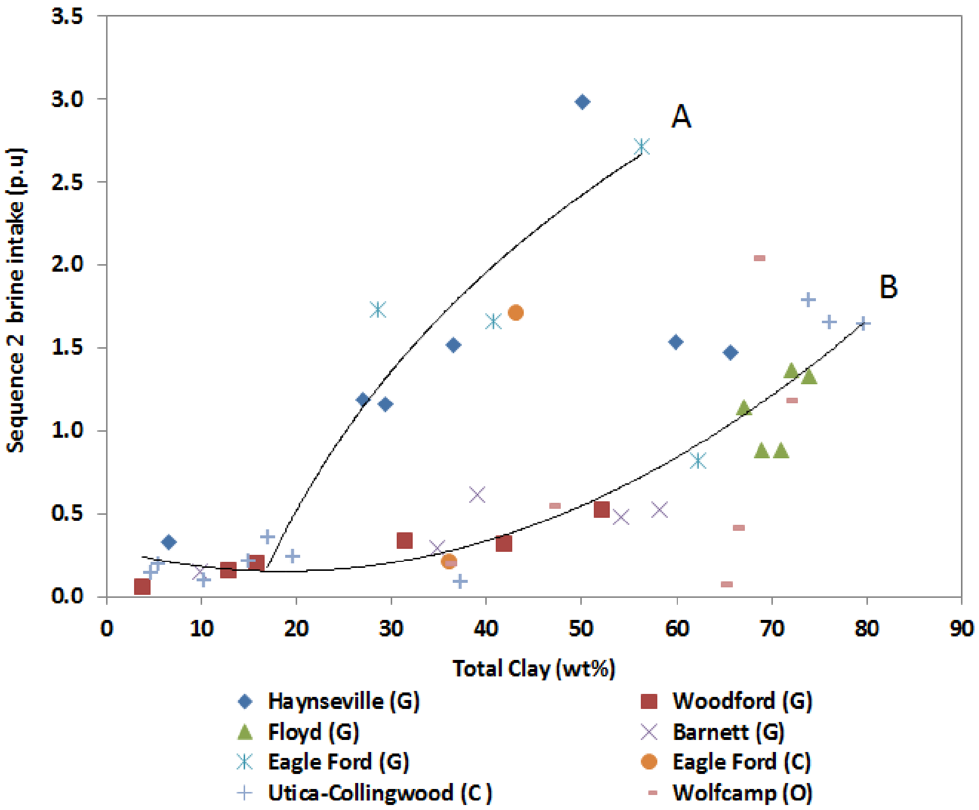

Figure 3.2.5: Amount of brine imbibed during sequence 2 as a function of the total clay content. 20wt% of clays is necessary in order to develop a connected network of water wet pores.

The samples in trend A imbibed more brine than the samples in trend B for the same amount of clays. This observation implies that the samples in trend A have more mixed wet pores only accessible through the water wet pores.

In order to study the connectivity of the hydrocarbon wet pore system we have plotted the amount of dodecane imbibed during sequence 1 as function of TOC **(Figure 3.2.6**). In this case, the water wet as well as the mixed wettability pores are occupied by brine. Below a TOC content of 3 - 4 wt% the amount of dodecane is generally less or equal to 0.5 p.u and does not show any correlation with TOC. Above 3 -4 wt% TOC we observe an increase of the amount of dodecane as a function of TOC implying that a minimum

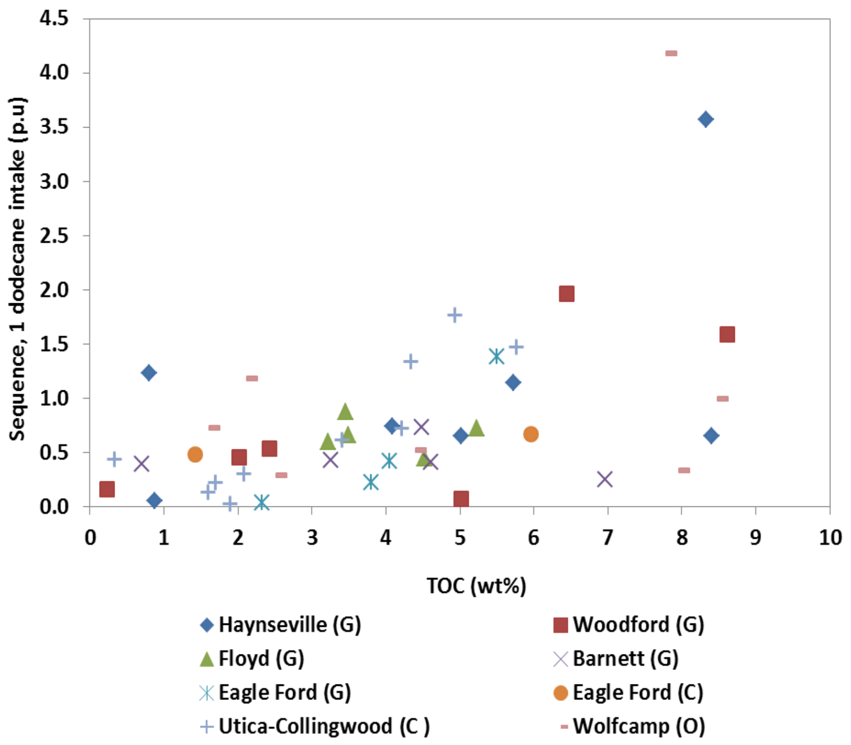

Figure 3.2.6: Amount of dodecane imbibed during sequence 1 as a function of TOC. This plot suggests that a minimum of 3 wt% of TOC is necessary in order to develop connectivity throughout the organic pores.

of 3 – 4 wt% TOC is necessary in order to develop a connected hydrocarbon wet pore network.

The study of connectivity at atmospheric pressure with spontaneous imbibition data may not represent the connectivity during the production of hydrocarbon, because it does not include the hydrocarbon wet pores accessible only via water wet pores. Therefore it is necessary to study the hydrocarbon wet pores connectivity as a function of fluids and pressure.

3.3 Pore connectivity as a function of pressure

In order to study pore connectivity as a function of pressure, we have saturated the 24 samples described in **Table A-II** (cf. appendix) with brine (25,000 ppm KCl) and dodecane. All saturations were conducted by applying a hydrostatic pressure of brine or dodecane. Companion samples from the same depths were used for the brine and dodecane saturation. The change in porosity due to saturation was monitored by acquiring the NMR T_2 distributions at TE=114 µsec with 2 MHz Oxford Geospec2™ instruments.

To determine the pressure necessary to fully saturate the sample we have selected a subset of samples in **Table A-II**, and monitored their change in porosity as a function of saturation pressure (**Figure 3.3.1**). The samples exhibit a rapid change in porosity, from simple spontaneous imbibition to a saturation pressure of 1000 psi. After a saturation pressure of 4000 psi, we observe a plateau in the change of porosity which would imply that the samples were fully saturated. We proceeded and saturated the rest of the samples at 7000 psi with brine and dodecane. At 7000 psi, brine and dodecane can enter respectively non-water wet and non-hydrocarbon wet pores with diameters as small as 4 nm.

Figure 3.3.2 illustrates the comparison between the brine and dodecane saturated porosity. In the majority of the cases, the brine saturated porosity is larger than the dodecane saturated porosity.

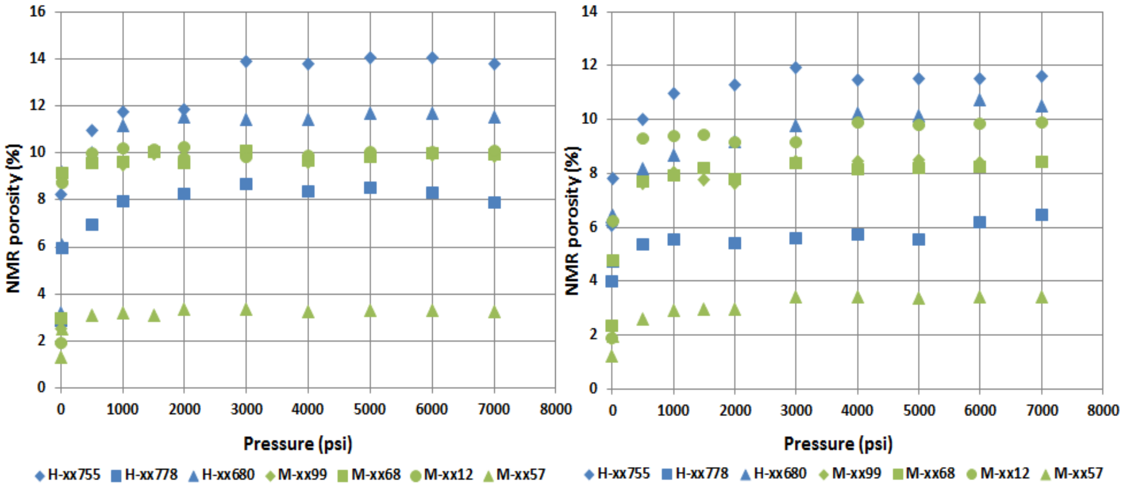

Brine saturation

Dodecane saturation

Figure 3.3.1: Change in NMR porosity as a function of brine and dodecane saturation pressure. Most samples do not show porosity increase after 4000 psi of saturation pressure for both fluids.

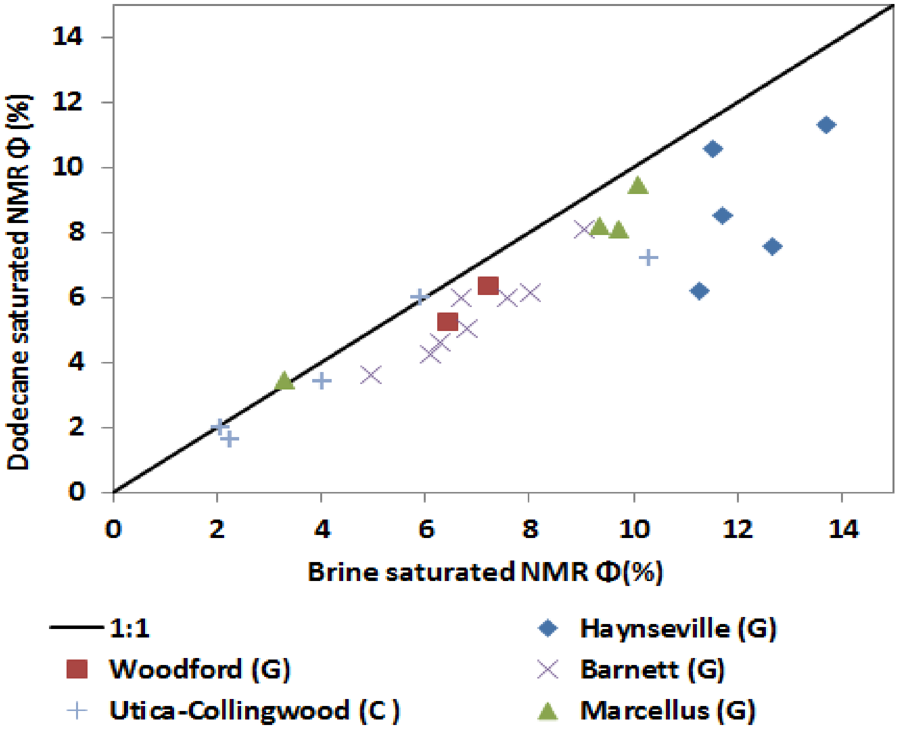

Figure 3.3.2: Comparison between dodecane and brine saturated NMR porosity after saturation at 7000 psi. The brine saturated porosity is generally greater than the dodecane saturated porosity.

The fact that brine porosity at 7000 psi is greater than dodecane porosity at 7000 psi implies that there is a fraction of the pore space that is accessible only through water wet pores with diameters smaller than 4 nm. However, the simple brine and dodecane porosity comparison cannot be used to determine if the majority of the pores accessible through water wet pores smaller than 4 nm are other water wet pores or hydrocarbon wet and/or mixed wet pores.

In order to determine the wettability of those pores, we have analyzed the NMR T_2 distributions of the "As received" samples as well as after brine and dodecane saturation at 7000 psi. (**Figure 3.3.3** and **Figure 3.3.4**). The "As received" NMR T_2 distributions show one NMR T_2 peak at T_2 times less than 1 ms representing the residual brine in the samples (**Figure 3.3.5**).

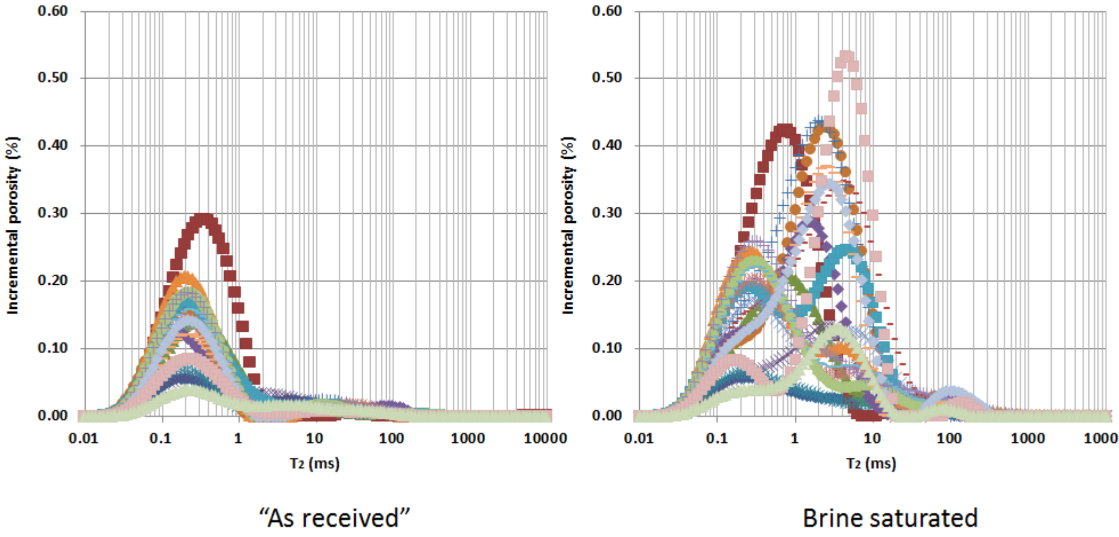

Figure 3.3.3: NMR T_2 distributions of the "As received" samples and after brine saturation at 7000 psi. There is only one NMR T_2 peak in the "As received" samples, while we generally observed two NMR T_2 peaks for the brine saturated samples.

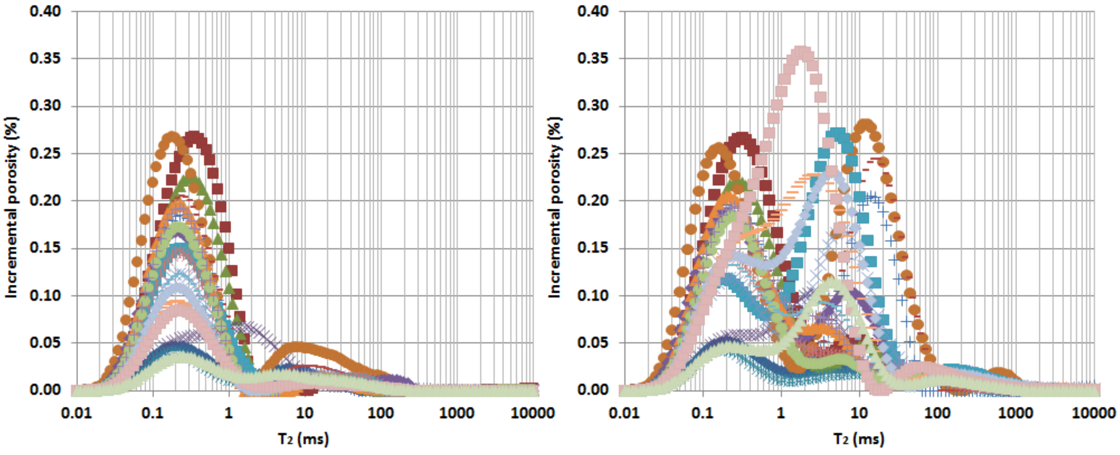

“As received” Dodecane saturated

Figure 3.3.4: NMR T_2 distributions of the “As received” samples and after dodecane saturation. While the “As received” samples have mainly one NMR T_2 peak, the dodecane saturated samples have bimodal NMR T_2 distributions.

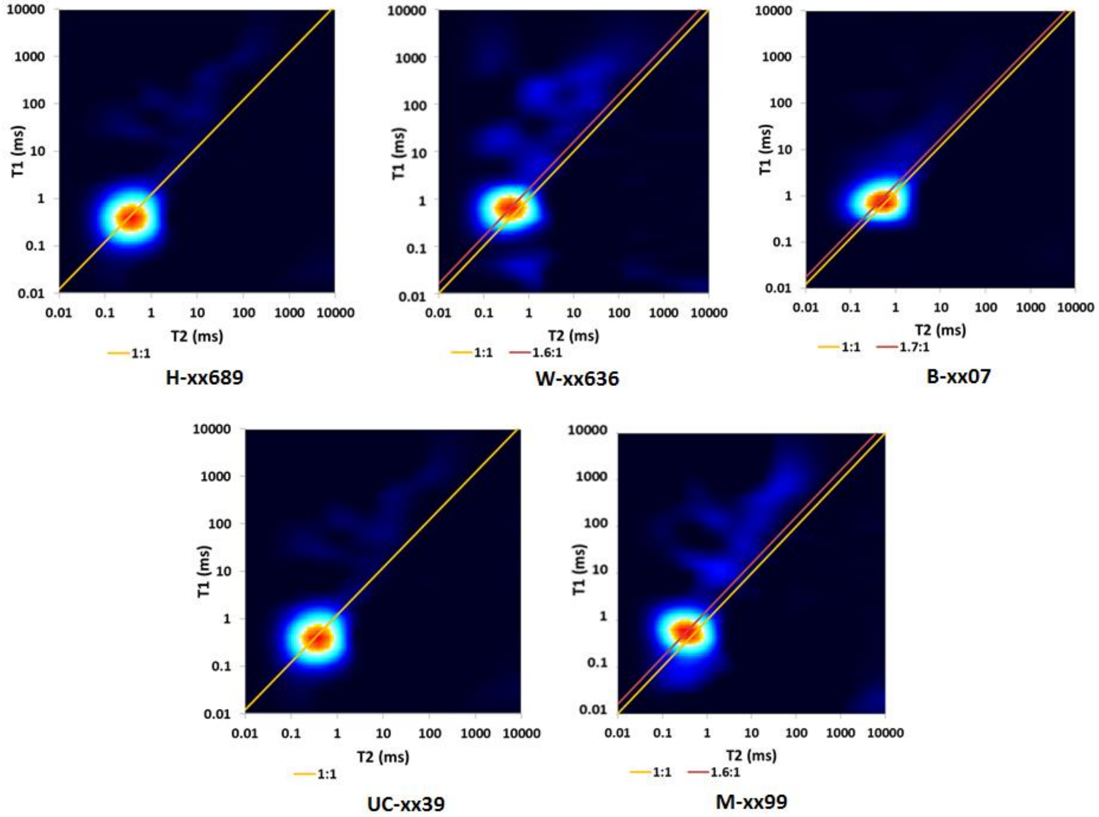

H-xx689 W-xx636 B-xx07 UC-xx39 M-xx99

Figure 3.3.5: T1-T2 maps of one “As received” sample from the Haynesville (H-xx689), Woodford (W-xx636), Barnett (B-xx07), Utica-Collingwood (UC-xx39),

and Marcellus (M-xx99) shale formation. The maps show NMR signals with T1/T2 ratio between 1 and 1.7, which represent the residual brine (Tinni et al., 2014).

However, after dodecane and brine saturation, we generally observed a bimodal distribution with a peak at T_2 times lower than 1 ms and another NMR T_2 peak between 7-20 ms. This observation can be due to a bimodal pore size distribution, the presence of pores with two different surface relaxivities or the combination of both.

We have fitted the NMR T_2 distributions with Gaussian functions (**Figure 3.3.6**) Peak 1 represent the NMR T_2 peak below 1 ms and peak 2, the NMR T_2 between 7-20 ms.

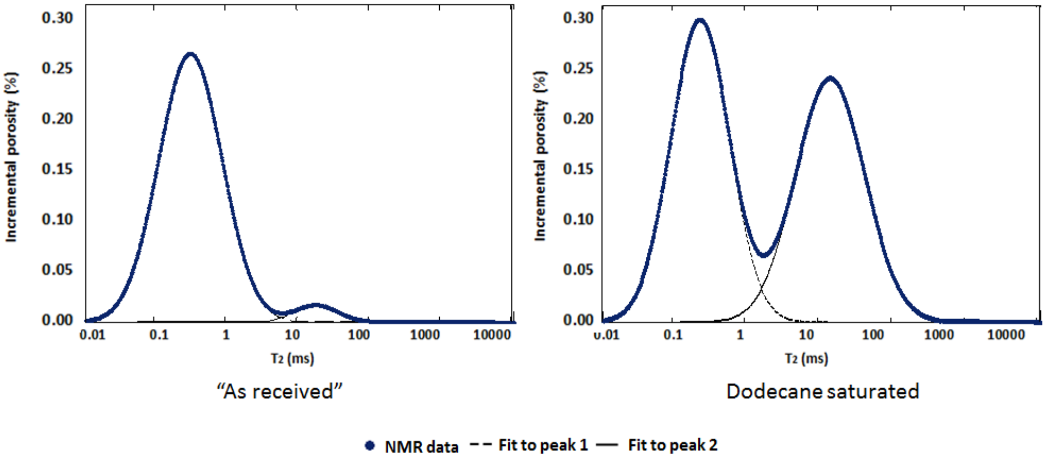

"As received"

Dodecane saturated

Figure 3.3.6: Example of Gaussian fitting applied to NMR T_2 distributions.

Figure 3.3.7 illustrates the increase of peak 1 and 2 after brine saturation as a function of clay content. **Figure 3.3.8** shows the dodecane intake in peak 1 and peak 2 as a function of TOC. We observe a positive correlation between the brine intake of peak 1 and clay content, and no relationship between the brine intake of peak 2 and clay content. In most samples the dodecane intake of peak 1 is less than 0.5 pu, and we do not observe a relationship between the dodecane intake of peak 1 and TOC. The increase of peak 2 after dodecane saturation shows a positive correlation with TOC.

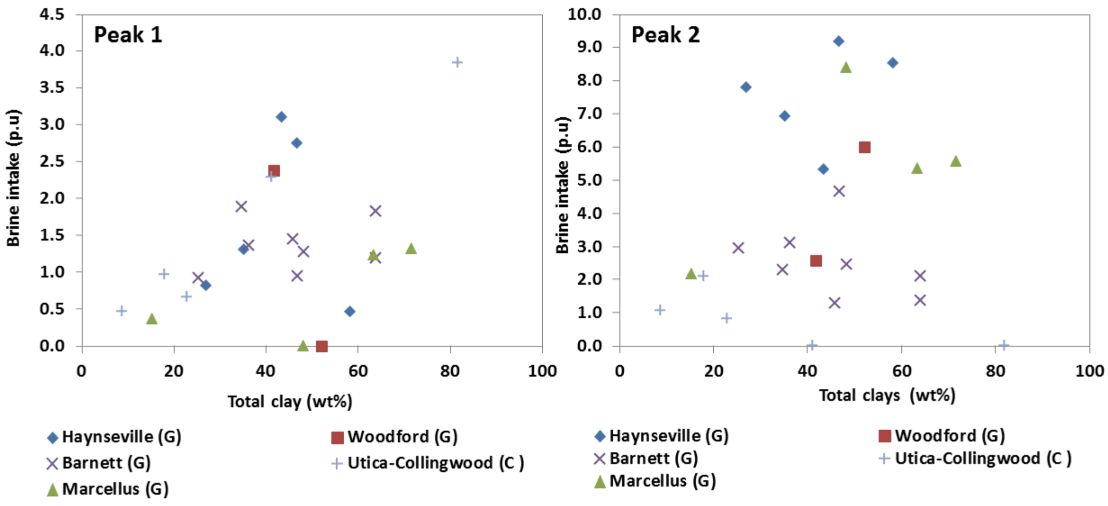

Figure 3.3.7: Brine intake of peak 1 and peak 2 after saturation at 7000 psi as a function of clay content. Note that the scales on the y axes are different. We observe a positive correlation between the increase of peak 1 and the clay content, but no relationship between the increase of peak 2 and the clay content.

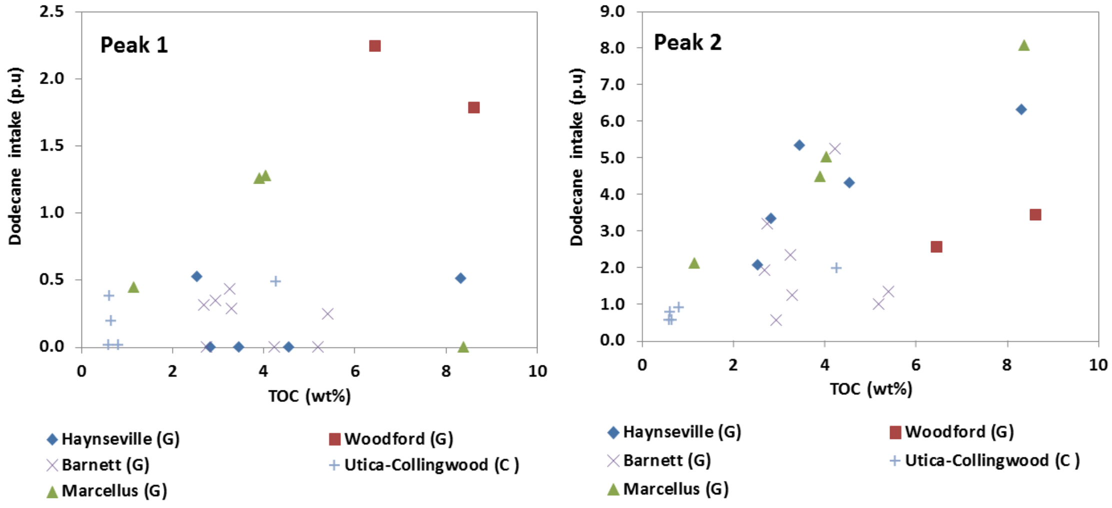

Figure 3.3.8: Dodecane intake of peak 1 and peak 2 after saturation at 7000 psi as function TOC. Note that the scales on the y axes are different. In most samples the increase of peak 1 after dodecane saturation is less or equal to 0.5 p.u, and does not exhibit a correlation with TOC. However, the increase of peak 2 after dodecane saturation shows a positive correlation with TOC.

These observations imply that pores associated with peak 1 are mainly comprised of water wet pores and the ones associated with peak 2 are essentially hydrocarbon wet pores. However, the scatter in the data indicate the presence of other types of pores such as mixed wet pores in peak 1 and peak 2.

The brine intake of peak 1 is generally larger or equal to the dodecane intake of peak 1 (**Figure 3.3.9**), and the dodecane intake of peak 2 is generally less or equal to the brine intake of peak 2 (**Figure 3.3.10**). Therefore, the pore space that is accessible only through water wet pores with diameters smaller than 4 nm are water wet pores as well as hydrocarbon and mixed pores.

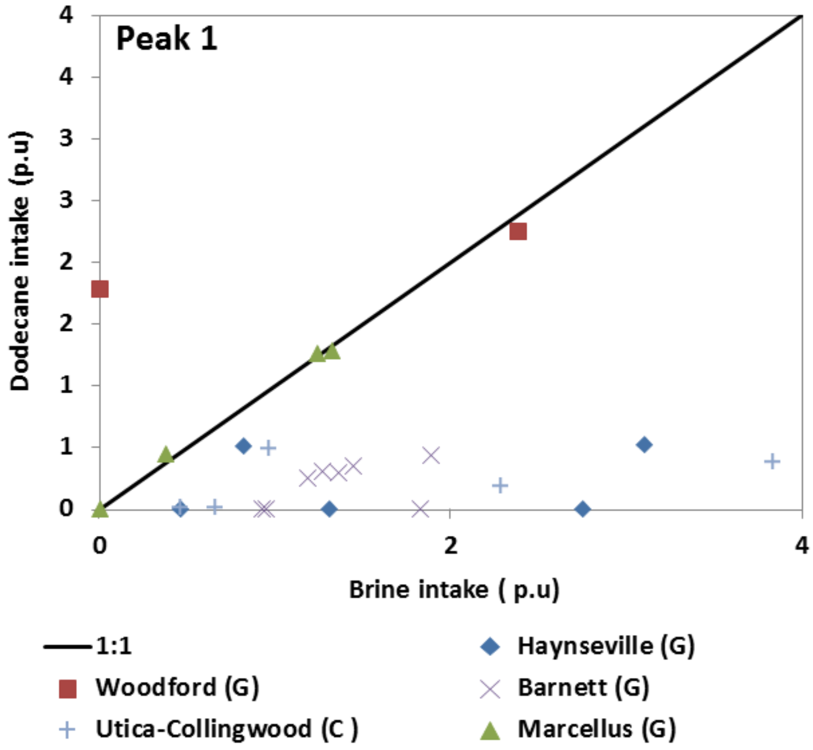

Figure 3.3.9: Comparison between the dodecane intake of peak 1 and brine intake of peak 1 after saturation at 7000 psi. The brine intake is generally larger or equal to the dodecane intake.

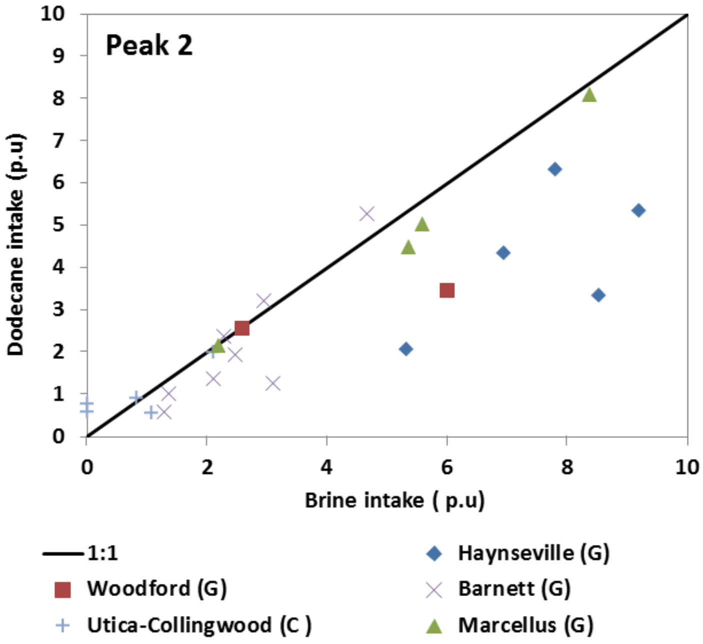

Figure 3.3.10: Comparison between the dodecane intake of peak 2, and the brine intake of peak 2 after 7000 psi saturation. The dodecane intake of peak 2 is generally less or equal to the brine intake of peak 2.

Figure 3.3.11 illustrates the different arrangements between organic matter and inorganic minerals that will define the connectivity of the water wet and hydrocarbon wet pores.

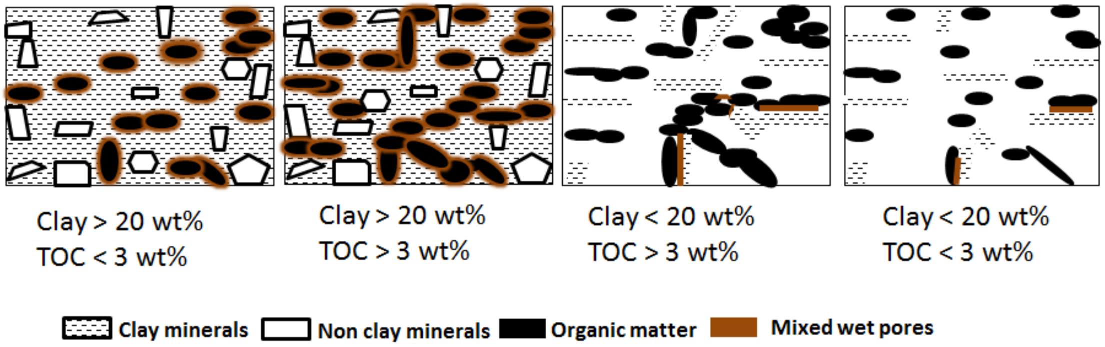
Clay > 20 wt%
TOC < 3 wt%
Clay > 20 wt%
TOC > 3 wt%
Clay < 20 wt%
TOC > 3 wt%
Clay < 20 wt%
TOC < 3 wt%
Clay minerals
Non clay minerals
Organic matter
Mixed wet pores

Figure 3.3.11: Representation of the distribution of organic matter and inorganic minerals as a function of clay content and TOC. At clay content above 20 wt%, a continuous water wet flow path is developed. At TOC above 3 wt%, most of the organic bodies are connected; however, there are some organic that are only accessible through the water wet pores.

In order to investigate the possibility of overcoming the barrier presented by the water wet pores with diameters smaller than 4 nm, we have saturated a subset of sample at 20,000 psi with dodecane (**Figure 3.3.12**). 20,000 psi of dodecane is equivalent to about 100,000 psi of mercury pressure. After saturation at 20,000 psi, the dodecane porosity increased, but is still slightly lower than the brine porosity.

From hydrocarbon storage and flow perspective, the results described in this chapter imply that hydrocarbon will be stored essentially in the hydrocarbon wet and mixed wettability pores but their deliverability will be hindered by the presence of water wet pores which will contain brine. The storage and flow of fluids as a function of pore wettability invalidates the concept of oil-water relative permeability in shales.

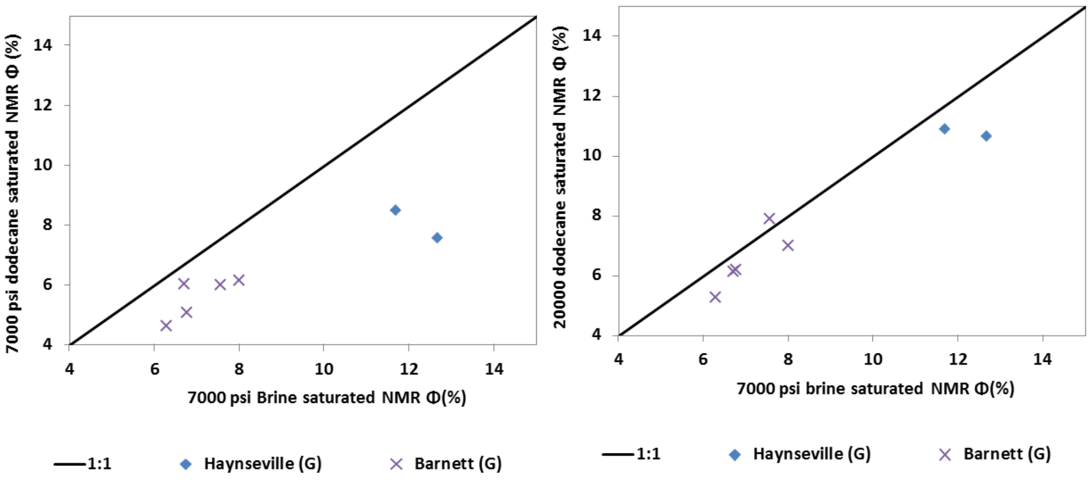

(a) (b)

Figure 3.3.12: Comparison between the porosity of a subset of samples saturated at 7000 psi with brine and dodecane (a) and at 20,000 psi with dodecane (b). The difference between the brine and dodecane porosity reduces after dodecane saturation at 20,000 psi.

Peak 2 represents the hydrocarbon wet pores as well as some mixed wettability pores. Therefore the magnitude of peak 2 after dodecane saturation can be used as proxy for the amount of producible hydrocarbon at a given pore pressure. To evaluate the productivity of hydrocarbon in more samples, we have saturated the 23 samples in **Table A-III** (cf. appendix) in addition to the 24 samples in **Table A-II** with dodecane at 7000 psi. **Figure 3.3.13** illustrates the relationship between peak 2 for this extended dataset and TOC; there are two trends. The samples in trend C show a higher magnitude of peak 2 than the samples in trend D at the similar values of TOC. This behavior can be caused by the predominance of water wet pores with diameters larger than 4 nm in the population of water wet pores and or by the presence of more mixed wettability pores in the samples of trend C. Samples from all formations can be found in trend C or D. Therefore the main difference between shale formations is ratio between the volume of facies with samples that belong to trend C or D. For a pore pressure of less than or equal to 7000 psi the facies represented by the samples in trend C will be better producers than those falling in trend D.

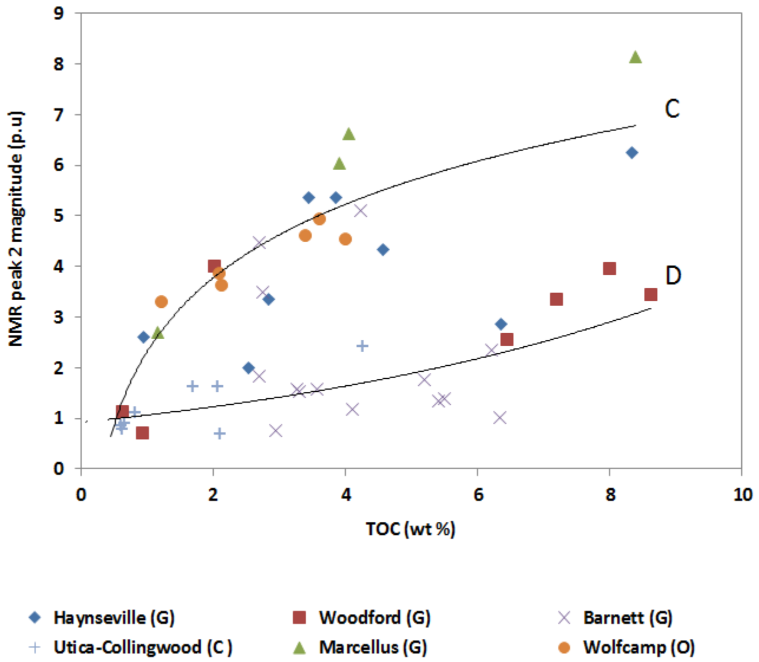

Figure 3.3.13: Magnitude of peak 2 after dodecane saturation at 7000 psi as a function of TOC. We observe two trends (C and D). The samples in trend C have a higher proportion of water wet pores with diameters larger than 4 nm and or mixed wettability pores.

4 Hydrocarbon storage in Shale

4.1 Special considerations in shales

In conventional reservoir rocks, hydrocarbons are stored as compressed fluids within the pore space. The knowledge of the available pore space and fluid properties is sufficient to predict the volumes and phases (gas and or liquid) of hydrocarbons present at a given pressure and temperature. The fluid properties are taken to be the bulk fluid properties. The prediction of hydrocarbon volumes and phases is performed with an equation of state (EOS) such as Peng-Robinson (Peng and Robinson 1976) or Soave-Redlich-Kwong (Soave 1972). However, recent papers by Didar and Akkutlu (2013), Ma et al., (2013), Pitakbunkate et al., (2015) suggested that the fluid critical properties change when the pore diameter approaches 10-15 nm. Therefore, the fluid properties used for conventional reservoir might not be appropriate for shale reservoirs.

In organic rich shales, hydrocarbons are stored as an adsorbed phase on the pore walls (generally organic pores) in addition to being stored as compressed fluids in the rest of the pore space (Ambrose et al., 2010; Bustin et al., 2008; and Sondergeld et al., 2010). The adsorbed phase storage capacity is currently quantified by the establishment of an absolute absorption isotherm (Ambrose et al., 2010).

Absolute adsorption cannot be determined directly (Sudibandriyo et al., 2003). In practice, the surplus of hydrocarbon due to adsorption (n_{excess}) is quantified by taking the difference between the total amount of hydrocarbon stored at a given pressure (n_{total}) and the amount of hydrocarbon that would be stored without adsorption (n_{free}) **(equation 4.1.1)**.

$$n_{excess} = n_{total} - n_{free} \tag{4.1.1}$$

The hydrocarbon surplus is often called Gibbs adsorption.

The storage capacity without adsorption is obtained after helium porosity measurement and adjustment for the hydrocarbon properties (Fitzgerald 2005; and Kang et al., 2010).

The absolute adsorption is obtained using **equation 4.1**.**2** (Mohammad et al., 2009), Ambrose et al., 2010; and Heller and Zoback 2014).

$$n_{absolute} = \frac{n_{excess}}{(1 - \frac{\rho_{fluid}}{\rho_{ads}})} \tag{4.1.2}$$

ρ_{fluid} is the bulk hydrocarbon density, and ρ_{ads} is the adsorbed phase density.

The application **equation 4.1**.**2** requires the knowledge of the adsorbed phase density. A literature review on the subject shows that the adsorbed phase density is not well constrained. Menon (1968) as well as Findenegg and Loring (1984) postulated that the adsorbed phase density should be equal to the liquid density. Haydel and Kobayashi (1967) concluded from their studies that the average adsorbed phase density is close the Van der Waals parameter “b”. Diaz-Campos and Hobson (2014) demonstrated with molecular dynamic simulation that the adsorbed phase density varies as a function of pressure. For a 4 nm graphene slit pore and a temperature of 46 ^{o}C Diaz-Campos and Hobson (2014) found that the absorbed phase density of methane increased from 0.06 g/cc to 0.27 g/cc when the pressure increased from 190 to 6850 psi.

When the absolute isotherm can be fitted with **equation 4.1**.**3**, the isotherm is called a Langmuir isotherm (**Figure 4.1.1**). Langmuir isotherm represents a monolayer adsorption process (Langmuir 1918).

$$n_{adsorbed} = \frac{p}{p + p_L} n_L \tag{4.1.3}$$

$n_{adsorbed}$ is the amount adsorbed at pressure p. n_L is the maximum adsorption capacity of the rock and p_L is the pressure at half n_L.

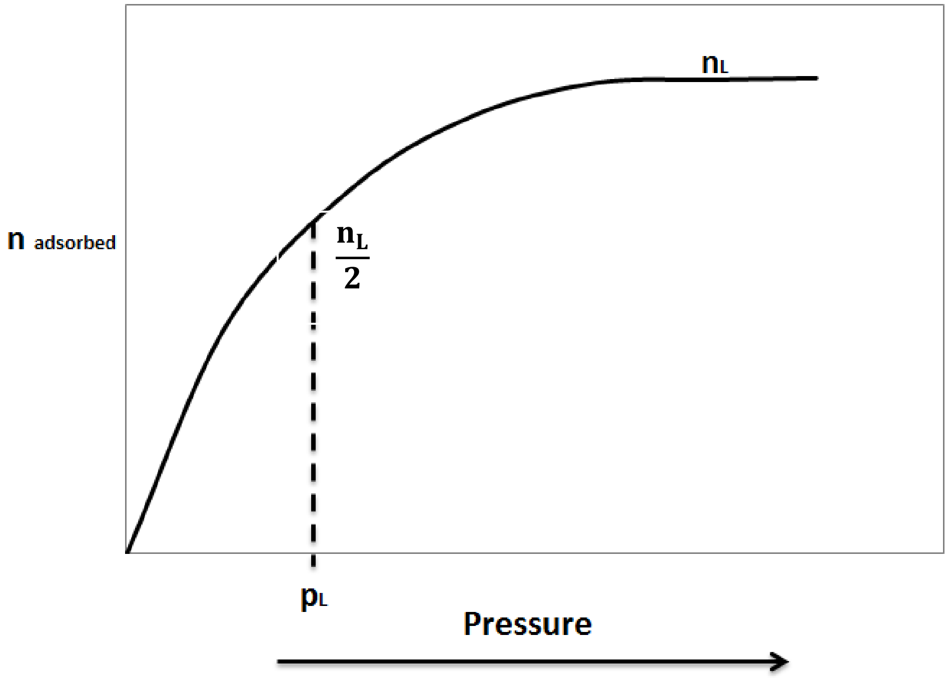

Figure 4.1.1: Schematic representation of a Langmuir isotherm.

Figure 4.1.2 (a) and **Figure 4.1.2 (b)** shows the methane excess adsorption measurements on a Sleen shale sample by Gasparik et al., (2012), and the absolute adsorption isotherms established using an adsorbed phase density of 0.42 g/cc (liquid density), 0.34 g/cc (Ambrose et al., 2010), and 0.27 g/cc (Diaz-Campos and Hobson 2014) respectively. Note that the assumed adsorbed phase density will significantly impact the reported absolute adsorption capacity, n_L, as well as the shape of the isotherm. While the isotherms established assuming 0.42 g/cc and 0.34 g/cc for the adsorbed phase density can be considered as Langmuir isotherms, the isotherm established assuming 0.27 g/cc for the adsorbed phase density cannot be considered as Langmuir isotherm.

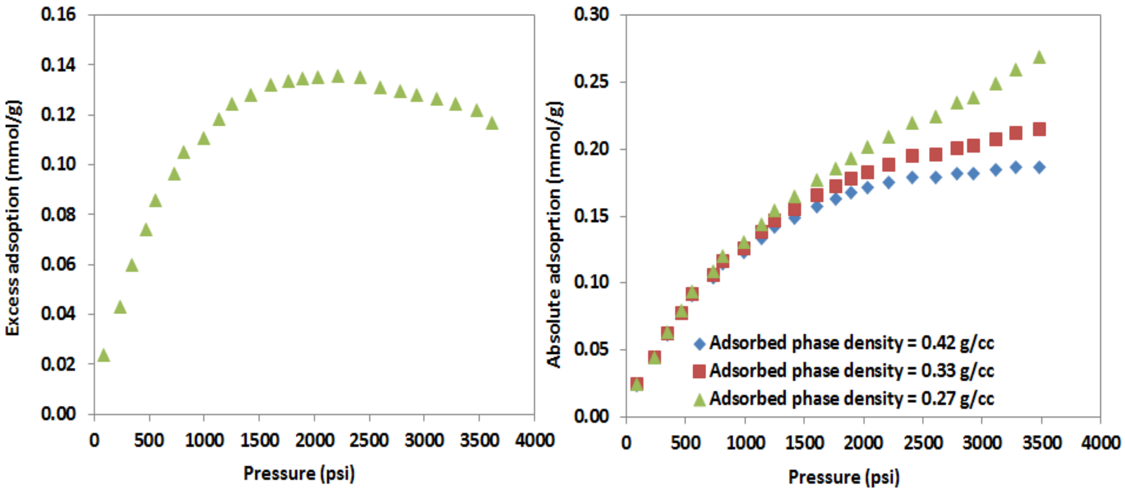

(a) (b)

Figure 4.1.2: Excess methane adsorption measurements on a Sleen shale sample by Gasparik et al., (2012) (a). (b) illustrates the absolute adsorption isotherms established from (a) using 0.42 g/cc, 0.33 g/cc, and 0.27 g/cc for the adsorbed phase density.

From the preceding it can be concluded that absolute adsorption isotherms are not accurate because of the lack of constrain on the adsorbed phase density.

The measurement of excess hydrocarbon due to adsorption requires the knowledge of the properties of the measurement fluids which are also in question.

In the following we have quantified the contribution of the pores with diameters less than or equal to 15 nm to the total porosity in several shales, conducted methane and ethane storage measurements, and multicomponent desorption experiments.

4.2 Contribution of the pores with diameters less than or equal to 15 nm to the total porosity

In order to estimate the contribution of the pores with diameters less than or equal to 15 nm (Φ_{15}) we have conducted subcritical nitrogen gas adsorption experiments on 41 samples from the Haynesville, Barnett, Wolfcamp and Avalon shale formations. The Haynesville and Barnett samples were from the dry gas window, while the Wolfcamp and Avalon sample were from late oil-condensate window. **Table A-IV** (cf. appendix) summarizes the petrophysical properties of the samples used. The pore size distributions of the samples were obtained using the DFT carbon slit model.

Figure 4.2.1 shows the comparison between the porosity calculated with the DFT slit method and the measured crushed rock helium porosity.

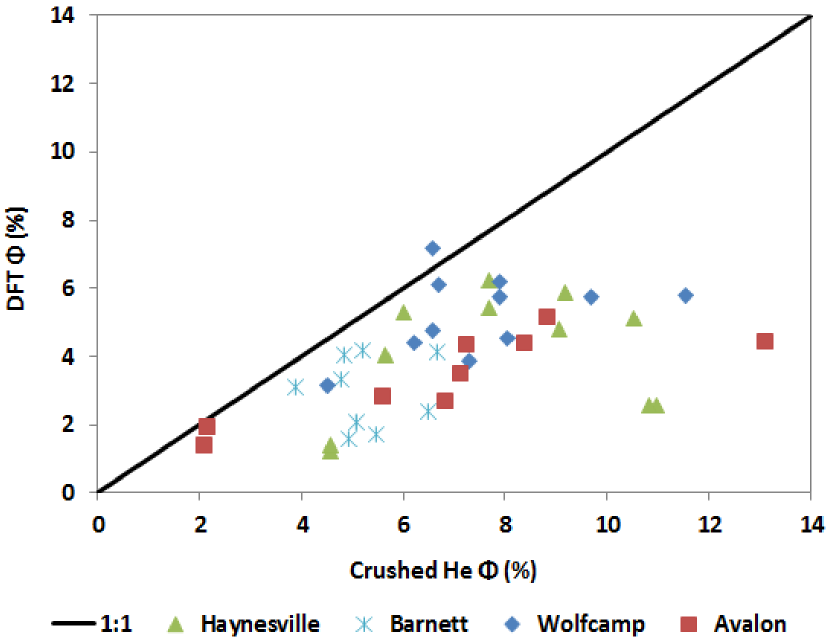

Figure 4.2.1: Comparison between the porosity calculated with the DFT carbon slit method and the measured crushed rock helium porosity. The crushed rock helium porosity is generally larger than the DFT porosity because the DFT method can only resolve pore with diameters less than or equal 300 nm.

Figure 4.2.2 illustrates the pore size distributions of the samples studied. The pore diameters resolved span from about 1.5 nm to about 300 nm. The samples from Haynesville, Wolfcamp and Avalon shale have pore size distributions skewed toward larger pore size, while the Barnett samples do not show any detectable skewness.

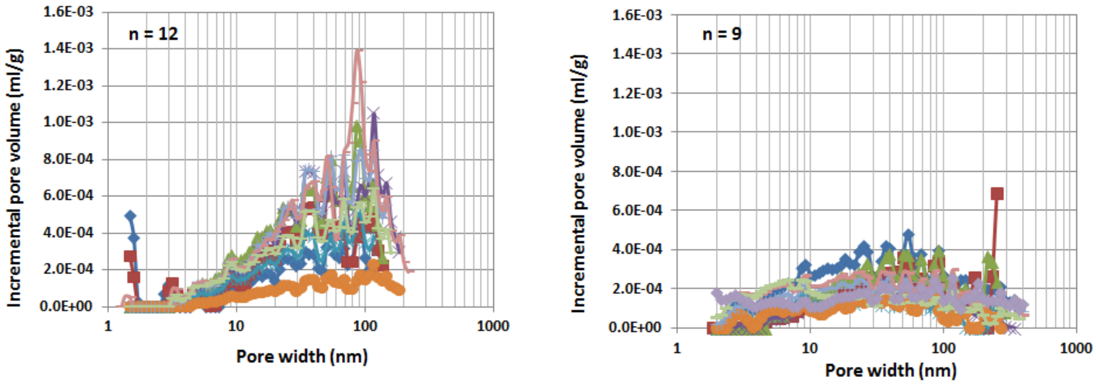

Haynesville **Barnett**

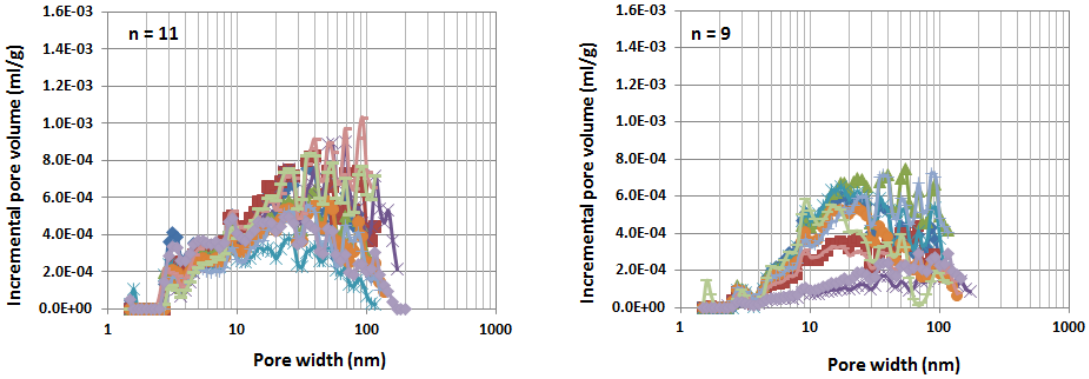

Wolfcamp **Avalon**

Figure 4.2.2: Pore size distribution obtained after subcritical nitrogen gas adsorption using the DFT carbon slit model for samples from Haynesville, Barnett, Wolfcamp and Avalon shale. The pores are assumed to have a slit shape, thus the pore size reported is the width of the slit. We consider this pore width to be representative of a pore diameter. n represent the number of samples studied for each formation.

Curtis et al., (2013) estimated the pore size distribution of a shale sample and determined the porosity associated with the pores below SEM resolution (~4nm) assuming a fractal distribution (**Figure 4.2.3**). They estimated that the porosity associated with the pores with radii smaller than 4 nm is in the order of 0.2 %. This observation implies that pore size distribution should be skewed toward lager pore sizes, which is confirmed by the pore size distributions in **Figure 4.2.3**.

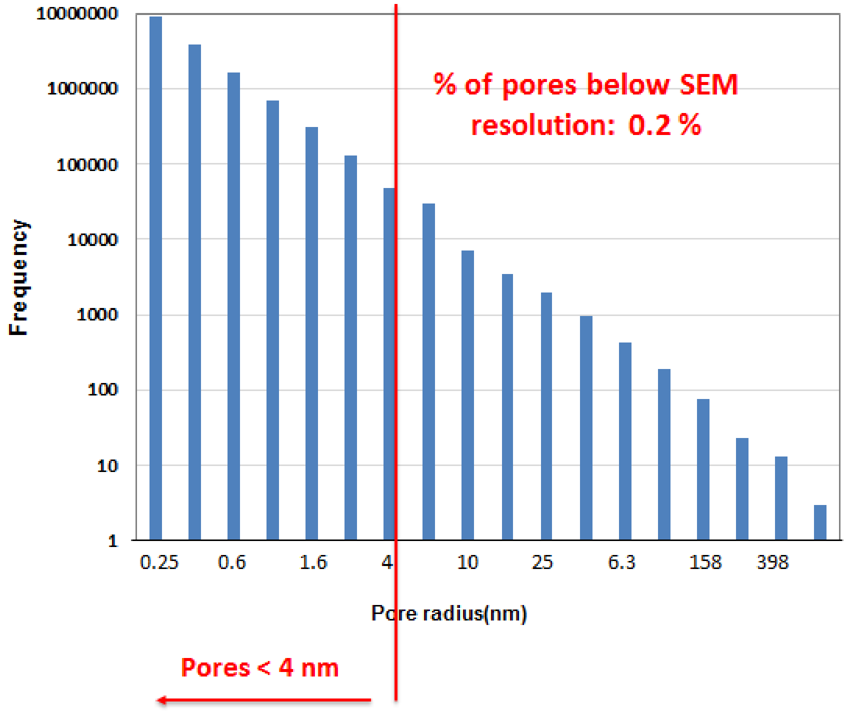

Figure 4.2.3: Pore size distribution in an Eagle Ford sample (Curtis et al., 2013). The pores with radii larger than 4 nm were quantified from the SEM images while the pores with radii less than 4 nm are estimated assuming a fractal pore size distribution.

Figure 4.2.4 presents the histograms of the contribution of Φ_{15} to the total pore volume for the different samples studied. This contribution varies from 5 % to 45 %. The Haynesville samples have the lowest contribution of Φ_{15} with an average of 10 % while the Wolfcamp samples have the largest contribution with an average of 25 %. These observations imply that the porosity associated with Φ_{15} is not dominant in most shale samples.

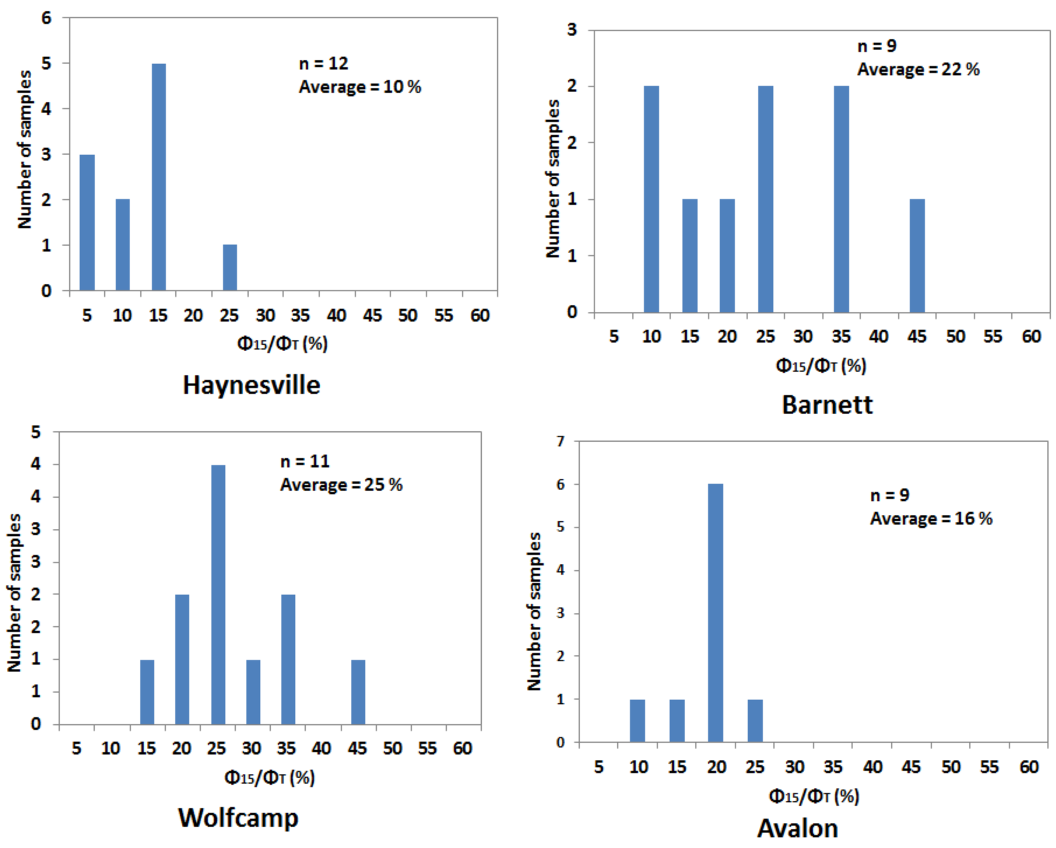

Figure 4.2.4: Histograms of the contribution of Φ_{15} to the total pore volume. The Haynesville samples have lowest contribution of Φ_{15} with an average of 10% while the Wolfcamp samples have the largest contribution with an average 25%.

Figure 4.2.5 shows the contribution of Φ_{15} plotted as function of clay content and TOC. We do not observe a relationship between the contribution of Φ_{15} with either clay content or TOC, implying that these pores are distributed between the clays and the organic pores.

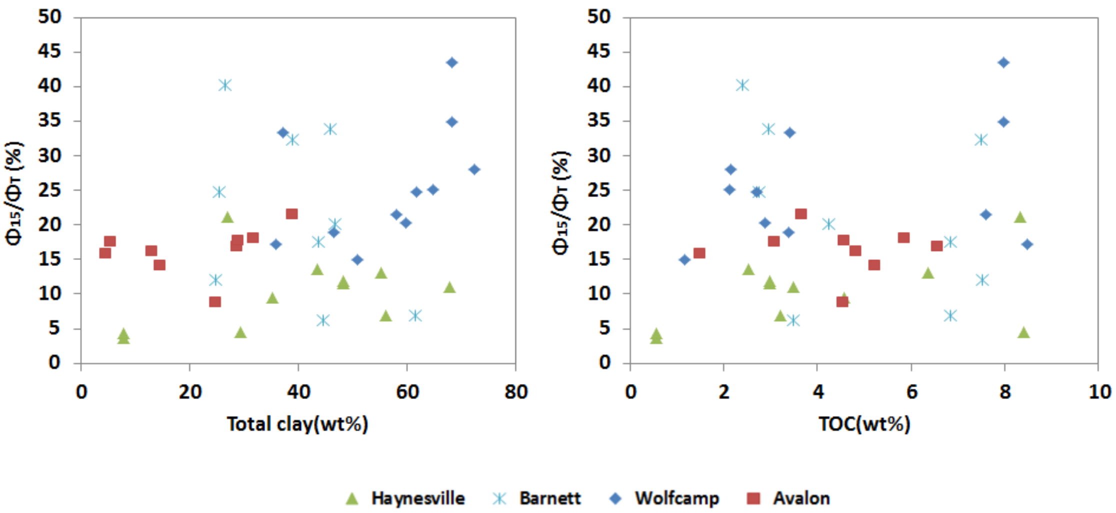

Figure 4.2.5: Contribution of Φ_{15} as a function of clay content and TOC. We do not observe a relationship between the contribution of Φ_{15} with either clay content or TOC.

4.3 Hydrocarbon storage measurements

4.3.1 Experimental procedure and samples description

The current industry practice for storage measurements in shales is designed for crushed rocks with the assumptions that the critical properties of the measurement fluid are not affected by the pore size. Measurements on crushed rock cannot be conducted under confining pressures. Therefore these measurements might not be representative of reservoir condition. In order to obtain measurements representative of reservoir conditions, we have conducted our storage measurements on “As received” Tennessee sandstone, Barnett, and Eagle Ford core plugs with lengths approximately equal to 1.5 in and diameters equal to 1 in **Table 4.3.1** summarizes the petrophysical properties of the samples used.

The Tennessee sandstone sample is a low porosity sandstone that was used as control sample.

Table 4.3.1: Petrophysical properties of the samples used for hydrocarbon storage measurements. The letters in the sample ID refers to the shale formation. B is used for Barnett and EF is used for Eagle Ford.

Sample ID	Crushed helium Φ(%)	Quartz + Feldspars (wt%)	Total clays (wt%)	Total carbonates (wt%)	TOC (wt%)	Specific surface area (m^2/g)
Tennessee sandstone	6.1	96	8	2	NA	0.5
B-xx97	5.2	38	39	13	7.5	11.2
EF-xx72	5.3	8	6	81	1.3	3.6
EF-xx18	5.1	10	9	74	1.3	3.3

Subcritical nitrogen gas adsorption measurements were conducted with approximately 1 g of the samples. The smallest pore diameter resolved in the Tennessee and Eagle Ford samples is 5 nm and 2 nm for the Barnett sample (**Figure 4.3.1). Figure 4.3.1** shows that the pore size distributions (4 samples) of the Tennessee and Eagle Ford samples are skewed toward the larger pores while the Barnett sample does not show a particular skewness. The contribution of Φ_{15} for the Tennessee sandstone is 0.6%, 32 % for the Barnett sample, 0.7 % for EF-xx18, and 1 % for EF-xx72.

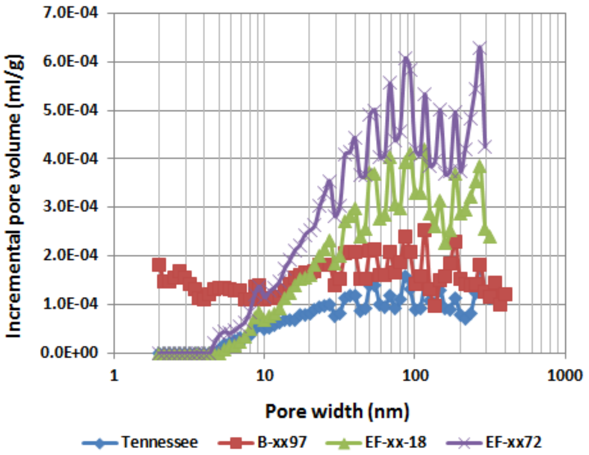

Figure 4.3.1: Pore size distributions of the samples used for storage measurements.

To verify, if fluid properties are affected by the pore structure, we chose to conduct our storage measurements with NMR.

The experiment consisted in measuring the NMR T_2 distributions of core plugs saturated with methane and ethane with a 2 MHz Oxford Geospec2™ NMR instrument at a TE = 200 µsec. **Figure 4.3.2** shows a schematic of the experimental setup.

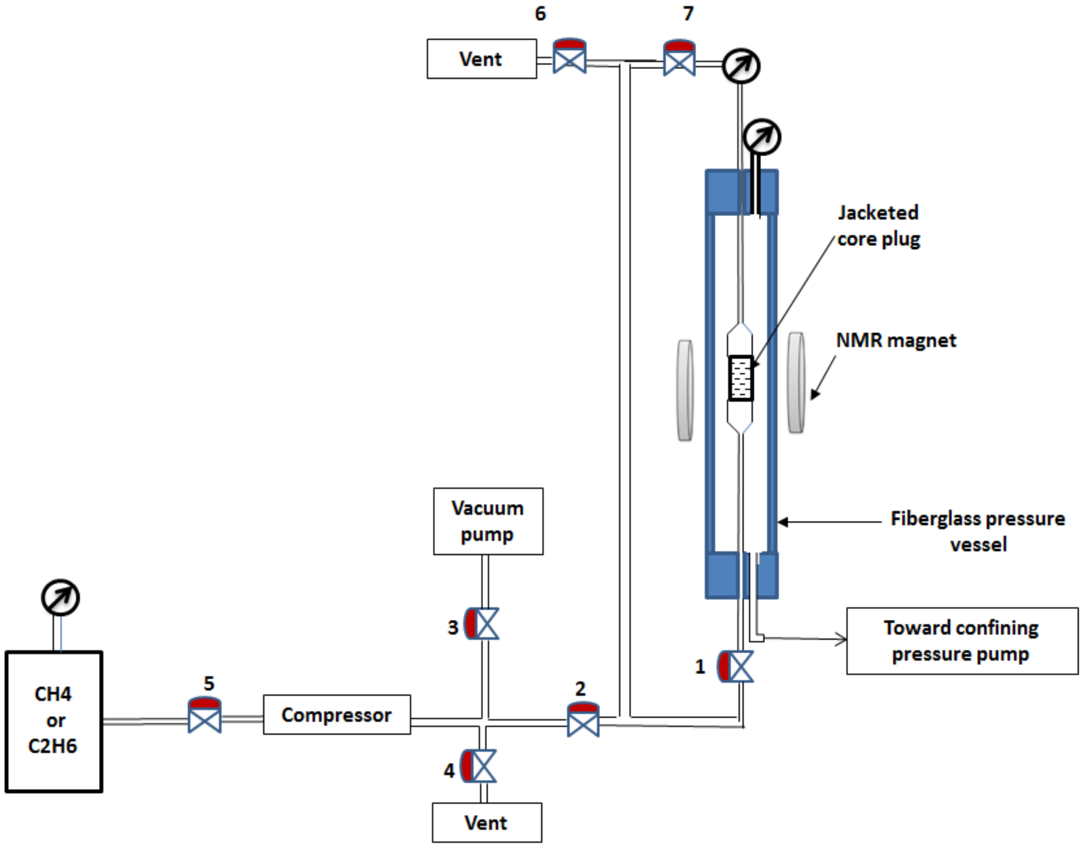
6
7
Vent
Jacketed core plug
NMR magnet
Fiberglass pressure vessel
Vacuum pump
3
Toward confining pressure pump
1
CH4 or C2H6
5
Compressor
2
4
Vent

Figure 4.3.2: Schematic of the experimental setup used for hydrocarbon storage measurements. Fluorinert FC 770 was used as confining pressure fluid.

Prior the saturation with methane or ethane the core plug is jacketed in a Teflon sleeve and the confining pressure is increase to 5000 psi. Valve 1, 2, 3 and 7 are opened while valve 4, 5 and 6 are closed to allow the application of vacuum for 1 hour. To saturate the sample, valve 3 is closed and 5 is open to allow the flow of the measurement fluid into the compressor. The compressor is used to pressurize the measurement fluid up to the desire pressure. The compressor is equipped with a check valve that prevents flow back toward the methane or ethane tanks. After the desire pressure is reached, valve 1 and 7 are closed and the pore pressure is monitored with a digital pressure gauge with a resolution of ± 1psi. The sample is considered fully saturated if the pressure does not decrease by 5 psi over 8 hours. If the pressure drops by more than 5 psi over a time interval less or equal to 8 hours, the sample is resaturated. Approximately 8 to 16 hours were required to saturate the samples with methane, while the saturation with ethane required 16 to 48 hours.

During the experiments, confining pressure was kept constant at 5000 psi and the NMR data was acquired at pore pressures between 300 and 4000 psi. The temperature was kept constant at 30 ^{o}C.

At these pressures and temperature conditions methane does not go through a phase transition. It is a gas at pressure lower than 670 psi and a supercritical fluid at pressure greater than 670 psi. We have used methane to study the storage mechanism in the dry gas window. At 30 ^{o}C ethane changes phases from gas to liquid at 675 psi; thus ethane can be used to study the storage mechanisms in liquid rich shales as well as changes in critical properties if they occur.

4.3.2 Methane and ethane storage measurements

The NMR T_2 distributions of the samples saturated with methane and ethane (**Figure 4.3.3**) show 2 NMR T_2 peaks for Tennessee sandstone and 3 peaks for the shale samples. All samples show an NMR T_2 peak at T_2 times larger than 200 ms. This peak represents the NMR signal associated with methane or ethane in the tubing above and below the sample. Therefore the NMR amplitudes above 200 ms were not included in our calculations and analysis.

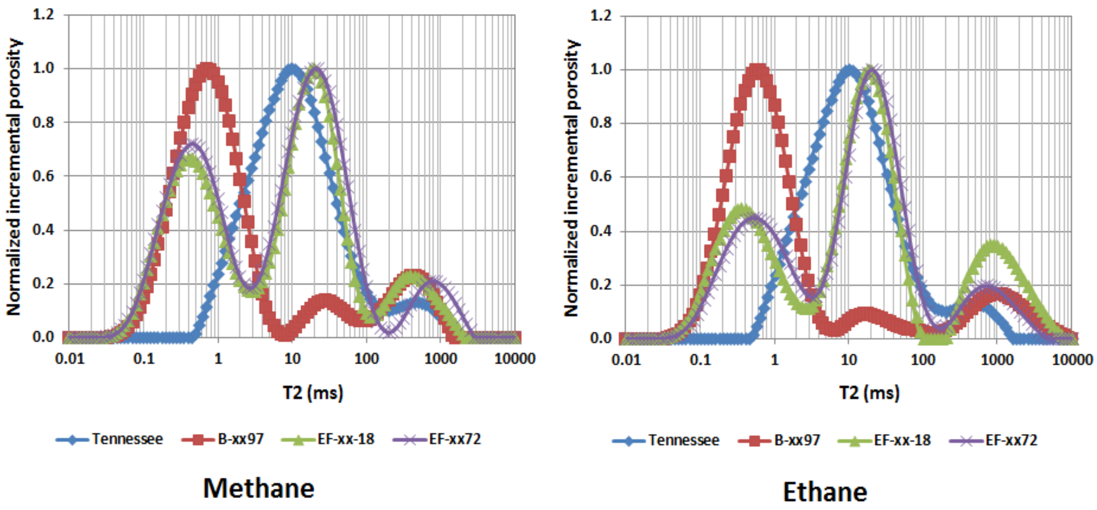

Methane

Ethane

Figure 4.3.3: NMR T_2 distribution of the Tennessee sandstone, Barnett, and Eagle Ford samples saturated with methane and ethane. The T_2 data was normalized to the maximum amplitude observed in each sample. The NMR signal at T_2 times larger than 200 ms represents methane or ethane in the tubings above and below the sample.

In order to evaluate the storage of methane and ethane we have converted the NMR amplitudes to porosity using **equation 2.5.2**. The hydrogen index used in **equation 2.5.2** was computed with **equation 2.5.3**, assuming that the fluid properties were not altered by the rock sample. If this assumption is correct, the calculated NMR porosity will be constant regardless of the measurements fluid or the pore pressure. An increase in porosity will translate into an increase in fluid density compared to the bulk fluid density. A decrease in porosity can be due to decrease in fluid density in comparison to the bulk fluid density or to pore compressibility if the effective pressure increases.

The NMR measurement at every pressure was repeated 3 times in order to assess the repeatability of the measurements and obtain an estimate of experimental errors. The measurements were conducted while the pore pressure was sequentially increased up to a pressure of 4000 psi then decreased sequentially. In order to evaluate the hysteresis between the data acquired when the pore pressure was increasing and decreasing we have introduced the term Ψ defined by **equation 4.3.1**.

$$\Psi = \frac{\phi_{up} - \Phi_{down}}{2 * \varepsilon} \qquad 4.3.1$$

ϕ_{up} is the calculated NMR porosity while the pressure is increasing and Φ_{down} is the calculated NMR porosity while the pressure is decreasing. ε represents the experimental error estimated from the standard deviation of the 3 measurements acquired at a given pore pressure. When Ψ is lower than 1, there is no hysteresis and when Ψ is larger than 1 there is measurable hysteresis.

Figure 4.3.4 to **Figure 4.3.7** show the NMR porosity and Ψ for the samples studied, using ethane and methane at different pressures. The NMR porosity presented, is the average of 3 measurements. Error bars were included in the NMR porosity measurements. However, in most case, they are too small to be seen.

Tennessee sandstone data (**Figure 4.3.4**) allows us to study hydrocarbon storage in a low porosity rock with no organic matter and a negligible contribution of Φ_{15}, thus no change in fluid critical properties due to pore confinement are expected. For this sample, the ethane saturated porosity is constant between 2000 psi and 4000 psi and close to the crushed helium porosity. This indicates that the assumed hydrogen index is correct over that pressure interval. Between 2000 psi and 750 psi the porosity decreases. This porosity reduction occurs as the effective pressure increases; thus the reduction in porosity between 2000 psi and 750 psi is due to pore compressibility.

The next pressure point below 750 psi is 650 psi. Between 750 psi and 650 psi, ethane will normally change phase, from liquid to gas at 675 psi. From 650 psi to 500 psi, the porosity increases from 6.2% to 8.9 %. This observation indicates that the assumed hydrogen index is not valid in this pressure range and the density of ethane is larger than in the bulk fluid at these pressures. This pressure range is also where we observe hysteresis in the ethane measurements. The increase in ethane density and the hysteresis occur only below the normal vapor pressure of ethane. Therefore, these phenomena are due to capillary condensation below the vapor pressure. Using the Kelvin equation (Thomson 1871) we estimated the largest pore diameter required to observe capillary condensation of ethane below its vapor pressure to be approximately 400 nm. The pore size distribution of Tennessee sandstone shows that it contains a non-negligible volume of pores with diameter less than or equal to 400 nm.

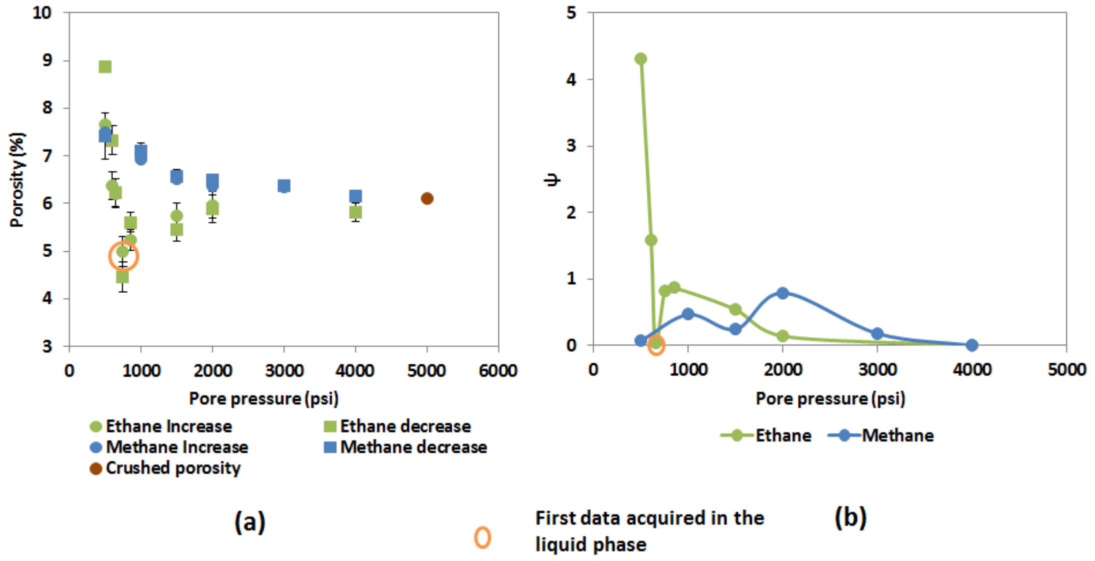

Figure 4.3.4: Ethane and methane porosity as a function of pressure (a) and ψ as a function of pressure (b) for Tennessee sandstone. At high pressures, ethane, methane and crushed helium porosity have similar values, but at low pressures we observe a porosity increase. ψ is always lower than 1 for methane, but for ethane it takes on values larger than 1 at pressures below the vapor pressure.

The methane saturated porosity at 4000 psi is similar to the ethane porosity at the same pressure as well as to the crushed helium porosity. However, when the pressure decreases, the methane porosity increases. The porosity increased from 6.1% to 7.4%

between 4000 psi and 500 psi of methane pressure. This observation indicates that the methane contained in the sample is denser than in its bulk state. No hysteresis can be observed in the methane data. The lack of a significant contribution of Φ_{15} to the total pore volume as well as the ethane measurements show that there are no changes in fluid critical properties for this sample. Therefore, the increase in porosity observed is due to the presence of an adsorbed phase with higher density than the bulk density. The increase in porosity when methane pressure decreases is due to the larger contrast in bulk density and adsorbed phase density at low pressures (Mohammad et al., 2009; and Diaz-Campos and Hobson 2014).

In the case of the Barnett sample (**Figure 4.3.5**), the ethane saturated porosity is constant and close to the crushed helium porosity from 4000 psi to 750 psi. In this pressure interval no hysteresis is observe in the data. Hysteresis and increase in porosity are only observed below the normal vapor pressure; hence they are due to capillary condensation, and not because of changes in the critical properties of ethane. From 750 to 300 psi, the porosity increased from 5.3% to 43%, implying that this sample can store up to 8 times the amount of ethane it would have stored in absence of capillary condensation. Hydrocarbon capillary condensation has been observed in shales by Chen et al., (2013).

The methane porosity at 4000 psi is similar to the ethane porosity at 4000 psi and the crushed helium porosity.

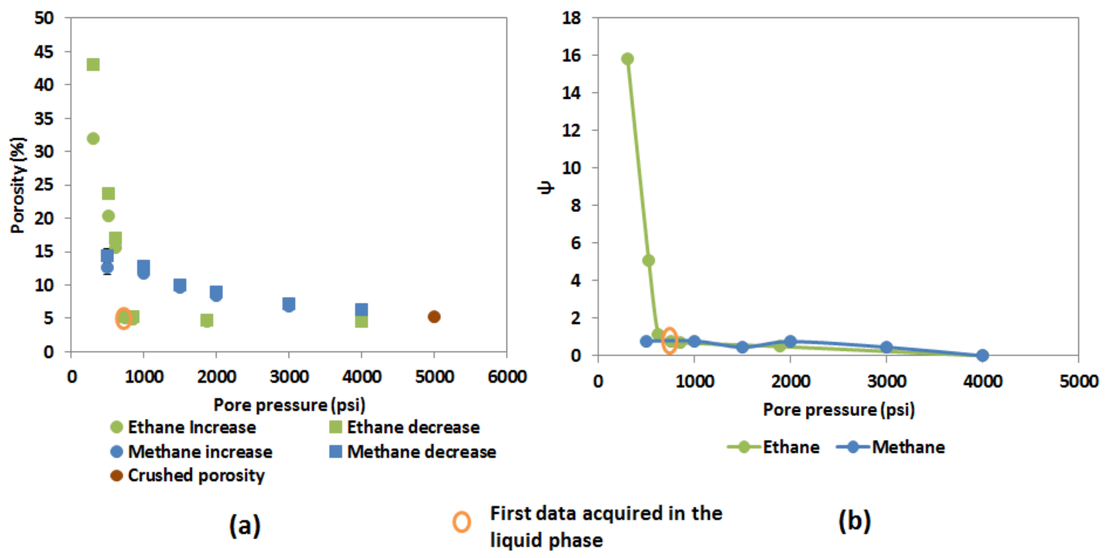

Figure 4.3.5: Ethane and methane porosity as a function of pressure (a) and ψ as a function of pressure (b) for Barnett sample B-xx97. Methane storage capacity increases as the pressure decreases because of the presence of the adsorbed phase which has a larger contrast with the bulk phase density at low pressures. No hysteresis is observed in the methane data. The ethane measurements show hysteresis below the vapor pressure because of capillary condensation. Capillary condensation also induces an increase in the storage capacity of ethane at pressures below the vapor pressure.

However, when the pressure decreases the methane porosity appears to increase due to adsorption. Between 4000 psi and 500 the methane porosity increases from 6.2% to 14.4%, implying that at 500 psi the Barnett sample can store more than two times the amount of methane it would have stored without adsorption.

Eagle Ford sample EF-xx72 (**Figure 4.3.6**) shows a similar trend as the Barnett samples, but the magnitude of increase in storage capacity for methane and ethane due to adsorption and capillary condensation are lower than in the case of the Barnett sample B-xx97.

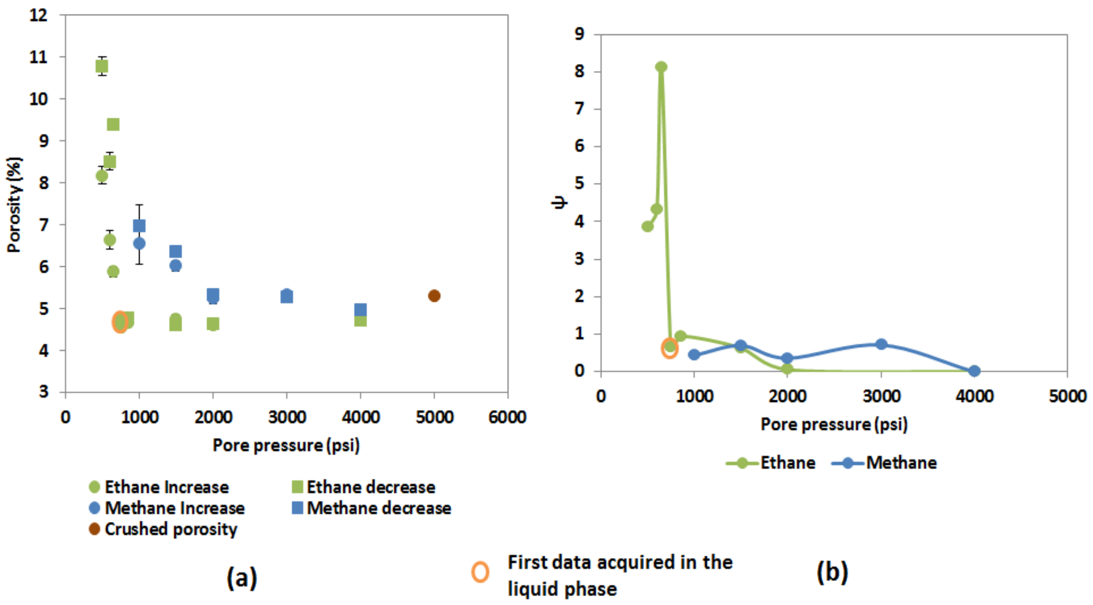

Figure 4.3.6: Ethane and methane porosity as a function of pressure (a) and ψ as a function of pressure (b) for Eagle Ford sample EF-xx72. At 4000 psi, the porosity measured with ethane, methane and the crushed helium porosity have similar values. Methane storage capacity increases at lower pressure because of adsorption, and ethane storage capacity increases below the vapor pressure because of capillary condensation which also induces hysteresis in the ethane measurements.

Eagle Ford sample EF-xx18 has the same petrophysical properties as sample EFxx72. At high pressure both sample exhibit the same behavior (**Figure 4.3.7**) and do not show changes in critical properties. However, sample EF-xx18 shows a slight decrease in ethane porosity between 2000 psi and 750 psi. This reduction in porosity due to pore compressibility is the reason why the magnitude of increase in ethane porosity is smaller for sample EF-xx18 compare to EF-xx72. Sample EF-xx72 does not show a significant increase in methane porosity as at low pressure because the increase in porosity due to adsorption is balanced by the reduction in porosity due to pore compressibility.

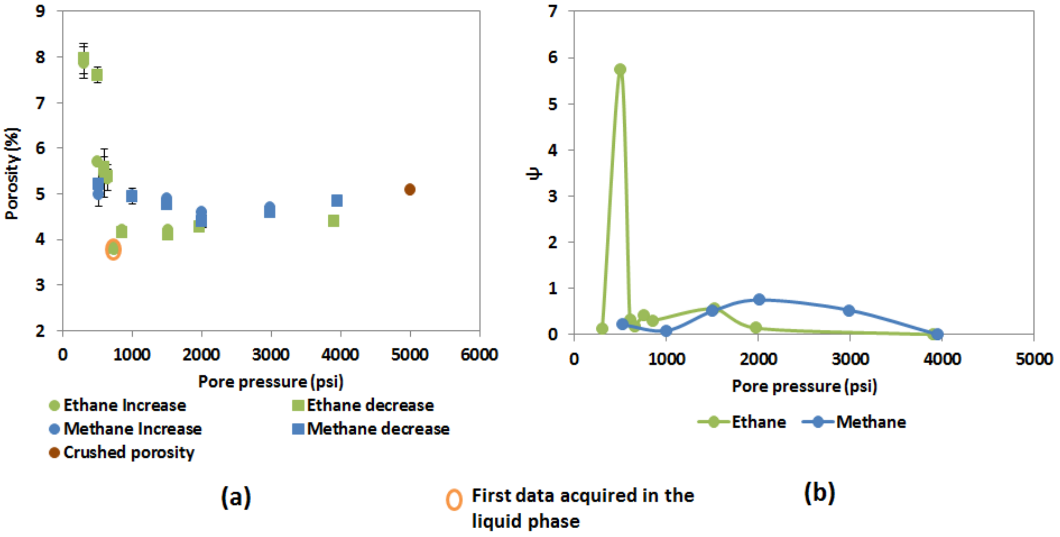

Figure 4.3.7: Ethane and methane porosity as a function of pressure (a) and ψ as a function of pressure (b) for Eagle Ford sample EF-xx18. This sample shows a reduction in ethane porosity due to pore compressibility at pressures between 2000 psi and 750 psi. This reduction in porosity balances the increase in ethane and methane storage capacity at low pressures.

4.4 Multicomponent desorption experiments

4.4.1 Experimental procedure and samples description

In the previous section, we have studied the storage of single hydrocarbon component, and observed that adsorption and capillary condensation are the dominant storage mechanisms at low pressures. In order to understand the mechanism associated with the production of multicomponent hydrocarbon mixture, we have conducted several desorption experiments on Berea sandstone, and Eagle Ford shale sample EF-xxx82, in addition to Barnett sample B-xx97 and Eagle Ford sample EF-xx72 already used for the storage measurements. The Berea sample is clean sandstone with 18% porosity; it was our control sample. The Eagle Ford shale sample EF-xxx82 has a quartz content of 4.5 wt%, 71 wt% carbonates, 20 wt% clays, 6.5 wt% TOC, and a crushed helium porosity of 6.2%.

Prior to measurements, the samples were dried at 100 ^{o}C for 48 hours. The measurements were conducted at 30 ^{o}C with a mixture of 85% methane and 15% butane. **Figure 4.4.1** illustrates the phase diagram of the mixture.

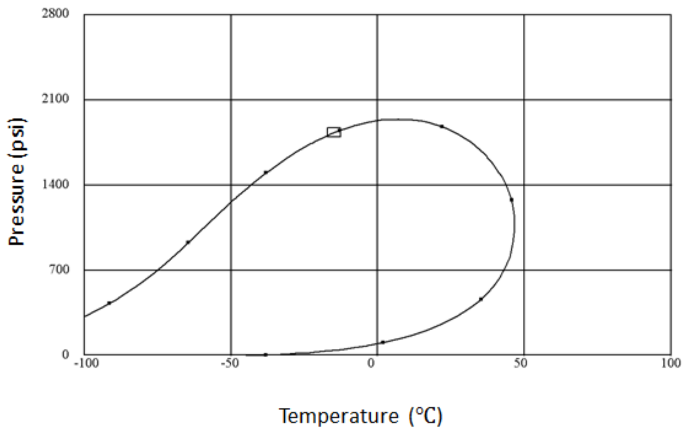

Figure 4.4.1: Phase diagram of 85% CH_4 and 15% C_4H_{10}. At 30 ^{o}C, the mixture is in gaseous phase above 1850 psi, two phases (gas-liquid) between 1850 psi and 375 psi, and single phase gas below 375 psi.

The experimental setup in **Figure 4.4.2** was used to conduct the desorption measurements.

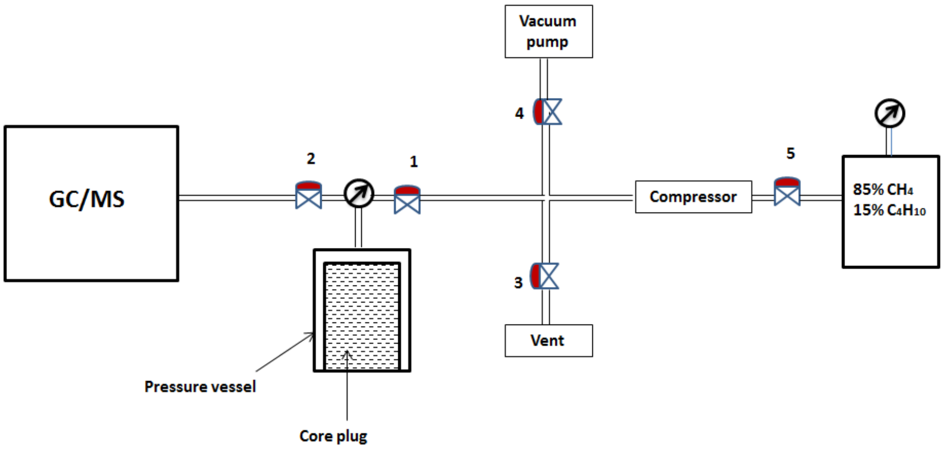
Vacuum pump
4
GC/MS
2
1
Compressor
5
85% CH4
15% C4H10
3
Vent
Pressure vessel
Core plug

Figure 4.4.2: Experimental setup used for multicomponent desorption experiments. GC/MS is the abbreviation of gas chromatograph/mass spectrometer (Agilent 7890B).

At the beginning of the experiment, the core plug and the tubing are vacuumed for 1 hour, by opening valve 1 and 4 while valve 2, 3 and 5 are closed. The vacuum step is followed by the pressurization of the sample with 85% CH_4 - 15% C_4H_{10} by closing valve 4 and opening valve 5. The opening of valve 5 allows the mixture to flow into the compressor where it is pressurize up to 3400 psi. The sample is kept at 3400 psi of fluid pressure for 10 minutes, then valve 1 is closed and the pressure within the pressure vessel is monitored with a digital pressure gauge. When the pressure reading is stable over 2 hours, we considered that equilibrium has been reached. After equilibrium has been reach, valve 2 is open for approximately 6 seconds to allow the mixture to flow into the Gas chromatograph/Mass spectrometer system. The opening of valve 2 creates a pressure drop. When the pressure reading is stable over 2 hours after the pressure drop, we open valve 2 again for 3 seconds to collect a new mixture sample.

Once inside the Gas chromatograph column, methane and butane are separated. Methane arrives first to the FID detector of the gas chromatograph and to the mass spectrometer. The mass spectrometer is used to confirm the identity of the hydrocarbon (methane or butane) and the FID detector is used to measure the amount of methane and butane that were released by the opening of valve 2.

4.4.2 Results

Figure 4.4.3 shows the signals detected by the FID detector at 3400 psi, when no sample was introduced in the pressure vessel. The FID signal is proportional to the mass of hydrocarbon detected; thus the ratio of methane signal to butane signal ($R_{CH4/C4H10}$) of 85% CH_4 - 15% C_4H_{10} mixture should be equal to 1.56.

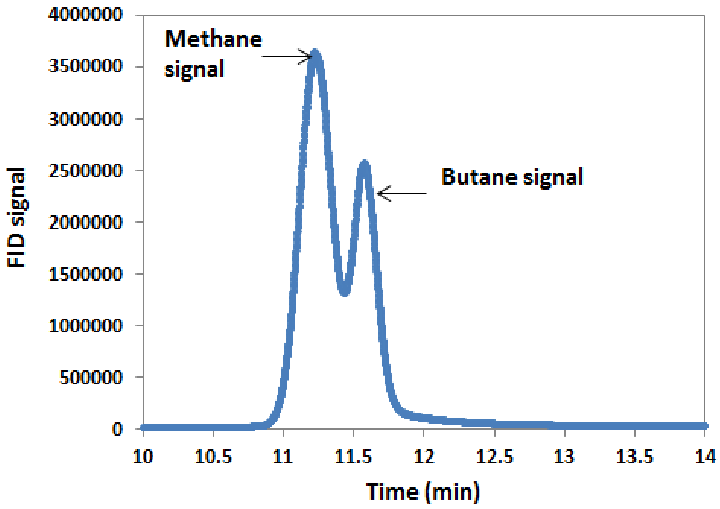

Figure 4.4.3: FID signal recorded during the analysis of the mixture collected at 3400 psi from an empty pressure vessel. The FID signal is proportional to the mass of hydrocarbon.

Figure 4.4.4 shows $R_{CH4/C4H10}$ acquired as a function of pressure when no sample was introduced in the pressure vessel. This data set gives the background response of the dead volume.

We observe that $R_{CH4/C4H10}$ is equal to the theoretical value of 1.56 until the pressure reaches the dew point of the mixture. When the pressure reaches the dew point we observe an increase of $R_{CH4/C4H10}$, implying that the mixture left in the pressure vessel contains more than 15% butane. The mixture in the pressure vessel is enriched in butane because at the dew point a fraction of the butane rich liquid phase drops at the bottom of the pressure vessel. Below 1000 psi $R_{CH4/C4H10}$ decreases because of the increase of the liquid phase saturation which will increase the mobility of this liquid phase. The dataset acquired when the pressure vessel was emptied shows that above its dew point, the mixture is produced uniformly. However, below the dew point, the generation of a liquid phase changes the composition of the stream produced. Because of the strong influence of the dead volume below the dew point, we only acquired data above the dew point of the 85% CH_4 - 15% C_4H_{10} mixture (1850 psi) when the core plugs were introduced in the pressure vessel.

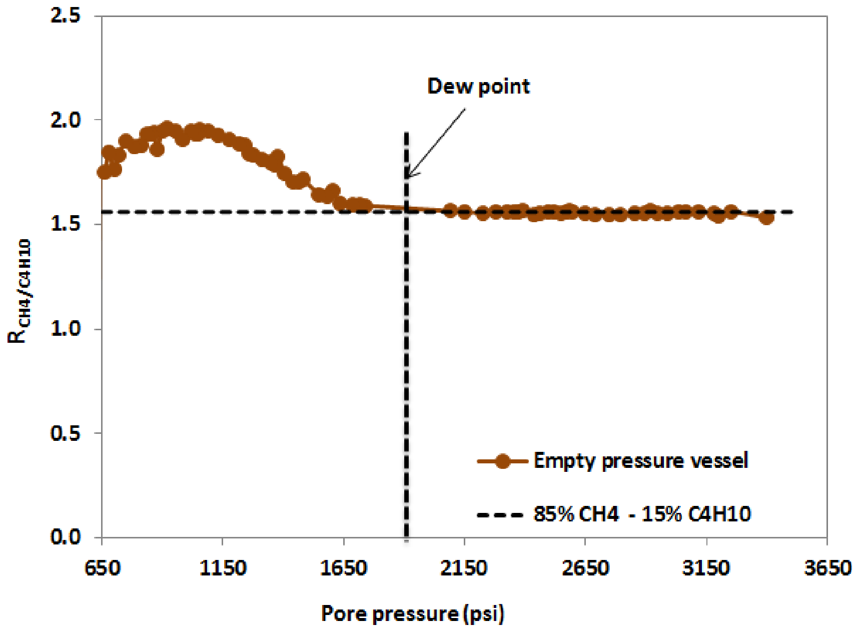

Figure 4.4.4: $R_{CH4/C4H10}$ as a function of pressure for the empty pressure vessel. The horizontal dashed line indicates the theoretical value of $R_{CH4/C4H10}$ (1.56) for a mixture of 85% CH_4 - 15% C_4H_{10}. The increase of $R_{CH4/C4H10}$ below the dew point is due to the settling of butane enriched liquid at the bottom of the pressure vessel.

Figure 4.4.5 shows the $R_{CH4/C4H10}$ data for the Berea sandstone experiment. For this sample $R_{CH4/C4H10}$ is constant and approximately equal to 1.56, implying that the production in Berea sandstone can be understood by studying bulk fluid phase behavior.

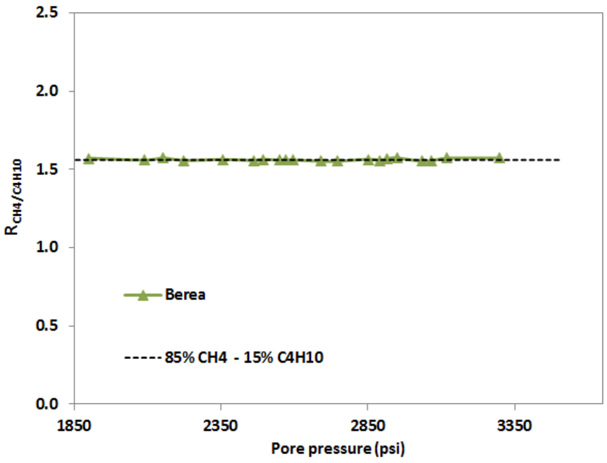

Figure 4.4.5: $R_{CH4/C4H10}$ as a function of pressure for Berea sandstone. The mixture composition is constant during the production from 3300 psi to 1900 psi.

$R_{CH4/C4H10}$ for Eagle Ford sample EF-xx72 (**Figure 4.4.6**) shows the same trend as the Berea sample; therefore, for this Eagle Ford sample, the production above the dew point will be similar as the production in conventional reservoirs.

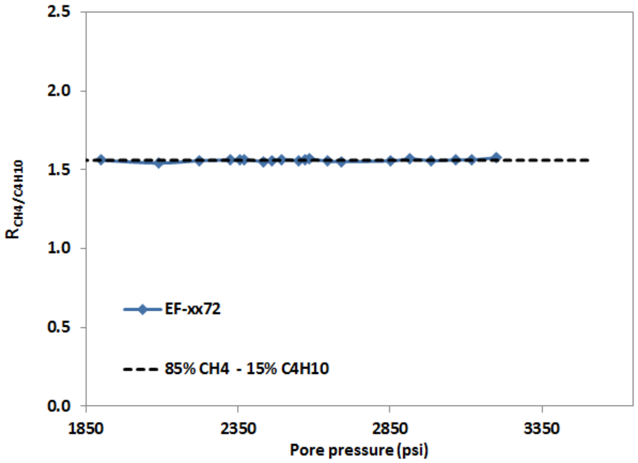

Figure 4.4.6: $R_{CH4/C4H10}$ as a function of pressure for Eagle Ford sample EF-xx72. The mixture composition is constant during the production from 3200 psi to 1900 psi.

In the case of sample the Barnett B-xx97 (**Figure 4.4.7**), the trend of $R_{CH4/C4H10}$ as a function of pressure is different from the trend observe for the empty pressure vessel, Berea sandstone and the Eagle Ford sample EF-xx72. Between 2900 psi and 2500 psi $R_{CH4/C4H10}$ is fairly constant with a value approximately equal to 1.56. However, below 2500 psi, $R_{CH4/C4H10}$ increases. This increase in $R_{CH4/C4H10}$ observed before the dew point of 85% CH_4 - 15% C_4H_{10} (1850 psi) is due to preferential retention of butane molecules by adsorption on the pore walls (essentially the organic pores) of the sample. This process will create a progressive enrichment in butane of the remaining mixture. Because of enrichment in heavier component liquid dropout will be observe in this sample at pressure above the dew point of the original fluid mixture.

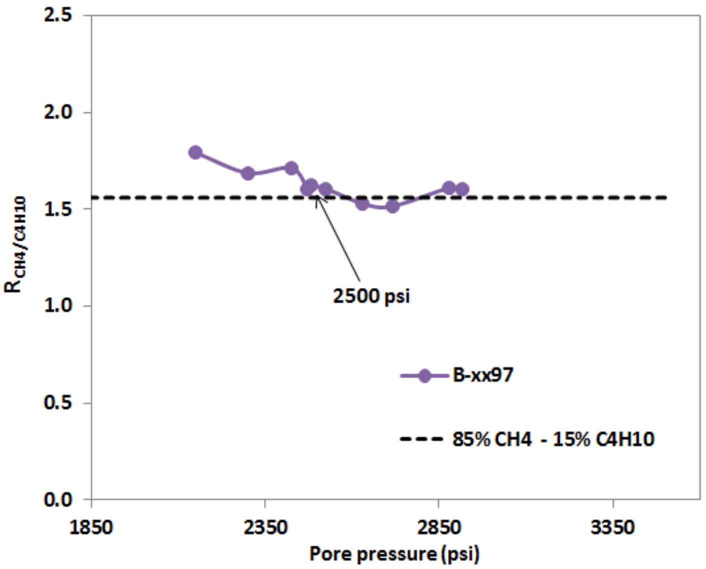

Figure 4.4.7: $R_{CH4/C4H10}$ as a function of pressure for B-xx97. We observe an increase of $R_{CH4/C4H10}$ at pressures greater than the dew point of the original mixture, because of the preferential adsorption of butane by the sample.

For the Eagle Ford sample EF-xxx82 (**Figure 4.4.8)** $R_{CH4/C4H10}$ starts at value of 1.63 for a fluid pressure of 3160 psi, implying preferential adsorption of butane at pressure higher than observed with B-xx97 Barnett sample. Between 2900 psi and 2600 psi, $R_{CH4/C4H10}$ decreases. This reduction in $R_{CH4/C4H10}$ implies that the liquid phase saturation in the dead volume is large enough to induce flow. After the liquid contained in the dead volume is produced more methane will be liberated by the sample. That is why we observe an increase of $R_{CH4/C4H10}$ below 2600 psi.

After, the measurements on EF-xxx82, we observed that the sample was fractured during the experiments and the presence of oil bubbles on the surface of the sample. The presence of oil on the surface of the sample implies that the sample contained some hydrocarbons that were not removed by the 100°C drying process. The injection of the mixture of methane and butane allowed the mobilization of these hydrocarbons. This observation implies that the injection of lean gas could potentially be used as an enhanced oil recovery method.

The magnitude of deviation of $R_{CH4/C4H10}$ from 1.56 is controlled by the dead volume of the system, and the adsorption capacity of the sample which depends on the pores surface areas to volumes ratio.

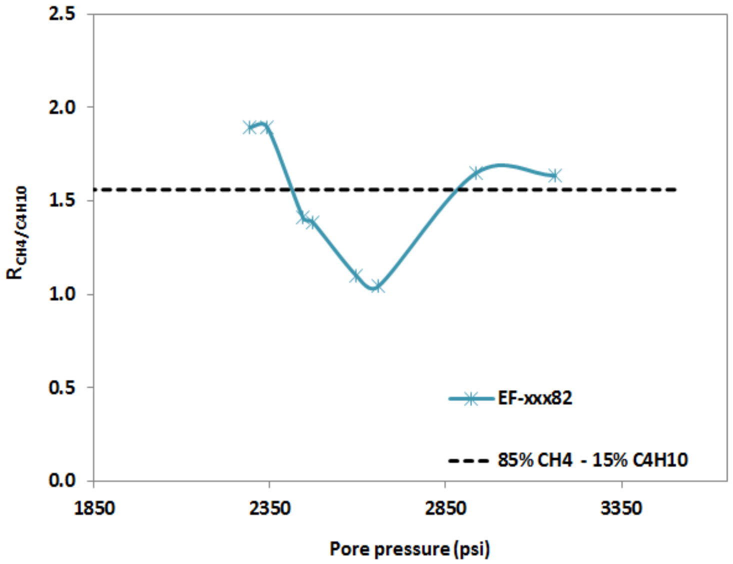

Figure 4.4.8: $R_{CH4/C4H10}$ as a function of pressure for Eagle Ford sample EF-xxx82. $R_{CH4/C4H10}$ starts at a value greater than the normal value for the original mixture, implying a preferential adsorption of butane at pressures greater than 3000 psi. This preferential adsorption induces liquid dropout at pressures greater than the dew point of the original mixture.

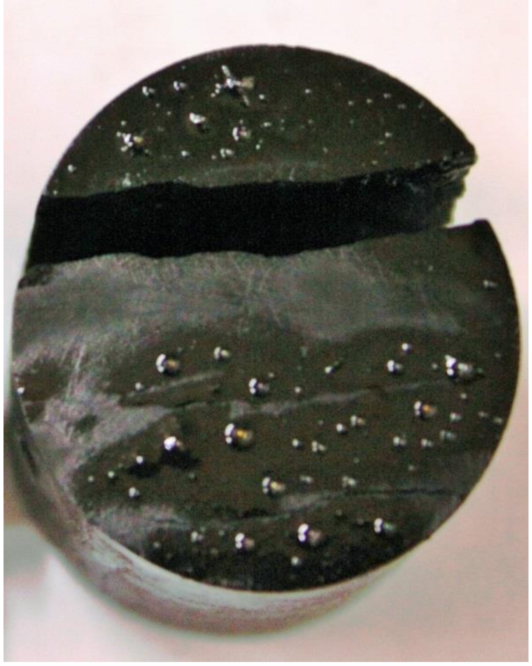

Figure 4.4.9: Sample EF-xxx82 after the injection of 85% CH_4 -15%C_4H_{10}. We observe that the sample was fractured during the experiments, and the presence of oil bubbles on the surface of the sample.

This preferential adsorption of heavier components implies that during pressure depletion, the hydrocarbon fluid composition will be different across the reservoir, even above the dew point in the case of a condensate reservoir. Lighter species will flow at a velocity greater than the velocity of heavier species. This separation between light and heavy hydrocarbon species will create an early liquid dropout near the wellbore in the case of condensate wells. However, the liquid dropout will be mobilized by the lighter species coming from the areas away from the sandface. This process will lead to the constant GOR observed in many shale condensate wells.

5 Conclusions

In shale reservoirs, the surface properties of the pores control fluid storage and flow, because of the small pore size, sub micrometer.

Pore surface properties control fluid distribution and flow through the influence of wettability on capillary pressure. The analysis of SEM images of organic rich shales shows the presence of water wet pores essentially associated with clay minerals; hydrocarbon wet pores within the solid organic matter, and mixed wettability pores at the interfaces between water wet and hydrocarbon wet components. The presence of pores with different wettability, challenges the current understanding of pore connectivity, and relative permeability. In shale reservoirs, pore connectivity is the spatial distribution and proximity of the water wet, hydrocarbon wet and mixed wet pores. To be accurate, pore scale models need to take into account the distribution of pores with different wettability.

Our analysis of the sequential imbibition of brine and dodecane by shale samples from Haynesville, Barnett, Woodford, Eagle Ford, Floyd, Utica-Collingwood and Wolfcamp formations, shows that a clay content of 20 wt% is required to develop a connected water wet pore network. The establishment of a connected hydrocarbon wet network requires at least 3-4 wt% TOC. The water wet and hydrocarbon wet pore network connectivity can be enhanced by the presence of mix wet pores.

The saturation of shale samples with brine and dodecane shows that the deliverability of hydrocarbon is often control by the water wet pore network. In shale reservoirs with pore pressures lower than the capillary pressure in the water wet pores, hydrocarbon cannot be stored or flown in the water wet network. The facies with the best hydrocarbon flow potential are the facies with considerable mixed wettability pores.

Considering that the creation of mixed wet pores require the presence of an optimum amount of organic matter, clay minerals as well as a high energy depositional environment, we postulate that the mixed wet pore will be more abundant in the shales deposited at the base of the slope in a marine environment.

The storage measurements of methane and ethane in shales show that the critical properties of hydrocarbons are not affected by the small pore sizes. However, adsorption and capillary condensation below vapor pressure can be misinterpreted as changes in critical properties.

The effect of adsorption on the storage capacity in shale reservoir reduces as the pressure increases, because, as pressure increases the contrast between the adsorbed phase density and the free phase density reduces. In the samples studied, the amount of methane stored at 500 psi could reach a maximum of 2.3 times the amount that would be stored without adsorption.

Capillary condensation can increase the storage capacity of shales by more than 8 times at pressures lower than the vapor pressure.

The multicomponent desorption experiments show that in shales with high adsorption potential lighter components will be separated from heavier components during pressure depletion even above the dew point in the case of a condensate mixture. This separation due to the adsorption of the heavy components by the pore walls will induce a change in the fluid composition across the reservoir depending on the pressure distribution. The preferential adsorption of heavier components implies that the produced hydrocarbon might not represent the fluid composition in the reservoir. During the production of hydrocarbon from shale reservoirs, it is expected that the produced fluid composition changes over time even above the dew point or the bubble point. The in-situ fluid composition during pressure depletion will not only depend on the fluid PVT but also on the interactions between the pores walls and the different types of hydrocarbon present. The dynamic change in fluid composition can lead to a constant GOR of the produced fluid.

References

1. AGI. 2013. Glossary of geology. http://glossary.agiweb.org/dbtw-wpd/exec/dbtwpub.dll (accessed 12 September 2015).
2. Al Tahini, A., and Abouseilman, Y.2008. Pore Pressure Coefficient Anisotropy Measurements For Intrinsic And Induced Anisotropy In Sandstone. SPE 116129 presented at the Annual Technical Conference and Exhibition, Denver, Colorado, 21-24 September.
3. Ambrose, R., Hartman, C. R., Campos, D. M., Akkutlu, Y., and Sondergeld, C. 2010. Shale Gas-In-Place Calculation Part I: New Pore-Scale Considerations. SPE 131772 presented at the Unconventional Gas Conference, Pittsburgh, Pennsylvania, 23-25 February.
4. API. 1998. Recommended Practices For Core Analysis. API Publishing Services.
5. Bailey, S. 2009. Closure And Compressibility Corrections To Capillary Pressure Data In Shales. Presentation given at the DWLS Fall Workshop, 19-October.
6. Ballard, B. 2007. Quantitative Mineralogy Of Reservoir Rocks Using Fourier Transform Infrared Spectroscopy. SPE 113023 presented at the Annual Technical Conference and Exhibition, Anaheim, California, 11-14 November.
7. Bertoncello, A., and Honarpour, M. M. 2013. Standards For Characterization Of Rock Properties In Unconventional Reservoirs: Fluid Flow Mechanism, Quality Control, And Uncertainties. SPE 166470 presented at the Annual Technical Conference and Exhibition, New Orleans, Louisiana, 30 September- 2 October.

8. Beskok, A., and Karniadakis, E. G. 1999. A Model For Flows In Channels, Pipes And Ducts At Micro And Nano Scales. *Microscale Thermophysical Engineering* **3**: 43-77.
9. Bloembergen, N., Purcel, E.M., and Pound, R.V. 1948. Relaxation Effects In Nuclear Magnetic Resonance Absorption. *Phys. Rev* **73**: 679-746.
10. Bohacs, K. M., Pasey, Q. R., Rudnicki, M., Esch, W. L., and Lazar, O. R. 2013. The Spectrum Of Fine-Grained Reservoirs From ‘Shale Gas’ To ‘Shale Oil’/Tight Liquids: Essential Attributes, Key Controls, Practical Characterization. IPTC 16676 presented at the International Petroleum Technology Conference, Beijing, China, 26-28 March.
11. British Geological Survey. 2003. Definition And Characteristics Of Very-Fine Grained Sedimentary Rocks: Clay, Mudstone, Shale And Slate. http://www.google.com/url?sa=t&rct=j&q=&esrc=s&source=web&cd=2&ved=0CDoQFjAB&url=http%3A%2F%2Fwww.bgs.ac.uk%2Fdownloads%2Fstart.cfm%3Fid%3D1415&ei=9VRWUvidIsK0yAGV34GADQ&usg=AFQjCNEyJDFDjNRhMxupAc_ICl08gBNPZQ&sig2=KjwI_uXfkYSsbUB3EthAtA&bvm=bv.53760139,d.aWc (downloaded 12 September 2015).
12. Brunauer S., Emmett P.H., and Teller E.1938. Adsorption Of Gases In Multimolecular Layers. *J. Am. Chem. Soc*. **62**:1723-1732.
13. Bustin, A.M.M., Bustin, R.M., and Cui, X. 2008. Importance Of Fabric On Production Of Gas Shales. SPE 114167 presented at the SPE Unconventional Reservoirs Conference, Keystone, Colorado, 10-12 February.

14. Campos, D. M. 2010. Uncertainties In Shale Gas In-Place Calculations: Molecular Simulation Approach. Master's Thesis, University of Oklahoma, Norman, Oklahoma.
15. Campos. D. M, Akkutlu, Y., and Sigal, R. 2009. A Molecular Dynamics Study On Natural Gas Solubility Enhancement In Water Confined To Small Pores. SPE 124491 presented at the Annual Technical Conference and Exhibition, New Orleans, Louisina, 4-7 October.
16. Cander, H. 2012. What Are Unconventional Resources? A Simple Definition Using Viscosity And Permeability. AAPG Search and Discovery Aticle#80217. http://www.searchanddiscovery.com/documents/2012/80217cander/ndx_cander.pdf (accessed 12 September 2015).
17. Chalmers, G. R., and Bustin, M. 2010. The Effect And Distribution Of Moisture In Gas Shale Reservoir System. AAPG Search and Discovery Aticle#80113. http://www.searchanddiscovery.com/documents/2010/80113chalmers/ndx_chalmers.pdf (accessed 12 September 2015).
18. Chalmers, G., Bustin, M., and Power, I. 2012. Characterization Of Gas Shale Pore System By Porosimetry, Pycnometry, Surface Area, And Field Emission Scanning Electron Microscopy/Transmission Electron Microscopy Image Analyses: Examples From The Barnett, Woodford, Haynesville, Marcellus, And Doig Units. *AAPG Bulletin* **96**: 1099-1119.
19. Chen, H. J., Mehmani, A., Li, B., Georgi, D., and Guodong, J. 2013. Estimation Of Total Hydrocarbon In The Presence Of Capillary Condensation For

Unconventional Shale Reservoirs. SPE 164468 presented at the Middle East Oil and gas Conference, Manama, Bahrain, 10-13 March.

20. Civan, F. 2010. Effective Correlation Of Apparent Gas Permeability In Tight Porous Media. *Transport in Porous Media* **82**: 375-384.
21. Cluff, R., Shanley, W. K., and Miller, M. Three Things We Thought We Understood About Shale Gas, But Were Afraid To Ask. http://www.discovery-group.com/pdfs/AAPG%202007%20shale%20gas%20posters%20all%20pages %20lo-res.pdf(downloaded 21 September 2015).
22. Cui, A., and Brezovski, R. 2013. Laboratory Permeability Measurements Of Unconventional Reservoirs: Useless Or Full Of Information? A Montney Example From The Western Canadian Sedimentary Basin. SPE 167047 presented at the Unconventional Resources Conference, Brisbane, Australia, 11-13 November.
23. Cui, X., Bustin, A.M.M., and Bustin, R.M. 2009. Measurement Of Gas Permeability And Diffusivity Of Tight Reservoir Rocks: Different Approaches And Their Applications. *Geofluids*. **9**: 208-223.
24. Curtis, E. M., Ambrose, J. R., Sondergeld, H. C., and Rai, C. S. 2011. Investigating The Microstructure Of Gas Shales By FIB/SEM Tomography & STEM Imaging. Presentation given at the Oklahoma Geological Survey workshop, Norman, Oklahoma, 21 July.
25. Curtis, E. M., Sondergeld, H. C., and Rai, C. S. 2013. Investigation Of The Microstructure Of Shales In The Oil Window. Presentation given at the

Unconventional Resources Technology Conference, Denver, Colorado, 12-14 August.

26. Curtis, M. 2012c. Microstructural Investigation Of The Wolfcamp, Woodford, Niobrara, And Eagle Ford Shales. Presentation given at the Unconventional Shale Consortium meeting, Norman, Oklahoma, 6-7 December.
27. Curtis, M., Cardott, B., Sondergeld, C., and Rai, C. S. 2012a. Development Of Organic Porosity In The Woodford Shale With Increasing Thermal Maturity. *International Journal of Coal Geology* **103**: 26-31.
28. Curtis, M., Cardott, B., Sondergeld, C., and Rai, C. S. 2012b. Development Of Organic Porosity In The Woodford Shale Related To Thermal Maturity. SPE 160158 presented at the Annual Technical Conference and Exhibition, San Antonio, Texas, 8-10 October.
29. Curtis, M.E., Ambrose, R.J., Sondergeld, C.H., and Rai, C.S. 2010. Structural Characterization Of Gas Shales On The Micro- And Nano-Scales. SPE 137693 presented at the Canadian Unconventional Resources & International Petroleum Conference, Calgary, Alberta, Canada, 19-21 October.
30. Dana, E. S. 1921.Textbook Of Mineralogy. W. E. Ford, New York.
31. Dang, S. 2013. Study Of Kerogen Maturity Using Transmission Fourier Transform Infrared Spectroscopy (FTIR). SPE 167637 presented at the Annual Technical Conference and Exhibition, New Orleans, Louisiana, 30 September-2 October.
32. Devegowda, D., Sapmanee, K., Civan, F., and Sigal, R. 2012. Phase Behavior Of Gas Condensates In Shales Due To Pore Proximity Effects: Implications For

Transport, Reserves And Well Productivity. SPE 160099 presented at the Annual Technical Conference and Exhibition, San Antonio, Texas, 8-10 October.

33. Dewit, C. P., and Arens. P. L. 1950. Moisture Content And Density Of Some Clay Minerals And Some Remarks On The Hydration Pattern Of Clay. Trans, 4th International Congress Of Soil Science, 2, 59-62.
34. Diaz-Campos, M., and Hobson, S. 2014. A Novel Approach For Reservoir Simulation And Fluid Characterization Of Unconventional Fields: Phase 1 Molecular Level Considerations. SPE 171786 presented at the Annual Tech
35. Didar, R. B., and Akkutlu. I. Y. 2013. Pore Size Dependency Of Fluid Phase Behavior And Properties In Organic-Rich Shale Reservoirs. SPE 164099 presented at the International Symposium on Oilfield Chemistry, Woodlands, Texas, 8-10 April.
36. Do, D. D., and Do H.D. 2003. Pore Characterization Of Carbonaceous Materials By DFT And GCMC Simulations: A Review. *Adsorption Science and Technology* **21**:389-423.
37. Dunn, J. K., Bergman, J. D., and Latorraca, G. A. 2002. Nuclear Magnetic Resonance: Petrophysical And Logging Applications. Handbook of Geophysical Exploration, Ed. Helbig, K., and Treitel, S. **32.**
38. Espiltalie, J., Madec, M., and Tissot, B. 1977. Source Rock Characterization Method For Petroleum Exploration. OTC 2935 presented at the Annual Offshore Technology Conference, Houston, Texas, 2-5 May.

39. Fathi, E., Tinni, A., and Akkutlu, Y. 2012. Shale Gas Correction To Klinkenberg Slip Theory. SPE 154977 presented at the SPE Americas Unconventional Resources Conference, Pittsburgh, Pennsylvania, 5-7 June.
40. Findenegg, H. G., and Loring, R. 1984. Fluid Adsorption Up To The Critical Point. Experimental Study Of A Wetting Fluid/Solid Interface. *J. Chem. Phys* **81**: 3270-3276.
41. Fitzgerald, E. J. 2005. Adsorption Of Pure And Multi-Component Gases Of Importance To Enhanced Coalbed Methane Recovery: Measurements And Simplified Local Density Modeling. Ph.D. Dissertation, Oklahoma State University, Stillwater, Oklahoma.
42. Florence, F. A., Rushing, J. A., Newsham, K. E., and Blasingame, T. A. 2007. Improved Permeability Prediction Relations For Low Permeability Sands. SPE 107954 presented at Rocky Mountain Oil & Gas Technology Symposium, Denver, Colorado, 16-18 April.
43. Gale, F. W. J., Reed, M. R., and Holder, J. 2006. Natural Fractures In The Barnett Shale And Their Importance For Hydraulic Fracture Treatments. AAPG Bulletin **91**: 603-622.
44. Ghanizadeh, A., Hildenbrand, A. A., Gasparik, M., Gensterblum Y., Krooss, B., and Littke, R. 2013. Experimental Study Of Fluid Transport Processes In The Matrix System Of The European Organic Rich Shales: II. Posidonia Shale (Lower Toarcian, Northern Germany). *International Journal of Coal Geology* **123**: 20-33.

45. Gregg, S. J and Sing, K. S. W., 1982. Adsorption, Surface Area And Porosity. 2nd Edition, London: Academic press.

46. Groen, J. C., peffer, L. A. A., and Perez, M. 2003. Pore Size Determination In Modified Micro And Mesoporous Materials. Pitfalls And Limitations In Gas Adsorption Data Analysis. *Microporous and Mesoporous Mater* **60** 1-17.

47. Gruner, J. W. 1937. Densities And Structural Relationships Of Kaolinites And Anauxites. *American Mineralogist* **22**: 855-860.

48. Gupta, N. 2012. Multi-Scale Characterization Of The Woodford Shale In West Central Oklahoma: From Scanning Electron Microscopy To 3D Seismic. Ph.D. Dissertation, University of Oklahoma, Norman, Oklahoma.

49. Handwerger, D. A., Suarez-Rivera, R., Vaughn, K. I., and Keller, J. K. 2011. Improved Petrophysical Core Measurements On Tight Shale Reservoirs Using Retort And Crushed Samples. SPE 147456 presented at the Annual Technical Conference and Exhibition, Denver, Colorado, 30 October-2 November.

50. Harry, D. 2009. Three Common Source Rock Evaluation Errors Made By Geologist During Prospect Or Play Appraisal. *AAPG Bulletin* **93**: 341-356.

51. Haydel, J., and Kobayashi, R. 1967. Adsorption Equilibria In The Methane-Propane-Silica Gel System At High Pressures. *Industrial and Engineering Chemistry Fundamentals* **6**: 564-554.

52. Heller, R., and Zoback, M. 2014. Adsorption Of Methane And Carbon Dioxide On Gas Shale And Pure Mineral Samples. *J. Unconventional Oil and Gas Resources* **8**: 14-24.

53. Hirasaki, J. G., and Mohanty, K. K. 2008. Fluid-Rock Characterization For NMR Well Logging And Special Core Analysis. DE-FC26-04NT15515 final report.
54. Honarpour, M. M., Nagarajan, N. R., Orangi, A., Arasteh, F., and Yao, Z. 2012. Characterization Of Critical Fluid PVT, Rock, And Rock-Fluid Properties - Impact On Reservoir Performance Of Liquid Rich Shales. SPE 158042 presented at the Annual Technical Conference and Exhibition, San Antonio, Texas, 8-10 October.
http://geology.gsapubs.org/content/early/2013/03/15/G33639.1.full.pdf+html (downloaded 20 September 2015).
55. Hu, Q., Gao, X., Gao, Z., Ewing, R., Dultz, S., and Kaufmann, J. 2014. Pore Accessibility And Connectivity Of Mineral And Kerogen Phases In Shales. URTeC 1922943 presented at the Unconventional Resources Technology Conference, Denver, Colorado, 25-27 August.
56. Jarvie, D. M., Claxton, B., Henk, B., and Breyer, T. 2001. Oil And Gas From Barnett Shale, Fort Worth Basin, Texas. Presentation given at the AAPG National Convention, Denver, Colorado, 3-6 June.
57. Jones, F, O., and Owens, W. W. 1980. A Laboratory Study Of Low-Permeability Gas Sands. *SPE Journal of Petroleum Technology* **32**: 1631-1640. SPE 7551-PA.
58. Kale, S. 2009. Petrophysical Characterization Of Barnett Shale Play. Master's Thesis, University of Oklahoma, Norman, Oklahoma.

59. Kang, M. S., Fathi, E., Ambrose, R, J., Akkutlu, Y. I., and Sigal, F. R. 2010. Carbon Dioxide Storage Capacity Of Organic Rich Shales. SPE 134583 presented at the Annual Technical Conference and Exhibition, Florence, Italy, 20-22 September.
60. Karastathis, A. 2007. Petrophysical Measurements On A Tight Gas Shale. Master's Thesis, University of Oklahoma, Norman, Oklahoma.
61. Khoshghadam, M., Khanal, A., and Lee, W. J. 2015. Numerical Study Of Production Mechanisms And Gas-Oil Ratio Behavior Of Liquid-Rich Shale Oil Reservoirs. SPE 175137 presented at the Annual Technical Conference and Exhibition, Houston, Texas, 28-30 September.
62. King, E. H., Eberle, P. R.A., Walters, C. C., Kliewer, E. C., Ertas, D., and Huynh, C. 2015. Pore Architecture And Connectivity In Gas Shale. *Energy Fuels,* **29**: 1375-1390.
63. Klaver, J., Hemes, S., Houben, M., Desbois, G., Radi, Z., and Urai, L. J. 2015. The Connectivity Of Pore Space In Mudstones: Insights From High Pressure Wood's Metal Injection, BIB-SEM Imaging, And Mercury Intrusion Porosimetry. Gofluids, **103**:12-25.
64. Klinkenberg, L. J., 1941. The Permeability Of Porous Media To Liquids And Gases. *Drilling and Production Practice* **41**: 200-213.
65. Langmuir, I. 1918. The Adsorption Of Gases On Plane Surfaces Of Glass, Mica And Platinum. *J. Am. Chem. Soc* **40**: 1361-1403.
66. Laughrey, D. C., Ruble, E. T., Purrazzella, P., Hooghan, K., Beuthin, J., Washburn, K., and Dorsey, W. 2013. Dual Mineral Matrix And Organic Pore

Textures In Thermally Mature Niobrara Formation (Upper Cretaceous) Rocks, Rocky Mountains, Regions, USA. Presentation given at the Houston geological Survey Mudrocks Symposium, Houston, Texas, 18-19 February.

67. Loucks, R. G., Ruppel, S., Reed, R., and Hammes, U. 2011. Origin And Classification Of Pores In Mudstones From Shale-Gas Systems. AAPG Search and Discovery Aticle#40855. http://www.searchanddiscovery.com/documents/2011/40855loucks/ndx_loucks.pdf (accessed 25 September 2015).
68. Luffel, D.L., Hopkins, C.W., Holditch, S.A., and Schettler, P.D. 1993. Matrix Permeability Measurement Of Gas Productive Shales. SPE 26633 presented at the SPE Annual Technical Conference and Exhibition, Houston, Texas, 3-6 October.
69. Ma, Y., Jin, L., and Jamili, A. 2013. Modifying Van Der Waals Equation Of State To Consider Influence Of Confinement On Phase Behavior. SPE 166476 presented at the Annual Technical Conference and Exhibition, New Orleans, Louisiana 30 September- 2 October.
70. Mahomad, B. 2014. Evaluation Of Shale Compressibility From NMR And MICP Measurements. Master’s Thesis, university of Oklahoma, Norman, Oklahoma.
71. Mathur. 2015. Experimental Investigation Of Matrix Permeability Of Shale. Master’s Thesis, University of Oklahoma, Norman, Oklahoma.
72. Menon, P. G. 1968. Adsorption At High Pressures. *Chemical Reviews* **68**: 277-294.

73. Michel, G. g., Sigal, R., Civan, F., and Devegowda, D. 2011. Parametric Investigation Of Shale Gas Production Considering Nano-Scale Pore Size Distribution, Formation Factor, And Non-Darcy Flow Mechanisms. SPE 147438 presented at the Annual Technical Conference and Exhibition, Denver, Colorado, 30 October-2 November.
74. Mighani, S. 2014. Rock Tensile Failure Related To Improving Hydraulic Fracture. Master's Thesis, university of Oklahoma, Norman, Oklahoma.
75. Mohammad, S., Fitzgerald, J. E., Robinson, L. R., and Gasem, K. 2009. Experimental Uncertainties In Volumetric Methods For Measuring Equilibrium Adsorption. *Energy Fuels* **29**: 2810-2820.
76. Odusina, E. 2011. An NMR Study Of Shale Wettability. Master's Thesis, University of Oklahoma, Norman, Oklahoma.
77. Pathi, V. S. M., 2008. Factors Affecting The Permeability Of Gas Shales. Master's Thesis, British Columbia U, Vancouver, Canada.
78. Peng, D. Y., and Robinson, D. B. 1976. A New Two-Constant Equation Of State. *Industrial and Engineering Chemistry: Fundamentals* **15**: 59–64.
79. Peng, S., Zhang, T., and Ruppel, C. S. 2014. Upscaling Of Pore Network And Permeability From Micron To Millimeter Scale In Organic-Pore Dominated Mudstones. Search and Discovery Aticle#41429. http://www.searchanddiscovery.com/documents/2014/41429peng/ndx_peng.pd (accessed 12 September 2015).
80. Peters, K., and Cassa, M. R. 1994. Applied Source Rock Geochemistry. In *The petroleum System, From Source To Trap*, Chap 5, 93-120. AAPG Memoir 60.

81. Pitakbunkate, T., Balbuena, B. P., Moridis, J. G., and Blasingame, T. A. 2014. Effect Of Confinement On Pressure/Volume/Temperature Properties Of Hydrocarbons In Shale Reservoirs. SPE 170685 presented at the Annual Technical Conference and Exhibition, Amsterdam, 27-29 October.
82. Rickman, R., Mullen, M., Petre, J. E., Grieser, W. V., and Kundert, D., 2008. A Practical Use Of Shale Petrophysics For Stimulation Design Optimization: All Shale Plays Are Not Clones Of The Barnett Shale. SPE 115258 presented at the Annual Technical Conference and Exhibition, Denver, Colorado, 21-24 September.
83. Sakhaee-Pour, A., and Bryant, S. 2011. Gas Permeability Of Shale. SPE 146944 presented at the Annual Technical Conference and Exhibition, Denver, Colorado, 30 October-2 November.
84. Sarkar, M. 2008. Petrophysical Study Of Shales Under High Temperature And Pressure. Master’s Thesis, university of Oklahoma, Norman, Oklahoma.
85. Sharma, A., and Damani, A. 2013. Hydraulic Fracture Characterization Using Acoustic Mapping And Fractography. Presentation given at the Unconventional Shale Consortium meeting, Norman, Oklahoma, 10-11 June.
86. Sinha, S., Braun, E. M., Determan, D. M., Passey, Q, R., Leornardi, S. A., Boros, J. A., Wood III, A. C., Zirkle, T., and Kudva, R. A. 2013. Steady-State Permeability Measurements On Intact Shale Samples At Reservoir Conditions - Effect Of Stress, Temperature, Pressure, And Type Of Gas. SPE 164263 presented at the Middle East Oil & Gas Show and Conference, Manama, Bahrain, 10-13 March.

87. Sisk, C., Diaz, E., Walls, J., Grader, A., and Suhner, M. 2010. 3D Visualization And Classification Of Pore Structure And Pore Filling In Gas Shales. SPE 134582 presented at the Annual Technical Conference and Exhibition, Florence, Italy, 20-22 September.
88. Soave, G. 1972. Equilibrium Constants From A Modified Redlich-Kwong Equation Of State. *Chem. Eng. Sci* **27**: 1197-1203
89. Soeder, D.J., 1988. Porosity And Permeability Of Eastern Devonian Gas Shale. *SPEFE* **3**: 116–124. SPE 15213-PA.
90. Sondergeld, C. 2011. Fourier Transform Infrared Spectroscopy And X-Ray Diffraction. Seminar presented 25 August 2011 at the University of Oklahoma.
91. Sondergeld, C. H., and Rai, C. S. 1993. A New Exploration Tool: Quantitative Core Characterization. *Pure and Applied Geophysics* **141**: 249-268.
92. Sondergeld, C.H. and Rai, C.S. 2011. Elastic Anisotropy Of Shales. *The Leading Edge* **30**: 324-331.
93. Sondhi, N. 2011. Petrophysical Characterization Of Eagle Ford Shale. Master's Thesis, University of Oklahoma, Norman, Oklahoma.
94. Suarez-Rivera, R., Chertov, M., Dean, W., Sidney, G., and Keller, J. Understanding Permeability Measurements In Tight Shales Promotes Enhanced Determination Of Reservoir Quality. SPE 162816 presented at the Canadian Unconventional Resources Conference, Calgary, Canada.
95. Sudibandriyo, M., Pan, Z., Fitzgerald, J. E., Robinson, L. R., and Gasem, K. 2003. Adsorption Of Methane, Nitrogen, Carbon Dioxide, And Their Binary

Mixtures On Dry Activated Carbon At 318.2 K And Pressures Up To 13.6 Mpa. *Langmuir* **19**: 5523-5531.

96. Sulucarnain, I. 2013. An NMR Study Of Shale Wettability And Effective Surface Relaxivity. Master's Thesis, university of Oklahoma, Norman, Oklahoma.
97. Thomsen, L. 1986. Weak Elastic Anisotropy. *Geophysics* **51**: 1954-1966.
98. Tinni, A., Fathi, E., Agarwal, R., Akkutlu, Y., Sondergeld, C., and Rai. C. 2012. Shale Permeability Measurements On Plugs And Crushed Samples. SPE 162235 presented at the Canadian Unconventional Resources Conference, Calgary, Canada, 30 October-1 November.
99. Tinni, A., Sondergeld, C. H., and Rai, C. S. 2014. NMR Response Of Brine, Oil And Methane In Organic Rich Shales. SPE 168971 presented at the Unconventional Resources Conference, Woodlands, Texas, 1-3 April.
100. Tinni, A., Sondergeld, C. H., and Rai, C.S. 2014. NMR T1-T2 Response Of Moveable And Non-Moveable Fluids In Conventional And Unconventional Rocks. SCA2014-091 presented at the International Symposium, Avignon, France, 8-11 September.
101. Tissot, B. P., Pelet, R., and Ungerer, P.H. 1987. Thermal History Of Sedimentary Basins, Maturation Indices, And Kinetics Of Oil And Gas Generation. *AAPG Bulletin* **71**: 1445-1466.
102. USGS. 2002. http://geomaps.wr.usgs.gov/parks/misc/glossarys.html (accessed 11 September 2015).

103. Valenza, j., Drenzek, N., Marques, F., Pagels, M., and Mastalerz, M. 2013. Geochemical Controls On Shale Microstructure. http://geology.gsapubs.org/content/early/2013/03/15/G33639.1.full.pdf+html (downloaded 20 September 2015).

104. Xu, M., and Dehghanpour, H. 2014. Advances In Understanding Wettability Of Gas Shales. *Energy Fuels* **28**: 4362-4375.

Appendix

Table A-I: Petrophysical properties of the samples used for sequential spontaneous imbibition of brine and dodecane. The letters in parenthesis next to the shale formation name indicate the gas window (G), the condensate window (C) and the oil window (O)

Shale formation	Sample ID	Crushed helium Φ(%)	Quartz +Feldspars (wt%)	Total clays (wt%)	Total carbonates (wt%)	TOC (wt%)
Haynesville (G)	H-xxx10.4	10.3	10	66	1	4.1
	H-xxx26.8	10.9	20	60	21	5.7
	H-xxx35.2	7.9	20	26	54	8.4
	H-xxx55.8	6.4	17	27	53	8.3
	H-xxx61.7	6.3	12	37	49	5.0
	H-xxx95.8	6.9	13	50	32	0.8
	H-xxx06.8	6.3	3	7	88	0.9
Woodford (G)	W-xxx13	7.0	47	31	21	5.0
	W-xxx17	4.0	60	13	28	2.4
	W-xxx36.3	6.4	40	52	8	8.6
	W-xxx48.4	6.6	50	42	8	6.4
	W-xxx89	1.9	4	4	84	0.2
	W-xxx23.1	6.1	79	16	5	2.0
Floyd (G)	F-xx25.5	7.0	17	71	12	3.2
	F-xx37	9.2	26	67	7	3.5
	F-xx59	7.4	19	74	7	3.5
	F-xx66.5	5.6	23	69	8	5.2
	F-xx69.8	7.8	23	72	5	4.5
Barnett (G)	B-xx03	3.2	20	10	74	0.7
	B-xx15	6.3	44	39	14	4.5
	B-xx93.3	4.9	42	35	22	3.3
	B-xx03.7	6.3	42	54	2	4.6
	B-xx44	4.2	21	58	15	7.0
Eagle Ford (G)	EF-xxx79	8.5	10	56	33	2.3
	EF-xxx92	5.3	8	62	26	3.8
	MEF-xxx09	10.0	6	41	50	4.1
Eagle Ford (C)	EF-xxx18	8.6	5	29	63	5.5
	EF-xx35	5.7	3	43	52	1.4
	EF-xx80	12.8	8	36	48	6.0
Utica-Collingwood (C)	UC-xx01	5.7	21	74	6	1.6
	UC-xx02	3.7	16	80	4	1.7
	UC-xx03	5.3	17	76	7	2.1
	UC-xx04	3.3	14	37	12	4.3
	UC-xx05	2.2	11	6	82	4.2
	UC-xx07	4.2	7	15	73	4.9
	UC-xx09	1.5	3	10	83	0.3
	UC-xx12	4.9	9	20	70	5.8
	UC-xx23	2.3	2	5	91	1.9
	UC-xx25	1.8	0	17	83	3.4
Wolfcamp (O)	Wc-xx83	7.1	24	66	4	2.5
	Wc-xx95	7.9	28	65	3	2.1
	Wc-xx03	6.4	19	72	5	1.6
	Wc-xx18	7.3	52	36	10	8.5
	Wc-xx19.08	6.5	28	47	15	7.8
	Wc-xx75	6.5	20	68	9	8.0

Table A-II: Petrophysical properties of the samples used for brine and dodecane saturation.

Shale formation	Sample ID	Crushed helium Φ(%)	Quartz +Feldspars (wt%)	Total clays (wt%)	Total carbonates (wt%)	TOC (wt%)
Haynesville (G)	H-xxx80	10.9	24	47	28	3.4
	H-xxx92	9.1	17	58	25	2.8
	H-xxx20	9.0	38	35	16	4.6
	H-xxx55	6.0	17	27	53	8.3
	H-xxx78	5.6	5	43	44	2.5
Woodford (G)	W-xxx36.3	6.4	40	52	8	8.6
	W-xxx48.48	6.6	50	42	8	6.4
Barnett (G)	B-xx44	6.7	45	47	5	4.2
	B-xx79	5.9	25	64	7	5.4
	B-xx93	4.8	21	25	47	2.8
	B-xx97	5.2	36	49	15	5.2
	B-xx08	4.8	26	46	26	3.0
	B-xx14	5.6	23	36	31	3.3
	B-xx16	5.9	31	48	17	2.7
	B-xx93.3	4.9	42	35	22	3.3
Utica-Collingwood (C)	UC-xx14	2.8	8	23	67	0.8
	UC-xx39	6.2	12	82	4	0.6
	UC-xx70	3.6	30	51	19	0.7
	UC-xx83	3.6	10	18	70	4.3
	UC-xx18	1.7	14	9	75	0.6
Marcellus (G)	M-xx11	9.8	23	72	4	4.1
	M-xx22	10.8	27	63	5	3.9
	M-xx26	13.1	42	48	10	8.4
	M-xx30	2.9	11	15	74	1.2

Table A-III: Petrophysical properties of the additional samples used for dodecane saturation.

Shale formation	Sample ID	Crushed helium Φ(%)	Quartz +Feldspars (wt%)	Total clays (wt%)	Total carbonates (wt%)	TOC (wt%)
Haynesville (G)	H-xxx69	10.9	14	55	12	6.3
	H-xxx33.5	9.6	12	30	53	3.9
	H-xxx84	8.7	10	52	34	1.0
	H-xxx89	9.2	8	68	17	3.5
Woodford (G)	W-xxx94	7.2	51	26	21	7.2
	W-xxx20	7.9	56	29	14	8.0
	W-xxx70	4.1	31	40	24	0.9
	W-xxx33.1	5.5	69	21	9	2.0
	W-xxx69.95	6.4	28	64	5	0.6
Barnett (G)	B-xx47	6.1	40	46	12	5.5
	B-xx17.5	4.8	43	50	4	4.1
	B-xx07.3	5.9	46	51	0	6.2
	B-xx15	5.9	31	48	17	2.7
Utica-Collingwood (C)	UC-xx72	1.7	7	6	86	2.1
	UC-xx73	5.6	18	55	27	1.7
	UC-xx03	5.3	17	76	7	2.1
Wolfcamp (O)	Wc-xx75	7.8	49	41	10	4.0
	Wc-xx39	3.6	23	27	49	1.2
	Wc-xx63	6.3	43	39	17	2.1
	Wc-xx93	6.5	49	45	6	3.6
	Wc-xx23	5.8	48	48	4	2.1
	Wc-xx53	8.5	38	53	9	3.4
	Wc-xx25	1.6	1	2	93	0.1

Table A-IV: Petrophysical properties of the samples used for subcritical nitrogen adsorption experiments.

Shale formation	Sample ID	Crushed helium Φ(%)	Quartz +Feldspars (wt%)	Total clays (wt%)	Total carbonates (wt%)	TOC (wt%)
Haynesville (G)	H-xxx69.7	10.9	14	55	12	6.3
	H-xxx20.02	9.0	38	35	16	4.6
	H-xxx27.82	10.5	25	56	17	3.2
	H-xxx35.2	10.8	12	29	54	8.4
	H-xxx44.6	4.6	1	5	86	0.6
	H-xxx43	4.2	3	8	89	0.3
	H-xxx55.8	6.0	17	27	53	8.3
	H-xxx68.8	7.6	12	48	37	3.0
	H-xxx58	7.4	7	44	38	2.5
	H-xxx89	9.2	8	68	17	3.5
	H-xxx78	5.6	5	43	44	2.5
Barnett (G)	B-xx44	6.6	45	47		4.2
	B-xx48	6.5	38	44	5	3.5
	B-xx66	5.4	26	62	9	6.8
	B-xx72	5.1	21	44	24	6.8
	B-xx81	4.9	42	25	17	7.5
	B-xx93	4.8	21	25	47	2.8
	B-xx08	4.8	26	46	26	3.0
	B-xx20	3.9	30	27	38	2.4
	B-xx97	5.2	38	39	13	7.5
Wolfcamp (O)	Wc-xx77	9.7	29	72	3	2.2
	Wc-xx95	7.9	42	65	3	2.1
	Wc-xx07	8.0	37	60	6	2.9
	Wc-xx73	6.7	50	58	3	7.6
	Wc-xx79	4.5	37	37	4	3.4
	Wc-xx09	6.2	41	62	8	2.7
	Wc-xx18	7.3	61	36	10	8.5
	Wc-xx21	11.5	62	51	5	1.2
	Wc-xx33	7.9	46	47	12	3.4
	Wc-xx75	6.5	28	68	9	8.0
	Wc-xx74	6.6	25	65	8	7.2
Avalon (O)	A-xx50	7.2	52	39	7	3.7
	A-xx30	5.6	50	13	29	4.8
	A-xx40	8.8	51	29	14	6.6
	A-xx80	2.1	15	5	77	1.5
	A-xx00	8.4	56	32	13	5.9
	A-xx20	7.1	53	29	14	4.6
	A-xx30	13.1	63	25	9	4.6
	A-xx90	6.8	40	14	37	5.2
	A-xx00	2.2	25	5	70	3.1